

ABSTRACT

Title of Thesis: EFFECTS OF 3D PRINTED VASCULAR NETWORKS ON HUMAN MESENCHYMAL STEM CELL VIABILITY IN LARGE BONE TISSUE CONSTRUCTS

Owen Matthew Ball, Master of Science, 2015

Thesis Directed By: Professor and Associate Chair, Dr. John P. Fisher, Fischell Department of Bioengineering

There is a significant clinical need for engineered bone graft substitutes that can quickly, effectively, and safely repair segmental bone defects. One emerging field of interest involves the growth of engineered bone tissue *in vitro* within bioreactors, the most promising of which, are perfusion bioreactors. Utilizing a tubular perfusion system bioreactor, which allows media to perfuse freely around alginate scaffolds laden with human mesenchymal stem cells, large-scale bone constructs can be created by simply aggregating these beads together in the desired shape. However, these engineered constructs lack inherent vasculature and quickly develop a necrotic core, where no nutrient exchange occurs. Through the use of 3D printed vascular structures, used in conjunction with a TPS bioreactor, cell viability after just one day of aggregation was found to increase by as much as 50 percent in the core of these constructs, with *in silico* modeling predicting construct viability at steady state.

EFFECTS OF 3D PRINTED VASCULAR NETWORKS ON HUMAN
MESENCHYMAL STEM CELL VIABILITY IN LARGE BONE TISSUE
CONSTRUCTS

by

Owen Matthew Ball

Thesis submitted to the Faculty of the Graduate School of the
University of Maryland, College Park, in partial fulfillment
of the requirements for the degree of
Master of Science
2015

Advisory Committee:
Professor John P. Fisher, Chair
Associate Professor Keith Herold
Assistant Professor Steven Jay

© Copyright by
Owen Matthew Ball
2015

Acknowledgements

I would first like to thank my advisor, Dr. John P. Fisher, for allowing me to become a part of the Tissue Engineering and Biomaterials Laboratory (TEBL). Coming from an undergraduate institution that did not have a graduate program, much less a bioengineering program, he always worked to make sure that I understood what was expected and provided positive support to keep me on track.

Next, I would like to thank Bao Nguyen, who took me under her wing and taught me nearly everything I know about how to function in a bioengineering lab. Without her aid and expertise, I would never have been able to finish this project on time. I would also like to thank Dr. Jesse Placone who spent countless hours training me to use the 3D printers in the lab, along with other lab skills.

I would also like to thank Dr. Herold and Dr. Jay who graciously agreed to serve as committee members for my defense on relatively short notice and who also provided valuable feedback along the way.

Finally, I would like to thank the rest of the TEBL members: Max Lerman, Laurie Bracaglia, Tony Melchiorri, Charlotte Piard, Javier Rueda, Ting Guo, Vincent Kuo, Navein Arumugasaamy, Dr. Hannah Baker, and Tara Talaie for all of their help and support along the way, and for just being good people. You all truly made my experience quite enjoyable.

Table of Contents

Acknowledgements.....	ii
Table of Contents.....	iii
List of Tables.....	v
List of Figures.....	vi
List of Abbreviations.....	viii
Chapter 1: Introduction.....	1
Chapter 2: Review of Related Literature.....	5
Introduction.....	5
TPS Bioreactors.....	6
Bioreactor Design.....	6
Advantages of a TPS Bioreactor.....	8
Tissue Engineering Strategies for Vascularized Constructs.....	10
Oxygen in the hMSC Niche.....	18
Chapter 3: Development of Vascular Networks for Large Bone Tissue Constructs ..	20
Introduction.....	20
Materials and Methods.....	21
SolidWorks Geometry Generation.....	21
COMSOL Mass Transport Analysis.....	25
SolidWorks Flow Analysis.....	29
Experimental Group Determination.....	32
3D Printing.....	33
EShell Sterilization.....	36
Alginate Bead Formation.....	37
Cell Culture.....	38
Bioreactor Setup.....	40
Construct Aggregation.....	42
Viability Analysis.....	43
Results.....	46
Initial Bioreactor Setup.....	46
COMSOL Diffusion Studies.....	48
SolidWorks CFD Analysis.....	55
<i>In Vitro</i> BTE Construct Viability.....	57
Discussion.....	60
COMSOL Diffusion Studies.....	60
SolidWorks CFD Analysis.....	61
<i>In Vitro</i> Viability Analyses.....	62
Future Directions.....	67
Conclusion.....	68
Appendix A: Raw Data.....	72
Appendix B: Calculations.....	85
Appendix C: ImageJ Macro Procedures.....	89
Appendix D: Viability Analysis Graphical Results.....	90

Appendix E: COMSOL Simulation Results	92
Appendix F: SolidWorks CFD Results.....	99
Appendix F: Additional Bioreactor Pictures.....	106
Bibliography	109

List of Tables

Table 1: 2% Alginate Bead Diameters in 0.1M CaCl ₂	72
Table 2: Percent Live Values for Each Bead	72
Table 3: Bottom Inner Day 1 Raw Data	73
Table 4: Bottom Inner Day 2 Raw Data	74
Table 5: Bottom Outer Day 1 Raw Data.....	75
Table 6: Bottom Outer Day 2 Raw Data.....	76
Table 7: Middle Inner Day 1 Raw Data.....	77
Table 8: Middle Inner Day 2 Raw Data.....	78
Table 9: Middle Outer Day 1 Raw Data	79
Table 10: Middle Outer Day 2 Raw Data	80
Table 11: Top Inner Day 1 Raw Data.....	81
Table 12: Top Inner Day 2 Raw Data.....	82
Table 13: Top Outer Day 1 Raw Data	83
Table 14: Top Outer Day 2 Raw Data	84

List of Figures

Figure 1: SolidWorks Design.....	22
Figure 2: Network Design.....	23
Figure 3: Custom Designed Connector – Units Displayed in mm.....	24
Figure 4: Bioreactor Network Design.....	25
Figure 5: Two Designs Printed Simultaneously	35
Figure 6: Soft-Cured Network, Complete with Support Structures.....	36
Figure 7: Alginate Bead Formation	38
Figure 8: Bioreactor Setup	41
Figure 9: Bioreactor Setup Featuring 4 Experimental Groups in Parallel	42
Figure 10: Harvest Sites.....	44
Figure 11: Perfusion of "Free" Beads by Green Food Dye	46
Figure 12: Final Network Design	47
Figure 13: Aggregated Alginate Construct.....	47
Figure 14: Rehydration of Aggregated Construct.....	48
Figure 15: 1.5mm Pore Spacing Oxygen Concentration - Middle Branch, Silicone..	49
Figure 16: 9mm Pore Spacing Oxygen Concentration - Middle Branch, Silicone.....	50
Figure 17: 1.5mm Pore Spacing Oxygen Concentration - Middle Branch, FEP.....	51
Figure 18: 9mm Pore Spacing Oxygen Concentration - Middle Branch, FEP.....	51
Figure 19: 1.5mm Pore Spacing Oxygen Concentration - Top/Bottom Branch, FEP	52
Figure 20: 9mm Pore Spacing Oxygen Concentration - Top/Bottom Branch, FEP...	52
Figure 21: 3mm Pore Spacing Oxygen Concentration - Middle Branch, FEP.....	53
Figure 22: 6mm Pore Spacing Oxygen Concentration - Middle Branch, FEP.....	53
Figure 23: 1.5mm Pore Spacing Oxygen Concentration - Single Tube, FEP.....	54
Figure 24: 1.5mm Pore Spacing Oxygen Concentration - Single Tube, FEP.....	55
Figure 25: Full Network, 1.5mm Pore Spacing CFD Results.....	55
Figure 26: Full Network, 9mm Pore Spacing CFD Results	56
Figure 27: Single Tube, 9mm Pore Spacing CFD Results	56
Figure 28: Flow Through an Aggregated Alginate Construct	57
Figure 29: Containment of Flow Through an Aggregated Alginate Construct	57
Figure 30: Day 1 Merged Live/Dead Images	58
Figure 31: Day 1 Percent Live Composite Averages.....	58
Figure 32: Viability in the Core of Static Control and Silicone Groups.....	59
Figure 33: Graphical Representation of Core Viability	59
Figure 34: Day 2 Percent Live Composite Averages.....	60
Figure 35: Failure of Single Tube to Adequately Bond with Construct	64
Figure 36: Aggregated Construct Demonstrates Possibility of Direct Anastomosis..	64
Figure 37: Composite Averages and Corresponding COMSOL Expectations.....	65
Figure 38: ImageJ Image Processing Macro.....	89
Figure 39: ImageJ Image Overlay Macro	89
Figure 40: ImageJ Counting Macro	89
Figure 41: Legend for All Viability Graphs	90
Figure 42: Day 1 Viability Results	90

Figure 43: Day 2 Viability Results	91
Figure 44: 1.5 mm Pore Spacing - Middle Branch, FEP	92
Figure 45: 1.5 mm Pore Spacing - Middle Branch, Silicone	92
Figure 46: 3 mm Pore Spacing - Middle Branch, FEP	93
Figure 47: 6 mm Pore Spacing - Middle Branch, FEP	93
Figure 48: 9 mm Pore Spacing - Middle Branch, FEP	94
Figure 49: 9 mm Pore Spacing - Middle Branch, Silicone	94
Figure 50: 1.5 mm Pore Spacing – Top/Bottom Branch, FEP.....	95
Figure 51: 1.5 mm Pore Spacing – Top/Bottom Branch, Silicone	95
Figure 52: 3 mm Pore Spacing – Top/Bottom Branch, FEP.....	96
Figure 53: 6 mm Pore Spacing – Top/Bottom Branch, FEP.....	96
Figure 54: 9 mm Pore Spacing – Top/Bottom Branch, FEP.....	97
Figure 55: 9 mm Pore Spacing – Top/Bottom Branch, Silicone	97
Figure 56: 1.5 mm Pore Spacing – Single Tube, FEP	98
Figure 57: 9 mm Pore Spacing – Single Tube, FEP	98
Figure 58: CFD Results Legend	99
Figure 59: Close Pore Trajectory Profile	99
Figure 60: Close Pore Vertical Cut Plot, 5 mm Offset	100
Figure 61: Close Pore Vertical Cut Plot	100
Figure 62: Close Pore Horizontal Cut Plot	101
Figure 63: Distant Pore Trajectory Profile.....	101
Figure 64: Distant Pore Vertical Cut Plot, 5 mm Offset.....	102
Figure 65: Distant Pore Vertical Cut Plot.....	102
Figure 66: Distant Pore Horizontal Cut Plot.....	103
Figure 67: Single Tube Trajectory Profile	103
Figure 68: Single Tube Vertical Cut Plot, 5 mm Offset	104
Figure 69: Single Tube Horizontal Cut Plot	104
Figure 70: CFD Legend for Darcy Flow Simulations	105
Figure 71: Darcy Trajectory Profile, Close Pore Group	105
Figure 72: Darcy Trajectory Profile Rear View	105
Figure 73: Darcy Trajectory Profile Side View	106
Figure 74: Darcy Horizontal Cut Plot, Pore Gradient Profile.....	106
Figure 75: Day 2 Construct Extraction from Silicone Group	107
Figure 76: Static Control Aggregated Construct	107
Figure 77: Day 2 Construct, Distant Pore Group.....	107
Figure 78: Trimmed Construct Demonstrates Complete Bead Infiltration	108
Figure 79: Re-perfusion of Constructs Demonstrates Potential for Anastomosis	108

List of Abbreviations

bFGF – Basic Fibroblastic Growth Factor

BTE – Bone Tissue Engineering

CAD – Computer-Aided Design

CAM – Calcein AM

CDC – Center for Disease Control

ECM – Extracellular Matrix

EPC – Endothelial Progenitor Cell

EH – Ethidium Homodimer-1

FBS – Fetal Bovine Serum

HIV – Human Immunodeficiency Virus

hMSC – Human Mesenchymal Stem Cell

ID – Inner Diameter

MMP – Matrix Metalloproteinases

OD – Outer Diameter

PBS – Phosphate-Buffered Saline

PDGF – Platelet-Derived Growth Factor

PVA – Poly(Vinyl Alcohol)

TGF- β – Transforming Growth Factor- β

TPS – Tubular Perfusion System

UV - Ultraviolet

VEGF – Vascular Endothelial Growth Factor

Chapter 1: Introduction

Clinicians and researchers are investigating new methods for repairing bone defects to meet the high demand for bone repair in the clinic. Currently, bone grafts are the most transplanted tissue.¹ Bone tissue defects are often attributed to elevated levels of stress associated with physical activity, obesity, and aging,¹ leaving a large portion of the population at risk. Each year, approximately 185,000 limbs are amputated in the United States alone.² Approximately 15 million bone fractures occurred worldwide in 2011, with nearly 10% resulting in nonunions.¹ The Food and Drug Administration classifies a fracture which fails to heal after nine months without intervention as a non-healing (i.e. critical) nonunion break³. Commonly, these nonunions exhibit a substantial displacement between the two fractured ends. This gap is said to be above the critical defect size if it is so large as to not allow for natural healing. Normally, bones broken with gaps below the critical defect size will fill the void naturally with proper non-surgical fixation (hard cast, splint, sling, etc.) of the fracture.

Nonunion fractures take an extended or indefinite time to heal, while typical fractures heal within a few weeks.⁴ Bone grafts and bone tissue engineering (BTE) strategies attempt to accelerate the healing process. Nonunions that require surgery to insert support materials can be complicated by infection, rejection of the implant, and revision surgery.⁴ Therefore, it is important to optimize these strategies to reduce potential physical and economic effects of these complications. Conservatively, about 10% of traumatic fractures result in a nonunion.⁵ In 2010, the CDC reported 342,030

hospitalizations in the United States due to extremity fractures with an average treatment cost of \$34,016.⁶ In these cases, surgical intervention is often needed to fully heal the wound through the use of artificial supports and bone grafts.

Transplanted human tissues used for bone regeneration may be derived from autologous sources (elsewhere in the patient's body) or donated allogeneic tissue (e.g. cadaveric tissue, living donors). Approximately 1 million grafting procedures are performed each year.⁷ Autografts are the gold standard for harvesting bone tissue for implantation^{3,8} because autologous tissues have osteogenic (bone growing), osteoinductive (bone inducing), and osteoconductive (bone infiltration) properties.³ Most commonly, surgeons remove a portion of the iliac crest and shape the explanted tissue for implantation elsewhere in the body.³ Regardless of harvesting site, introduction of a secondary defect site increases the risk for complications. This may include post-surgical pain, infection, and scarring at the donation site.⁵ Additionally, autografts are not possible for all patients and the maximum donation size is limited. The elderly, young, and sick may not be able to donate their own bone tissue for reimplantation, and up to 20% of patients experience complications from the harvesting procedure.⁸ Surgeons may also choose to inject the space with bone marrow, which has been shown to exhibit the necessary osteogenic and osteoinductive properties, but the clinical success of this has been limited and is insufficient for defects which require structural support.³

Cadaveric donors overcome one limitation of autologous transplants – constrained supply – by providing allogeneic bone structures capable of bearing load without the restrictions of donor site morbidity. Allografts are the most widely

available option for treating long bone defects.⁸ Fresh allografts are rarely used due to the potential for serious infections such as HIV and Hepatitis C and the presence of immunogenic factors.⁸ Therefore, allogeneic bone requires processing prior to transplantation to reduce the risk of disease transmission, which also decreases the desirable biological activity of the tissue.⁸ Specifically, allografts have lower osteoinductive signaling relative to autografts and lack osteogenic signaling, resulting in slower growth of new bone.¹ Still, the greater quantity of bone tissue available to surgeons allows them to pack allografts at higher density and promote osteoconduction.³ Even with the extensive processing, it is still possible for the transplant to be rejected.¹ Substitute materials can be engineered with highly reproducible and tunable properties, which make them a desirable substitute for bone tissue derived grafts.

Current clinical practices to heal long bone non-union defects primarily employ the Masquelet and Ilizarov techniques.⁹ The Masquelet technique involves the use of a temporary inert spacer to create and sustain a defined space in the bone, allowing a specialized membrane to form.^{10,11} After 4-12 weeks, the spacer is removed and the defect site is packed with autologous bone and allogeneic bone chips, with mechanical support provided by metal surgical hardware.¹¹ The Ilizarov technique involves external fixation of the defect site, mechanically separated over time to allow for distraction osteogenesis.¹² The main goal behind distraction osteogenesis is to continually extend the external fixation device as the bone heals, keeping the gap between the two fractured ends just below the critical defect size, thus allowing for natural healing over an extended period of time. This process results

in maximum healing rates on the order of 1mm per day, requiring the bulky external fixator to be worn for several months at a time.¹³ Both the Masquelet and Ilizarov techniques are complicated by substantial healing times and multiple surgeries,¹¹ and the risk of clinical failure due to infection and recurring injury^{9,12}.

Researchers are currently investigating *in vitro* strategies in an attempt to overcome the complications that arise as a result of the current clinical practices. Recently, research has shown much improvement in the field of bone tissue engineering that utilizes directed differentiation of stem cells to create osseous tissue constructs. A major complication of such constructs, however, is the lack of inherent vasculature. The research presented here demonstrates a novel, bottom-up approach to bone tissue engineering that lays out the foundation to create the first large-scale tissue constructs with inherent vasculature. Through the combination of a tubular perfusion system (TPS) bioreactor, computer aided design (CAD) and subsequent 3D printing and *in silico* modeling, we demonstrate the ability to create viable tissue constructs on the order of 20 cm³. To put this in perspective, a 2014 review of bioreactor systems, puts the largest bioreactor construct at only 10.721 cm³,¹⁴ or half the size of the base unit in our modular system.

Chapter 2: Review of Related Literature

Introduction

Vascular networks are a key component of any biological system. In fact, cells within the human body are restricted to a distance of 100-200 μm from the nearest capillary.^{15,16} Despite the overwhelming presence of vascular networks within the body, vascularization of implantable bone grafts remains a major limitation. Vascular systems provide cells with oxygen and glucose transport necessary for respiration, as well as an efficient means of waste removal.^{15,17,18} The human body has demonstrated the ability for vascular tissues to spontaneously invade implanted tissue.^{15,19} However, host vasculature invades from the outside of an implanted scaffold inward, and thus the time required to achieve sufficient vascularization depends on the thickness of the implant. Spontaneous vascular ingrowth has been measured on the order of a few hundred nanometers per day,¹⁹ thus requiring several weeks to vascularize even the smallest of constructs. During this time, implantable constructs quickly develop a necrotic core.^{15,17,18,20} Those cells that do not die experience extreme nutrient gradients, with cells on the periphery of the construct consuming much greater levels of nutrients than those cells embedded deeper within the core. The unequal metabolic rates cause cells to release different signals, thus resulting in non-uniform differentiation of stem cells in these constructs.¹⁹

The need to create inherent vasculature is clear, and there are many different vascularization techniques currently being developed. However, there are also many different cell culture and tissue engineering strategies used throughout research, and

many vascularization techniques are incompatible with certain tissue engineering strategies. Therefore, the first step in designing vasculature for bone tissue engineering is to determine which cell culture and construct formation strategy will work best for the intended application. The research presented here focuses primarily on the use of tubular perfusion system (TPS) bioreactors, and the vascularization techniques were therefore tuned for use within these systems.

TPS Bioreactors

Bioreactor Design

There are many different types of bioreactors currently being used in the field of bone tissue engineering (BTE) including spinner flasks, rotating wall systems, and perfusion systems. Though there are many different systems, they all seek to control the mechanical stimuli, and thus downstream pathways, on cells, as well as to regulate the cell culture media.²¹ Regulation of media helps provide adequate levels of nutrients and waste exchange to all cells uniformly, whereas mechanical stimuli primarily focuses on shear stress derived from the flow of media over the parts of the scaffold exposed to flow. In the body, bone reacts to, and remodels in the presence of, mechanical stimuli, as evidenced by the increased healing rates of bone in response to ultrasonic waves²². In *in vitro* environments, it has been hypothesized that shear stresses provide the bulk of this mechanical stimuli. Further, shear stresses on the order of 0.01 to 20 dyn/cm² have been shown to impact both stem cell differentiation and mineralization.²³ Therefore, many BTE bioreactor systems seek to expose human mesenchymal stem cells (hMSCs) to these levels of shear stress, in an attempt to

preferentially differentiate these cells down osteogenic lineages, as opposed to chondrogenic or adipogenic pathways.

While all of the previously mentioned methods of dynamic culture have shown benefits over traditional static culture, success has been modest in spinner flask and rotating wall bioreactors, due to the less-ordered nature of the systems.²¹ At its most basic form, a spinner flask bioreactor simply consists of a BTE scaffold submerged in a flask containing cell culture media. Mechanical stimuli and flow of media is then provided via convection created by the spinning of a stir bar at the base of the beaker. Similarly, a rotating wall bioreactor contains a BTE scaffold in a flask consisting of two concentric cylinders. Here, the flow of media is driven through the viscous effects of media in contact with the both the stationary inner wall, and the rotating outer wall. In both of these systems, convection of media is relegated to the periphery of the constructs, and, while advantageous as compared to static culture, they still require small-scale constructs to allow for full diffusion of the necessary nutrients to the core of these constructs.²¹ In fact, cell death is often observed in the core of scaffolds as close as 200 μm from the scaffold surface.²⁴

Perfusion bioreactors overcome many of the limitations of spinner flask and rotating wall bioreactors, but require a significantly more complex setup. A typical perfusion bioreactor is composed of a media flask, which feeds into a custom-fit reaction chamber, via a tubing circuit. The media is then perfused through a porous BTE construct through the use of a pump. These systems have demonstrated increased proliferation, osteogenesis, and chondrogenesis of stem cells as compared to static culture and other dynamic culture options.²¹ However, in order to ensure that

media perfusion actually occurs through the pores of the BTE construct, the scaffold must be press fit into a custom sized reaction chamber to eliminate any void space between the scaffold and the chamber walls. The inherent porosity of the scaffold further limits the effect of perfusion bioreactors. Conventional scaffold fabrication techniques including gas-foaming, particulate leaching, and freeze drying often result in highly porous scaffolds. However, due to the random nature of pore orientation in these scaffolds, pore interconnectivity typically limits the flow of nutrients.¹⁹ To overcome these limitations, a system is needed that can provide for increased perfusion of nutrients and increased shear stresses, while eliminating of the need for custom fit reaction chambers.

Advantages of a TPS Bioreactor

Tubular perfusion system (TPS) bioreactors overcome all three of these limitations through a unique design. In a TPS bioreactor, a single scaffold is replaced by several modular units, which remain separate entities during the initial growth and differentiation period. When the researcher is satisfied with the state of the cells within these modular units, they can be easily aggregated to create a single BTE construct.²⁵ Under the TPS design, these modular units are composed of alginate, a natural anionic polysaccharide derived from brown algae, due to its ability to self-assemble into spherical beads. Further, cells can be isolated as alginate is dissolved in the presence of a chelating agent.

Alginate consists of mannuronic and guluronic acid side chains.²⁶ Alginate assembles into the “egg-box” model in the presence of divalent cations, such as Ca^{2+} , due to the crosslinking of alginate chains driven by ionic interactions.²⁷ This allows

for cellular encapsulation within alginate beads. When a cell population that is homogenous within liquid alginate is exposed to divalent cations, typically calcium in the form of a liquid CaCl_2 solution,²⁶ the alginate spontaneously forms alginate gel. This allows for the encapsulation of cells within the gel. By exposing the alginate to calcium solution dropwise, spherical gel beads are formed, with bead diameter largely a function of needle size.²⁶

Individual cell-encapsulating alginate beads are then loaded into a reaction chamber that consists simply of a tube capped by connectors of size such that perfusion of media is allowed without allowing beads to escape from the chamber. By dividing one larger scaffold into several smaller, spherical, modular units, perfusion of media easily occurs in the void space between the beads. This additional perfusion serves a two-fold purpose. First, under this model each individual bead sees direct convection over its outer surface. This allows for dramatically increased transport of nutrients.²⁸ Alginate, while highly porous (~96%)²⁹ is not particularly permeable, having a Darcy permeability of only $1 \times 10^{-17} \text{ m}^2$.²⁹⁻³¹ This means that transport occurs primarily via diffusion. However, under this model, each individual bead represents a BTE scaffold. At the size scale of individual beads, nutrient transfer via diffusion is sufficient to maintain viability in each bead.²⁵ The second benefit is increased shear stress throughout the scaffold. By utilizing a number of modular units, the surface area is greatly increased as compared to a single scaffold of the same overall size. As previously mentioned, flow through the interior of beads will be minimal due to its extremely low Darcy permeability, however, cellular differentiation and mineralization within TPS alginate beads have been shown to increase with

increasing flow rate and viscosity, both of which increase shear stress, as evidenced by Equation 1. Where μ is the dynamic viscosity of the fluid and u is the fluid velocity. The effect of increased shear stress on the periphery of each bead is thought to enhance differentiation and mineralization of cells on the interior of beads via paracrine signaling.^{24,32}

$$\tau = \mu \frac{du}{dy} \quad (1)$$

After the growth and differentiation phase, individual beads are aggregated by simply filling the void space between beads with liquid alginate and then cross-linking this liquid alginate with CaCl_2 solution.²⁶ After sufficient mineralization, the alginate can easily be dissolved through the addition of a chelating agent such as ethyldiaminetetraacetic acid (EDTA), which binds the Ca^{2+} ions.²⁶ Due to the bottom-up design of the TPS bioreactor, construct size is limited only by *in vivo* vascularization requirements.

Tissue Engineering Strategies for Vascularized Constructs

All living cells require nutrients for sustained growth and viability. In the body, diffusion of oxygen is limited to only 100-200 μm .^{15,16,19} Despite recent advances in bone tissue engineering, this diffusion requirement has relegated clinically used implants to thin or avascular tissues which can be vascularized by spontaneous host-capillary invasion, such as skin and cartilage.¹⁹ To address the need for large-scale tissue constructs, several vascularization techniques are currently under investigation, both *in vitro* and *in vivo*.

The most common component of engineered vascular constructs is the presence of endothelial cells³³⁻³⁶. These cells are a major component of native vascular tissues, and form a confluent monolayer which line vascular networks providing an effective barrier to prevent hemorrhage while allowing for nutrient exchange. Briefly, vascular networks are formed via a three-phase process. First, endothelial progenitor cells (EPCs) differentiate and proliferate to form the early stages of a capillary network. After this phase, which is also known as vasculogenesis, angiogenesis occurs. During this phase, endothelial cells release matrix metalloproteinases (MMPs) which serve to degrade the extracellular matrices (ECMs) surrounding the primitive networks formed during vasculogenesis. As the ECM degrades, proliferating endothelial cells migrate into the void, remodeling and elongating the network to form blood vessels. Finally, these blood vessels are remodeled and enlarged into larger vessels and arteries in a process called arteriogenesis.¹⁹

For thin constructs, there is little need for a vascular network prior to implantation. Hypoxic conditions within constructs trigger the release of angiogenic growth factors, and this, combined with the host inflammatory response, triggers spontaneous host-capillary invasion which provides sufficient vascularization for thin grafts, such as skin.¹⁹ Current vascularization strategies are being used in conjunction with this natural response in an attempt to provide sufficiently perfused vascular constructs.

One such technique, termed *in vivo* prevascularization, provides implants with a vascular network that spans the major axis of a construct. This allows for direct

microsurgical anastomosis of the construct to host vasculature, and thus immediate perfusion of the construct. However, this technique requires that a host undergo two separate surgeries. First, the BTE construct is implanted into a healthy region of the body with a major artery. Over a time span of several weeks, the graft and the axial vasculature of the artery merge, and once the vascular axis within the graft is sufficient, it is removed from the implant growth site and inserted into the defect site.¹⁹ While this technique overcomes many of the major limitations of vascularization within BTE constructs, the requirement of two surgeries, as well as the removal of a major vascular axis from the initial implant site are significant drawbacks. In particular, the requirement for an axial vascular network to be removed from the initial implant site places limitations on the size of the implant, because as construct size increases, the removal of the initial implant becomes more dangerous.

Another promising approach utilizes *in vitro* prevascularization. Under the right conditions, EPCs can be directed to differentiate into endothelial cells and form vascular networks. Several design strategies include the addition of growth factors such as vascular endothelial growth factor (VEGF), basic fibroblast growth factor (bFGF), platelet-derived growth factor (PDGF), and transforming growth factor β (TGF- β), among others, to stimulate the formation and remodeling of vascular networks. However, adding in too much of a growth factor can cause issues which include hemorrhagic vessels, and undesirable differentiation of seeded cells.¹⁹ While these strategies result in spontaneous, random microvascularization of constructs they are not sufficient as standalone techniques for complete vascularization of large scale

constructs. Therefore, both *in vitro* and *in vivo* prevascularization techniques are often combined with other scaffold-based techniques.

Scaffold-based BTE must be carefully tuned to optimize construct survivability and functionality. Specifically, scaffolds must be significantly porous to allow for the migration of endothelial cells necessary to form vascular networks.³⁷ One significant challenge to scaffold-based vascularization is the difficulty of creating interconnected pores. In many systems, a high porosity is not enough to ensure pore interconnectivity.¹⁹ Furthermore, as porosity increases, scaffold mechanical properties and integrity decrease, reducing the capability for use in load-bearing defects. There are many ways to create porosity within scaffolds. Particulate leaching involves the dispersion of a particle within a polymer resin. The polymer is then solidified, resulting in a scaffold with solid particulates randomly dispersed throughout. The scaffold is then exposed to a solvent that will dissolve the particulate, but not the scaffold.³⁷⁻³⁹ However, due to the random distribution of particulates, pores are rarely interconnected. This results in reduced cellular migration, but also residual particles, which raise cytotoxicity concerns. Another popular technique is freeze-drying⁴⁰, or lyophilization. Under this system, hydrogels are rapidly cooled, causing phase separation. After sublimation of the solvent under a vacuum, void spaces left in the hydrogel act as pores.³⁷ This method results in many of the same challenges caused by particulate leaching, specifically, a lack of pore interconnectivity. A third technique that results in a similar porous architecture is gas foaming. Under this method gas bubbles are formed either through a chemical reaction, or by placing the gas-saturated polymer in a high pressure environment. The

resulting bubbles displace the polymer scaffold, resulting in void spaces which form pores.³⁷ Commonly, sodium bicarbonate is homogenized within the polymer resin, forming CO₂ bubbles as it decomposes in the presence of an acidic environment induced after the polymer scaffold has been formed.³⁷ When endothelial cells are introduced to scaffolds with sufficient pore interconnectivity, these techniques can result in randomly arranged microvasculature. However, without a major vascular axis, complete perfusion after implantation takes weeks.¹⁹

To combat many of the issues of these methods, 3D printing is often utilized. Here, there are two primary ways in which 3D printing techniques are used to create vasculature in BTE constructs. First, porosity and vascular channels can be created simply by utilizing printing techniques that leave user-defined voids for pores and vascular channels. The second method, which is also the method most commonly used, is sacrificial molding. This technique does not require that molds be 3D printed, but they often are, providing highly reproducible molds.

Several methods of 3D printing are used to create scaffolds with user-defined geometries and pore structures. These techniques largely serve the same purpose, with the major differences being the types of materials that can be used with each technique, and the resolution that each method offers. In the broadest sense, 3D printing can be broken down into two primary techniques, stereolithography and extrusion. Stereolithography involves the use of a liquid polymer resin and a light source. Here, the light source can either be visible light, or ultraviolet (UV) light, depending on the polymer. This technique requires that the polymer have side chains, such as methacrylate groups, which crosslink when exposed to a beam of light. Here,

highly focused light causes crosslinking of the photopolymer in a layer-by-layer fashion. Porosity can then be user defined either through the use of CAD files⁴¹, or by simply blocking the light path in certain areas, either by addition of particles in the resin, or by simply covering up portions of the glass through which the focused light passes.²⁰ Major limitations of a stereolithographic approach include cell death caused by UV light, the requirement that polymers be photo-crosslinkable, and scaffold thickness limitations based on the max depth of light penetration.²⁰ Major advantages include relatively quick and hands-off production, good resolution, and a high degree of reproducibility.⁴²

Extrusion based printing, which includes techniques such as fused deposition modeling (FDM) and fused filament fabrication (FFF), involves the layer-by-layer addition of material. Extrusion occurs either by drawing the material through a nozzle (FFF), or simply by applying pressure to force the material through a nozzle (FDM). Under an FDM system, the temperature of both the print head and build platform can be highly controlled to allow for multiple material types. Here, the polymer is placed at a temperature that allows for extrusion, while keeping it viscous enough to maintain strand integrity. By tuning the applied pressure and print head movement speed, strand diameter can be carefully controlled. Then, polymer fibers are deposited layer by layer onto a build plate, where the temperature is such that the resulting structure solidifies, with porosity controlled by adjusting strand diameter and spacing, as well as the angle at which each subsequent layer is applied. Under this system, UV crosslinkable photopolymers can also be used by simply curing each layer with UV light before the next layer is applied. While highly reproducible, this technique is

limited by a relatively large resolution, which is driven by the minimum strand diameter, a function of the print nozzle diameter. Further, this technique is limited by the strength of attachment of each layer to the next, as well as the imperfect alignment of each rounded strand to the rounded strand in the previous layer.

For these reasons, sacrificial molding is the most commonly utilized technique for creating vasculature in BTE constructs. Sacrificial molding involves the creation of a user-defined vascular mold. These molds can either be formed by printing a mold within a hydrogel to be filled with a sacrificial material, or by forming the scaffold around the sacrificial template. Major limitations of sacrificial molding include cytotoxicity of sacrificial materials¹⁸, and the challenges associated with creating relevantly sized, interconnected vascular channels. Further, sacrificial molding requires that scaffolds maintain their shape after the network material is sacrificed, which eliminates the possibility of using sacrificial molding within a TPS bioreactor.

Perhaps the most common method of creating sacrificial networks is solvent cast molding. Here, a soluble material such as poly(vinyl alcohol) (PVA),¹⁸ is poured into a mold with the desired shape. The cast is then allowed to solidify, and the tissue construct is built up around it. Once the construct is complete, the cast is sacrificed by simply exposing the construct to a solvent which will selectively dissolve the cast. Alternatively, certain cast materials can be sacrificed at elevated temperatures. These methods are limited by the properties of the sacrificial material, as they must be durable enough to withstand the process of generating the construct, while at the same time be easily sacrificed under conditions that are not harmful to the construct or the cells encapsulated within them. Common sacrificial materials include PVA,¹⁸ carbohydrate

glasses,^{43,44} sugar-based fibers,^{15,45} sodium alginate,⁴⁶ gelatin⁴⁷, and fugitive inks (Pluronic F127, etc.)^{17,48}.

Another way to create sacrificial channels within BTE constructs is through the incorporation of electrospun fibers. Electrospinning is the process of nanofiber formation driven by an electric current applied to a fluid jet composed of a polymer dissolved in a solvent.⁴⁹ Electrospinning, commonly combined with a polydimethylsiloxane (PDMS) scaffold,⁴⁹ allows for the formation of a complex nano-channel network. Electrospun fiber materials can then be sacrificed in a variety of ways, such as the dissolution polyethylene oxide⁴⁹ and pullulan⁵⁰ fibers in water. Additionally, fibers formed by any number of other means can be encapsulated within a polymeric scaffold and sacrificed either manually⁵⁰ (requires that channels not be interconnected), through the addition of a solvent, or by the application of heat⁴⁹.

Despite the vast array of different vascularization strategies currently under investigation, relevantly sized BTE constructs remain largely avascular. Furthermore, the majority of the vascularization techniques produce vasculature on the micro-scale. However, the diameter of the human femoral artery ranges from about 6 mm to about 10 mm,⁵¹ highlighting the need to create vasculature of much larger proportions. Therefore, a significant need exists to identify strategies that will allow for the vascularization of large-scale BTE constructs. Promising techniques involve a combination of multiple different strategies, along with the natural, spontaneous vascularization that occurs upon implantation.

Oxygen in the hMSC Niche

In vivo oxygen concentrations have long been known to influence cellular respiration, proliferation, and viability. Recent studies have examined the influence of oxygen concentrations on hMSC differentiation. Unfortunately, many of these studies yielded conflicting results, demonstrating the complexity of oxygen interactions in the body. It is, however, typically agreed that an increasing cell density results in a decreased specific oxygen consumption rate.⁵² Additionally, studies within cardiac tissue have shown that cell viability decreases linearly with oxygen concentration, while cell density decreases exponentially.⁵³ These results were driven not only by decreasing viability with decreasing oxygen, but also decreased proliferation rates. As previously mentioned, capillaries provide the bulk of oxygen transport to cells, and it is for this reason that the maximum distance from each cell to the nearest capillary is typically limited to 200 μm .^{15,16,54}

Atmospheric air consists of 20.95% O_2 , or roughly 160 mm Hg⁵⁵. By the time inhaled oxygen reaches arterial blood, these levels fall to about 7-12%,^{56,57} and fall to less than 5% in venous and capillary blood⁵⁶. Further, interstitial oxygen levels within human tissues and organs range from around 2-9%,^{55,56} while average oxygen tensions within healthy bone marrow range from 6-7%⁵⁶⁻⁵⁸. Cells within BTE constructs under dynamic culture have been shown to live for up to seven days at oxygen levels just below 4%, whereas identical constructs under static culture yielded 0% central oxygen concentrations in only five days, and marked cell death.⁵⁴

It is generally thought that low oxygen tensions (5%) favor chondrogenesis,^{53,55,59} whereas 2-5% O_2 allows hMSCs to maintain an

undifferentiated state^{55,59}. At the same time, long term exposure to oxygen tensions below 1% result in massive levels of cell death.⁶⁰ Several studies have shown the inhibitory effects of low (2-3%) oxygen concentrations on both osteogenesis and chondrogenesis as compared to groups cultured at 21% oxygen.^{59,61} On the other hand, primary mouse osteoblasts cultured in 2% oxygen were shown to overexpress hypoxia-inducible factor α (HIF α), resulting in developed bone tissue that was much more dense and highly vascularized than cells that did not express HIF α .⁶² Similarly, an analysis on oxygen concentrations and the differentiation and proliferation of embryonic chick limb bud mesenchymal cells demonstrated an optimum oxygen concentration of 5%.⁵⁷ It was further reported that rat MSCs cultivated in 5% oxygen yielded more bone mass than cells at 20% oxygen.⁵⁷ Still, other studies have shown little difference in osteogenic differentiation in cells cultured in 2% oxygen as compared to cells cultured in 21% oxygen.⁶³ This study did, however, demonstrate the inhibitory effects of oxygen concentrations below .02%. Furthermore, temporarily induced hypoxia (less than 4% O₂) has been shown to upregulate VEGF expression in MSCs as the cells attempt to develop vasculature to relieve their hypoxic state.⁶⁰

These conflicting results demonstrate the complex nature of the oxygen-hMSC interaction. This broad spectrum of results is hypothesized to be a result of the wide range of cell types, lines, and culture techniques used in these studies. With no clear choice of optimal oxygen concentration, the best method is to ensure that constructs are able to survive at *in vitro* oxygen levels equal to those of the desired implant site.

Chapter 3: Development of Vascular Networks for Large Bone Tissue Constructs

Introduction

With nearly 15 million bone fractures¹ and 1 million bone grafting procedures⁶⁴ worldwide, and 185,000 limb amputations in the United States each year², there is a large clinical need for relevantly sized tissue engineered alternatives. Conventional techniques have so far been limited to tissue engineered constructs of less than 11 cubic centimeters,¹⁴ or about the size of an adult human pinky. Current research is limited by the need to embed large scale BTE constructs with the necessary vasculature for long-term graft functionality.

The TPS bioreactor provides many advantages over both traditional static culture and the many different means of dynamic culture. Under the TPS model, increased proliferation, differentiation, and mineralization have been observed.^{25,32} Furthermore, due to the bottom-up approach utilized by the TPS model, there is no limit on maximum construct size. Rather, the only limitation is the lack of a sufficient vascular network. Due to the unique nature of TPS bioreactors, many conventional methods of creating vasculature, notably sacrificial molding and scaffold-based design, are not applicable. Therefore, a novel approach must be utilized. Here, a biomimetic vascular network was created using stereolithography 3D printing in conjunction with the TPS bioreactor. Previously, constructs designed in the TPS model suffered the same diffusion limitations as traditional methods, and developed necrotic cores when grown to clinically relevant sizes. By incorporating a rigid

vascular structure, aggregated alginate constructs were successfully re-inserted to a TPS bioreactor. Due to the presence of a major vascular axis and a highly porous branched network that minimized the distance of each cell from the nearest nutrient source, aggregated constructs on the order of 20 cm³ were observed to be viable after 24 hours.

Materials and Methods

SolidWorks Geometry Generation

The use of stereolithography and other 3D printing techniques are advantageous not only because of the high degree of accuracy that they produce, but also because they allow any lab to reproduce the results of another, as long as they have access to the same computer-aided design (CAD) files. However, the CAD files must first be developed. Here, SolidWorks was utilized to create all structures to be printed. First, concept drawings were created that began and ended with a single inlet and outlet, respectively. This would allow for easy, direct anastomosis to existing host vasculature. In between the inlet and outlet, a series of branching is necessary to ensure that diffusion limitations are overcome. Final network design consisted of three vertical branches, each of which split into three more horizontal branches, for a total of nine branches. This system allowed for the greatest degree of symmetry, which would help to ensure uniform viability and differentiation. Ultimately, the center-most branch was removed, as it provided a direct path for fluid flow, and thus prevented flow from being evenly distributed throughout all of the other branches.

This change also served to free up space in the interior of the network to allow for a greater number of alginate beads to be encapsulated within the design.

Bioreactor tubing was chosen to be $\frac{3}{4}$ " inner diameter (ID), and this, combined with the 3.5 mm diameter of the alginate beads (Appendix A, determined via a microscopic pixel count analysis), was the driving force behind the overall geometry of the network. The outer diameter (OD) of the inlet and outlet branches was chosen to be 3.0 mm. This choice served a two-fold purpose. First, it allowed for the connection of the $\frac{1}{8}$ " tubing that would supply the flow of media, and second, this size would allow for the anastomosis to relevantly sized host vasculature. The overall length of the network was limited by the length of the printer build platform, or approximately 70 mm. Once all of the design parameters were known, the actual CAD model could be developed, as seen in Figure 1.

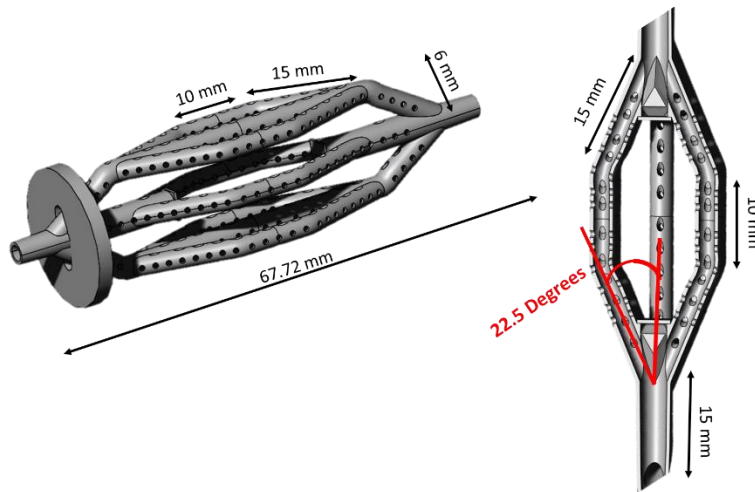


Figure 1: SolidWorks Design

To achieve the highest degree of symmetry, one quarter of the network was built, and then mirrored about two axes to create one whole network. First, a line diagram of the quarter network was drawn using the 3D sketch tool in SolidWorks.

Each horizontal branch was designed to be 22.5° from the center branch, and each vertical branch was 6 mm from the centerline (50° vertical branch angle). As previously mentioned, inlet and outlet channels featured 3 mm outer diameters to allow for connection to bioreactor tubing. After branching, the eight interior branches featured 2.4 mm outer diameters. These diameters, combined with the 6 mm vertical spacing between vertical branches, left 3.6 mm of void space, which is just enough to allow for the 3.5 mm alginate beads to infiltrate the network. The 22.5° horizontal offsets were also chosen to allow the beads to fill in the void spaces. Individual branches were formed by executing a surface loft of individual circles following the profile designed in the 3D sketch tool. Branches were then given thickness using the “thicken” tool. A thickness of 400µm was utilized to ensure printability (200µm wall thickness resulted in branch separation during printing). Internal horizontal and vertical bifurcation and trifurcation aids were created to allow for uniform flow through each branch, as seen in Figure 2.

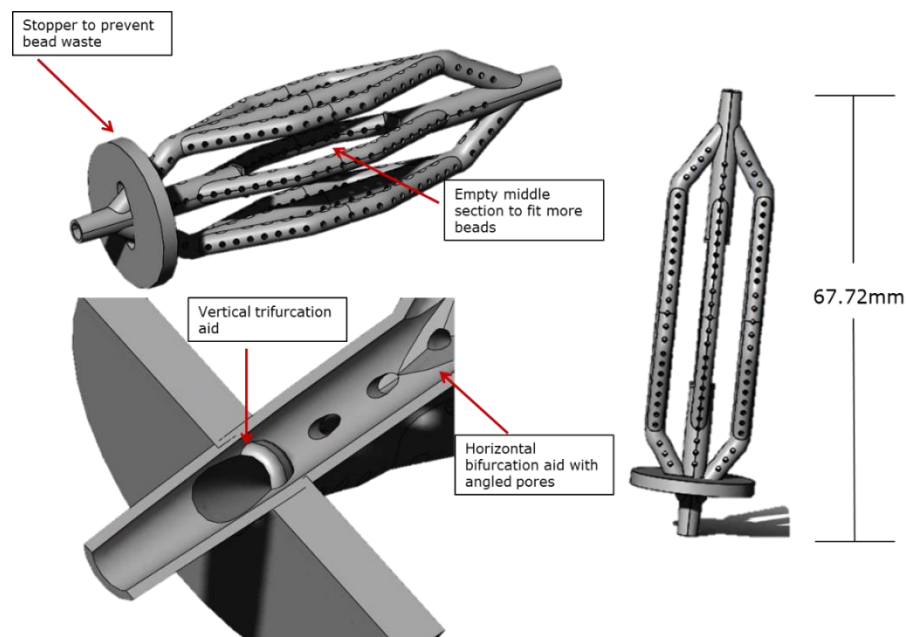


Figure 2: Network Design

Pores were added to each branch using the simple, 2D “Boss/Extrude” tool. Using this tool, pore diameter and spacing could be readily tuned. Pores of 500, 750, and 1000 μm were printed. Ultimately, 750 μm pores were chosen, as this gave the best pore size to network integrity ratio (user preference based on print post-processing skill). Pore spacing, a user-defined variable, was determined through COMSOL simulations. The bead stop disk was also created using the “Boss/Extrude” tool. This bead stop was designed to prevent unnecessary bead waste that was observed between the tubing connectors and the start of the vascular network.

Custom designed connectors (Figure 3) were also needed to allow for the system to be housed within the 3/4" tubing, while at the same time allowing for the connection of 1/8" tubing to the actual network design. These custom connectors feature a 1/4" OD channel which allows for easy external connection to bioreactor tubing. This then expands to 3/4" to provide an adequate seal which prevents the leakage of media from the reaction chamber. The connectors then feature a 1/8" OD channel for connection to the perfusion network.

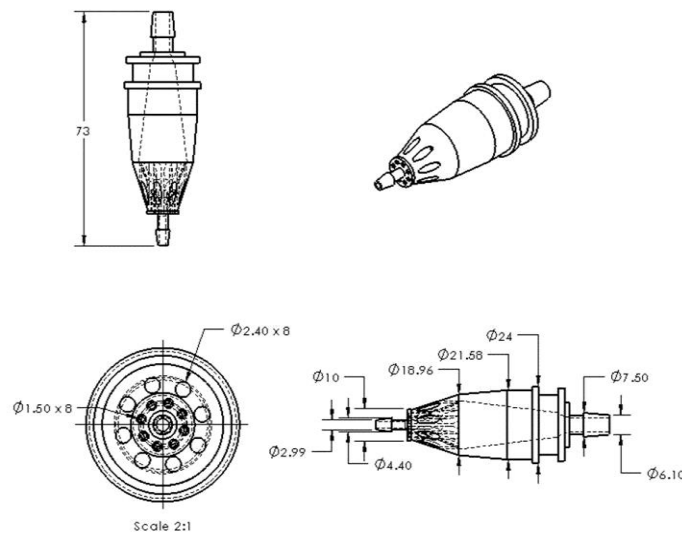


Figure 3: Custom Designed Connector – Units Displayed in mm

Connectors to be used at the inlet featured a solid exterior, whereas outlet connectors featured the same overall geometry, but contained pores in line with the outlet flow (Figure 3) to prevent media stagnation at the outlet.

The final combination of connectors and the perfusion network resulted in a system that allowed for the direct perfusion of media throughout the interior of the designed network (Figure 4). The network was then surrounded by hundreds of alginate beads which filled the void space left not only between the outer edges of the network and the reaction chamber tubing, but also the void space between the exterior of adjacent horizontal and vertical channels.

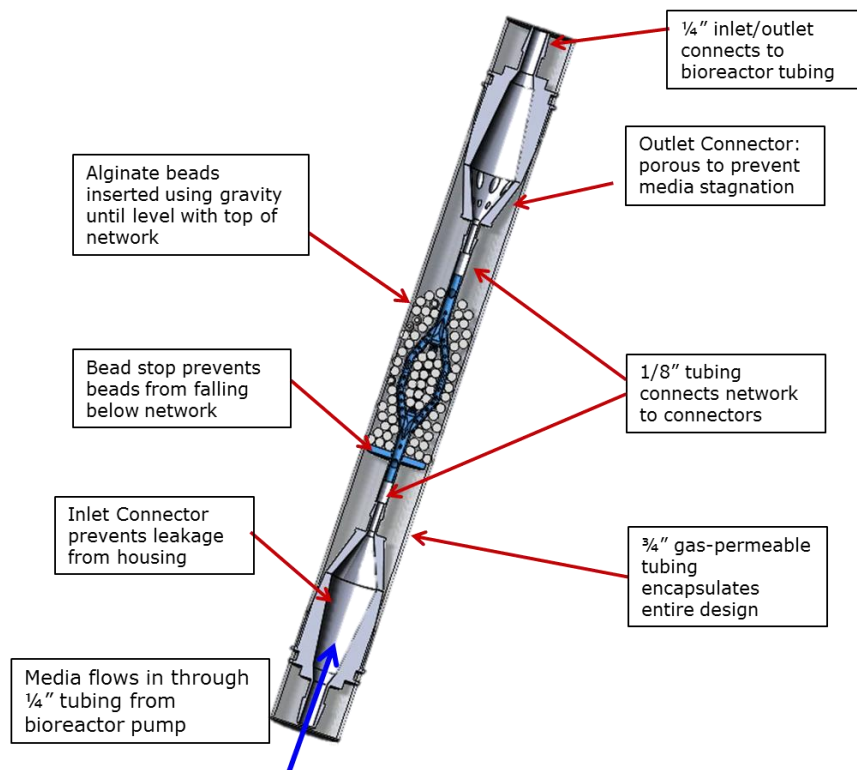


Figure 4: Bioreactor Network Design

COMSOL Mass Transport Analysis

COMSOL is a commercial multiphysics software that utilizes finite element analysis to solve complex transient and steady state equations. As the porosity within

the designed perfusion network increases, so does mass transport of oxygen, waste, and essential nutrients, due to the increased surface area of alginate exposed to media. However, porosity and mechanical integrity are inversely proportional, and therefore, a mass transport analysis is necessary to determine the optimal porosity. It was hypothesized that an increase in porosity and a decrease in the distance from each bead to the nearest pore would result in increased oxygen concentrations throughout the BTE constructs. This hypothesis was tested through a wide array of COMSOL models. Here, the diffusion of oxygen throughout the construct was modeled in 2D using COMSOL's "Chemical Species Transport, Transport of Diluted Species" module. The effects of convection and diffusion on pre-aggregation "free" beads have previously been shown to provide necessary levels of oxygen to encapsulated cells.^{25,28} For this reason, these COMSOL studies focused on convection and diffusion throughout the aggregated construct. Furthermore, alginate, while highly porous, has very low permeability ($k=1 \times 10^{-17} \text{ m}^2$ ²⁹⁻³¹). The relationship between flow rate and permeability is given by Darcy's Law (Equation 2).

$$Q = -\frac{kA}{\mu} \frac{\Delta P}{L} \quad (2)$$

Where Q is the flow rate, μ the dynamic viscosity of the media (0.78 centipoise)²⁵, L is the length, and ΔP is the pressure drop. Previously, flow rate through a single bead was calculated to be $3 \times 10^{-7} \text{ mL/min}$.²⁴ Based on this minimal flow rate, and taking into consideration both the free flow path that the printed network allows the media and the complete size of the alginate construct, convection through the aggregated construct was neglected. COMSOL convection and diffusion equations (Equation 3),

based on Fick's Law, are therefore simplified, as the fluid velocity, u , is assumed to be zero.

$$N_i = -D_i \Delta C_i + C_i u \quad (3)$$

Where N_i is the flux (mol/m²-s) through material "i", D_i is the diffusivity of material "i", and C_i is the concentration of the diffusing species within material "i".

Due to the presence of metabolically active cells within each alginate bead, a nutrient sink exists within the model. This sink is modeled through Equations 4 and 5, where Equation 4 is the Michaelis-Menten reaction kinetics equation, and Equation 5 is the concentration sink equation utilized by COMSOL.

$$R_i = N_0 \frac{C}{C + K_{MM}} \quad (4)$$

$$\Delta(-D_i \Delta C_i) + u \Delta C_i = R_i \quad (5)$$

Here, R is the rate of consumption of oxygen (mol/m³-s), N_0 is the oxygen consumption rate (0.012 μ mol/10⁶ cells/h)²⁵, and K_{MM} is the Michaelis-Menten saturation constant (0.011 mol/m³)²⁵. It is important to note that the user must define R as a negative value, since it represents a consumption rate. It is also worth noting that, while the entire space confined between the tubing and the network should be modeled as alginate, only the beads themselves should be modeled as metabolically active. Converting the oxygen consumption rate to relevant units yielded a consumption rate of 1.45×10^{-5} mol/m³-s. For this analysis, networks that yielded oxygen concentrations below .04 mM (4% O₂) were considered to be non-functional. This number was selected based on the concentration of oxygen in human capillary blood (~5%),⁵⁶ in human tissues/organs (~2%-9%),^{55,56} and in bone marrow (~4%-7%)⁵⁷. While research has demonstrated conflicting information on the effect of low

oxygen tensions on MSC differentiation, and it is generally accepted that low oxygen tensions favor chondrogenesis to osteogenesis,⁵⁹ the effect of these low oxygen concentrations on differentiation was not taken into account. This can be justified by the results of several experiments which demonstrate increased osteogenesis and proliferation^{25,26,32} pre-aggregation. Therefore, post aggregation oxygen concentrations need only support cell viability, as constructs will only be aggregated after significant differentiation and mineralization have occurred.

The diffusivity of oxygen was modeled as $2.56 \times 10^{-9} \text{ m}^2/\text{s}$ in media, and $2.08 \times 10^{-9} \text{ m}^2/\text{s}$ in alginate.²⁵ Media, which is contained in a flask constantly exposed to air and travels through 1/8" gas-permeable tubing, was assumed to be saturated water 37 °C and 0.21 mol/m^3 , as calculated from Henry's Law (Equation 6) and the Van't Hoff equation (Equation 7).

$$C_{aq} = \frac{P}{K_H} \quad (6)$$

$$K_H(T) = K_H(T^*) \exp \left[-\frac{\Delta H_{sol}}{R} \left(\frac{1}{T} - \frac{1}{T^*} \right) \right] \quad (7)$$

Where C_{aq} is the concentration of oxygen dissolved in media, P is the partial pressure of oxygen in air, K_H is the Henry's Law constant, ΔH_{sol} is the enthalpy of dissolution, R is the universal gas constant, T^* is 298 K, and T is 310 K (37 °C). All calculations can be found in Appendix B. Henry's Law constants and enthalpy of dissolution values were obtained from the National Institute of Standards and Technology.

The air-saturation assumption further served to allow for the pores to be modeled by simply imposing constant surface oxygen concentrations of 0.21 mol/m^3 at each pore. Similarly, a constant surface concentration was imposed on the outer boundary of the reaction chamber tubing. The EShell network, was modeled as non-

permeable ($D = 1 \times 10^{-100} \text{ m}^2/\text{s}$) to provide modeling for even the least permeable materials.

To mimic an *in vivo* environment, low-permeability fluorinated ethylene propylene (FEP) tubing was obtained (McMaster-Carr), in addition to the highly permeable silicone rubber (Cole-Parmer) tubing typically used with TPS bioreactors. Diffusivity values were converted (Appendix B) from permeability values given by the respective manufactures. The resulting diffusivity values were $4.174 \times 10^{-11} \text{ m}^2/\text{s}$ for FEP and $2.357 \times 10^{-8} \text{ m}^2/\text{s}$ for silicone.

Geometries were generated to represent 2D models of the printed network, as well as a single-channel design. This single channel was designed to mimic the worst case scenario of a TPS bioreactor with no vascular network. Due to the low permeability of alginate, a single tube must be created, even in this worst case scenario, or the back pressure will cause the tubing to explode.

Finally, the mesh settings were set to “Physics-controlled mesh” with individual mesh element size set to “normal”. These settings resulted in a total number of mesh elements on the order of 360,000 over an area of 1248 mm^2 . Visual inspection of these settings, as well as a comparison of results generated from differing mesh element sizes determined that these settings resulted in an acceptable degree of accuracy within a reasonable calculation time.

SolidWorks Flow Analysis

COMSOL helped to develop a keen understanding of the effects of porosity on diffusion, but a key phase of any TPS bioreactor is the pre-aggregation flow. In order to ensure uniform proliferation and differentiation, care should be taken to

ensure that flow profiles are roughly the same in all experimental groups. It was hypothesized that perfusion network design will have little effect on the pre-aggregation viability of cells encapsulated within alginate beads, provided that each bead see some degree of convection. To test this hypotheses, 3 major groups were examined. First, the entire network was examined with a 1.5 mm center-center pore spacing. This distance represents the minimum pore spacing (maximum porosity) that can be achieved while still allowing for the user to be able to print and trim the networks. A full network with a 9 mm center-center distance was examined to gain an understanding of the effects of the minimum porosity, within reason, of a branched network on flow profiles. Finally, a single tube with pores every 9mm was created, once again to mimic the worst case scenario. It was also crucial to ensure that flow was uniformly distributed throughout each branch of the branched network. This was achieved by running several flow simulations and tweaking the size of the bifurcation/trifurcation aids until flow profiles were uniform.

Computational fluid dynamics (CFD) analyses could then be run utilizing the SolidWorks “Flow Simulation” add-in. SolidWorks develops accurate flow profiles by solving the Navier-Stokes equations for conservation of energy, mass, and momentum, using a finite volume analysis. A unique feature of CFD in SolidWorks is that it automatically determines the fluid volume, making it easy to set up. Further, because CAD models were originally designed in SolidWorks, there was no need to convert files or create entirely new files. However, SolidWorks CFD does require that all fluid volumes be fully constrained, so that the software can determine flow paths. Therefore, an outer shell of 3/4” ID was created using simple 2D extrusions. This

shell was made to be the same length as the network (67.72 mm), and was mated with the network in a SolidWorks assembly to fix their relative positions. Once mated, the network and the outer shell shared a longitudinal axis, as seen in Figure 4, and both parts inlets and outlets were aligned. Outer shell caps (3/4" diameter) were then created, once again using simple 2D extrusions. These caps were mated to the inlet and outlet ends of the outer shell, effectively containing the fluid volume. Finally, a 3 mm diameter cap was created and mated to the face of the inlet to the perfusion network. This cap, though it overlapped with the inlet outer shell cap, served to allow the inlet flow to be constrained to only the network, as opposed to the entire outer shell.

Boundary conditions were then imposed, assuming fully developed flow. A flow rate of $450 \text{ mm}^3/\text{s}$, or 27 mL/min, was imposed as the inlet boundary, and environmental pressure (1 atm) was imposed as the outlet boundary condition. This 27 mL/min flow rate was determined based on an optimal flow rate of 3 mL/min that had previously been used in TPS bioreactor design.²⁵ This 3 mL/min flow rate optimized the trade-off between shear stress and bead degradation. However, this flow rate was for a 1/4" ID system. Scaled to a 3/4" ID system, 27 mL/min achieves the same average fluid velocity (Appendix B). Furthermore, this flow rate is comparable to *in vivo* arterial flow rates.⁶⁵

Finally, flow of media was modeled as water at 37 °C, gravity was imposed to account for the vertical orientation of the reaction chamber within the incubator, and mesh resolution was set to "5". This resolution value was determined to give the best results within a reasonable time. Even so, average calculation time was about 2 hours.

After flow profiles of each group were observed, the flow of media through aggregated alginate was examined. An aggregated alginate construct was modeled by using the SolidWorks “mold” tool to create an exact mold of the network. To do this, all pores were first suppressed, and the network was cut in half along the longitudinal axis to allow for the use of “shut off surfaces” required by the mold tool. A half mold was created, and then mirrored about the cut plane to create a full mold. Then, the mold was mated with the flow assemblies created previously, carefully ensuring that all network pores were present once again. Using SolidWorks “porous media” module, an alginate material was defined using the Darcy permeability characteristics previously mentioned and added to the SolidWorks material library. This newly created material was then assigned to the mold. From here, all boundary conditions, media properties and resolution setup was the same as previously mentioned.

Experimental Group Determination

Taking into account the results of both the COMSOL aggregated diffusion studies and the SolidWorks pre-aggregation CFD studies, 5 experimental groups were determined to test the two-fold hypothesis. This hypothesis was that the perfusion network design will have no significant pre-aggregation impact on the viability of cells encapsulated within alginate beads, provided that each bead sees some degree of convection, while post-aggregation viability will be a function of oxygen concentration throughout the construct, and therefore porosity and distance of each bead from the nearest pore. First, a static control was utilized. This group featured cell-encapsulated alginate beads cultured in 6-well plates until Day 1, upon which they were aggregated and incubated in a 50 mL Falcon tube. This group is referred to

as “Static Control” in all relevant graphs and tables. All other groups were cultured in a TPS bioreactor. The second group featured a single channel with pores every 9 mm, once again to simulate the worst-case TPS scenario. This group is referred to as “Single Tube” in all relevant graphs and tables. A full network with pores every 9 mm (referred to as “Distant Pore”) was utilized to validate COMSOL results as compared to a full network with pores every 1.5 mm (referred to as “Close Pore”). These three groups were cultured in FEP tubing to mimic the *in vivo* environment, where gas exchange on the periphery of these constructs would be limited. Finally, the fifth group featured a full network with pores every 1.5 mm housed in highly permeable platinum-cured silicone, to demonstrate the *in vitro* efficacy of these constructs. This group is simply referred to as “Silicone” in all relevant graphs and tables. The results of this group, in conjunction with the Close Pore group, would serve to demonstrate both elevated efficacy when culture *in vitro*, but also the feasibility to survive in an *in vitro* environment.

3D Printing

All 3D printing was completed using a Digital Light Processing (DLP) stereolithography printer (EnvisionTec). A clear polymer, EShell 300 (EnvisionTec) was chosen for both the perfusion network, and the connectors. EShell 300 is a clear, photocrosslinkable polymer, due to the functionalization of both acrylate and methacrylate groups. Tuned by the manufacturer for use with EnvisionTec DLP printers, it provides resolutions on the order of 100-150 μ m, and is designed as a bioinert polymer for commercial hearing aid manufacturing.

First, CAD files of networks and connectors were imported as .stl files to Magics, an STL editor software. Parts were rotated and translated as necessary to align them to the build plate. They were then “fixed” using the built-in features of Magics to correct overlapping geometries, holes, etc. From here, support structures were generated within Magics. Support structures attach to the print files, and allow for rounded structures to adhere to the build platform, and ensure that separate branches and pores do not collapse onto each other during the build process. Part files and support structures were then imported to Perfactory RP (EnvisionTec), a software which allows the user to translate .stl files to the proper format to be used with Perfactory printers. Here, parts can be angled and rotated to allow for optimal use of build platform space. Additionally, build style is selected here. The EnvisionTec default build style for EShell 300 was used, with a step size of 50 μm .

The Perfactory 4 (EnvisionTec) was the DLP printer utilized for all prints. Ensuring that the projector light type was set to “UV,” the intensity was calibrated to 180 mW/dm^2 , as is recommended by the manufacturer. A 48-field calibration was used to achieve the highest degree of accuracy. Once calibrated, the flat calibration plate was exchanged in favor of the material tray, which features silicone rubber walls to allow for the containment of the liquid EShell 300 resin. From here, files were transferred to the printer, and the printer was left to run its course. The build plate was wide enough to allow for any combination of two separate files (two connectors, two networks, one connector and one network, etc.) to be printed at one time, as seen in Figure 5. Build time ranged from four to six hours.

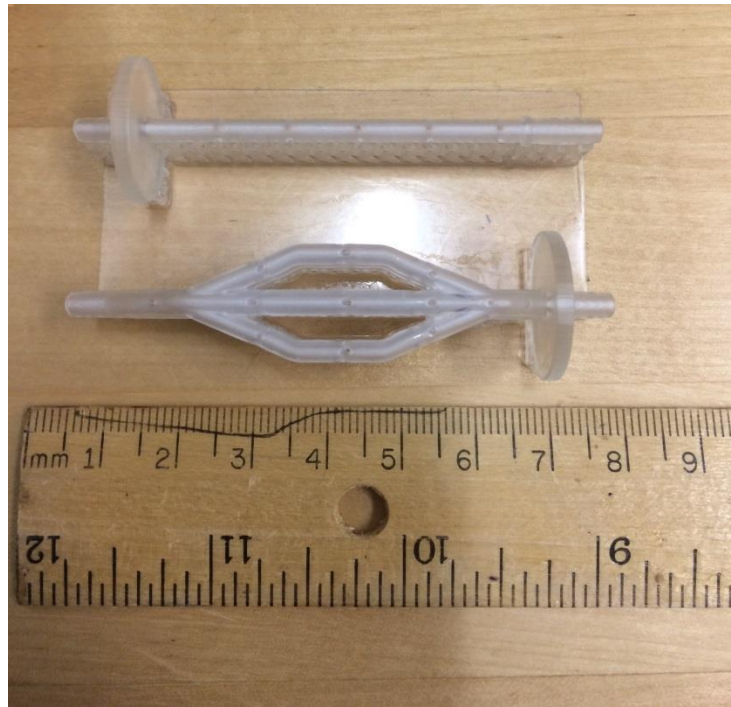


Figure 5: Two Designs Printed Simultaneously

Once the printer finished, the build platform was raised and prints were removed from the build platform using a putty knife. At this point, prints were soft-cured, meaning that they maintained their shape, but were still very soft and sticky to the touch due to the presence of partially cured polymer. Prints were cleaned by spraying them gently with 99% isopropanol, and then placed into an isopropanol bath on a shaker platform for approximately 15 minutes. This cleaning process served to remove excess polymer, and ensure that pores and channels were not occluded.

Following the cleaning process, parts were dried with compressed air, and support structures were trimmed using a razor blade and an X-ACTO knife. Parts were washed and dried again, and cured through the application of 4000 flashes in a light polymerization chamber (EnvisionTec). Remaining support structure debris was

then sanded down to yield smooth surfaces. Support structures can be seen in Figure 6.

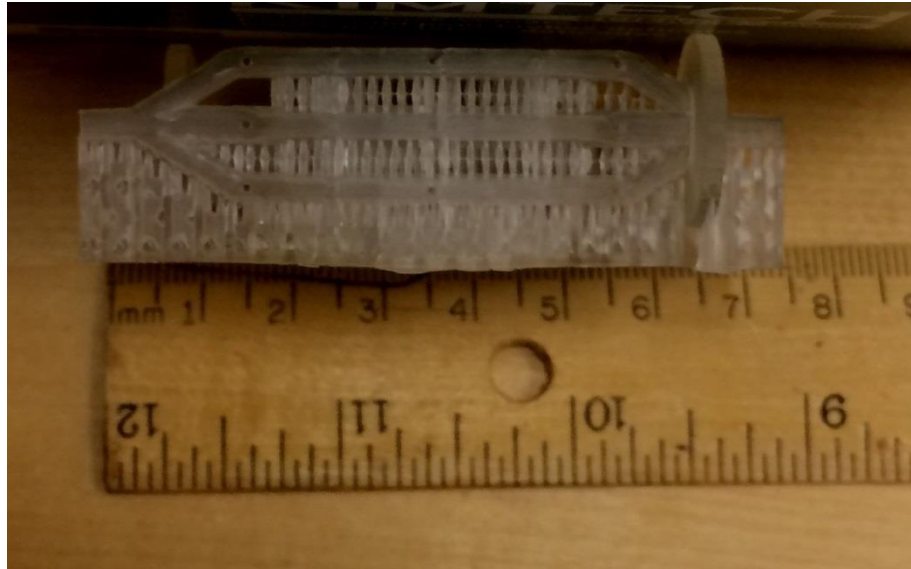


Figure 6: Soft-Cured Network, Complete with Support Structures

EShell Sterilization

EShell parts cannot be autoclaved, and were thus sterilized following a sterilization-rehydration protocol. First, five sterile beakers were sprayed with 70% ethanol and transported to a sterile hood. Similarly, an unopened 1 gallon jug of 100% ethanol was sprayed into the hood, along with sterile phosphate-buffered saline (PBS, pH 7.4). The five beakers were filled with five different solutions (one each), of 100% PBS, 25%-75% ethanol-PBS, 50%-50% ethanol-PBS, 75%-25% ethanol-PBS, and 100% ethanol. All parts to be sterilized were submerged in 100% ethanol and exposed to UV light for 15 minutes. Then, parts were gradually rehydrated in PBS by soaking them in increasing percentages of PBS, for five minutes per beaker, all while exposed to UV. Once the parts reached the final, 100% PBS, solution, they

were removed using sterile tweezers and stored submerged in PBS in sterile 50 mL Falcon tubes.

Alginate Bead Formation

Liquid alginate (2% w/v) was prepared by first creating a buffer solution of 0.025M HEPES and 0.15M NaCl in Milli-Q water. The solution was then buffered to pH of 7.4. Alginic acid sodium salt (Sigma) was then added to a beaker containing the buffer solution to obtain 2% w/v. The alginic acid was dissolved into the solution through the use of a stir bar. At the same time, the entire system was heated to 60 °C to aid in the dissolution of alginate. Clumps were broken up periodically using a laboratory spatula. Once completely dissolved, the liquid alginate solution was autoclaved for 45 minutes on a liquid cycle. The autoclaved solution was then transferred into a sterile hood where it was filtered into 50 mL Falcon tubes using 3 mL syringes to force alginate through .22 µm sterile filters. Sterile alginate was stored at 4 °C until ready to use (maximum 5 days). 0.1M CaCl₂ (Milli-Q water) solution was created, buffered to pH 7.4, and sterile filtered through a .22 µm filter.

Human mesenchymal stem cell (hMSC) (RoosterBio) pellets were centrifuged at 200 x g for 10 minutes and resuspended in alginate at 37 °C to achieve roughly 130,000 cells per bead following Equation 8.

$$\frac{Cells}{mL} \times \frac{1mL}{30 Beads} = \frac{Cells}{Bead} \quad (8)$$

A beaker was filled with approximately 10 mL of sterile CaCl₂ for each mL of alginate. This solution was gently stirred using a stir bar. Following resuspension, cell-encapsulated beads were created by adding the cell-alginate solution to 0.1M CaCl₂ dropwise using an 18 gauge needle from a height of about 6 inches above the

CaCl₂ solution (Figure 7). This height allows for the formation of spherical beads (will be tear-drop shaped if dropped from too low due to the high viscosity of alginate). Beads were left to self-assemble for 15 minutes. Excess CaCl₂ was drained, and beads were poured into the bioreactor reaction chamber by removing the outlet connector. The outlet connector was then reattached, and the system was tapped gently to allow the beads to settle and completely fill the void space between branches.

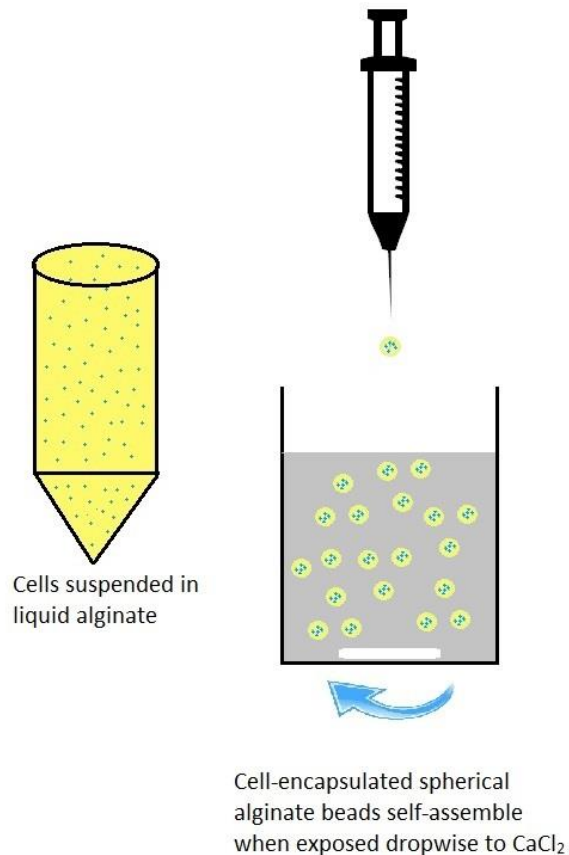


Figure 7: Alginate Bead Formation

Cell Culture

3 million bone marrow-derived hMSCs (RoosterBio) were thawed and plated into a Corning 2-Stack (Sigma) according to RoosterBio Starter Kit Expansion Protocols.

Briefly, 1 vial of hBM-MSC Media Booster GTX was added to each 500 mL quantity of hBM-MSC Basal Medium (RoosterBio). This combination will henceforth be referred to as simply “high performance media.” The frozen cell vials (1 million cells each) were thawed in a 37 °C water bath until only a sliver of ice remained. The vials were sprayed with 70% ethanol and transferred into the hood, where cells were aseptically transferred into one 50 mL Falcon tube per vial. 4 mL of high performance media at room temperature were added dropwise to the cells in each tube. Cells were centrifuged at 200 x g for 10 minutes. The supernatant was removed and cells were resuspended in 45 mL each of high performance media. These cells were then seeded into the 2-Stack, and high performance media was added to bring the total volume to 250 mL. After four days, cells were washed with 50 mL sterile phosphate-buffered saline (PBS, pH 7.4). PBS was aspirated, and cells were lifted by adding 50 mL trypsin-EDTA (Fisher). Trypsin was quenched with an equal volume of PBS + 1% Fetal Bovine Serum (FBS, Fisher). The cell suspension was transferred into 50 mL Falcon tubes, and centrifuged at 200 x g for 10 minutes. Supernatant was aspirated, and the cell pellets were resuspended into 100 mL fresh high performance media. The cell suspension was then plated into a Corning 10-Stack (Sigma), and high performance media was added to bring the total volume to 1.5 liters.

After 4 more days, cell pellets were isolated following the same procedures as above, but requiring 250 mL each of PBS to wash, trypsin-EDTA to lift, and PBS + 1% FBS to quench. Total cell count reached 400,000,000 (determined via a trypan blue exclusion assay). These cells were then suspended equally into 100 mL of

alginate, to achieve a seeding density of approximately 130,000 cells/bead (Equation 8).

Perfusion and static culture media for use with encapsulated alginate beads was Dulbecco's Modified Eagle Media plus 10% FBS, 1% antibiotic-antimycotic 1% non-essential amino acids and 2% L-glutamine (all components from Fisher).

Bioreactor Setup

A Masterflex L/S peristaltic pump (Cole-Parmer) drives the flow of media throughout the bioreactor. Masterflex two stop L/S 14 tubing is fed into the pump. All tubing and connectors were first autoclaved, with the exception of EShell parts, which were sterilized as described above. Using appropriate 1/8-1/8" connectors, 1/8" ID tubing extends from both ends of the pump tubing. As seen in Figure 8 (page 41), one end is fed into the media flask, which is stopped with a rubber stopper with two holes for tubing. The other end extends as necessary and is connected to a short (~ 2 in) section of 1/4" ID tubing. This tubing feeds into the custom printed EShell connectors. A short (~ 2 cm) section of 1/8" tubing connects the EShell connectors to the printed network. A second, similarly sized section of 1/8" tubing is attached to the outlet connector. The 3/4" reaction chamber tubing (FEP or platinum-cured silicone) is then slid over top of the inlet connector/printed network assembly. Alginate beads are then poured in from the top until they become level with the end of the outlet channel. Once this chamber has been filled with alginate beads, the outlet connector is carefully added such that the 1/8" tubing that was pre-assembled on the connector fits over the outlet of the printed network. Another 2 inch section of 1/4" tubing is attached to the outer end of the outlet connector. This is then connected to a length of 1/8" tubing, which is

fed into the remaining slot in the flask stopper. All four bioreactor groups were run in parallel on the same pump (Figure 9). Once set up in a sterile hood, the entire system is then transported to a cell culture incubator at 37 °C, with 5% CO₂ where the reaction chamber is suspended vertically to allow for the removal of any air bubbles by gravity. Each experimental group had its own separate media flask, filled with 250 mL of perfusion media as demonstrated by Figure 9, which features the complete setup installed into the incubator at 37 °C. All groups saw a flow rate of 27 mL/min.

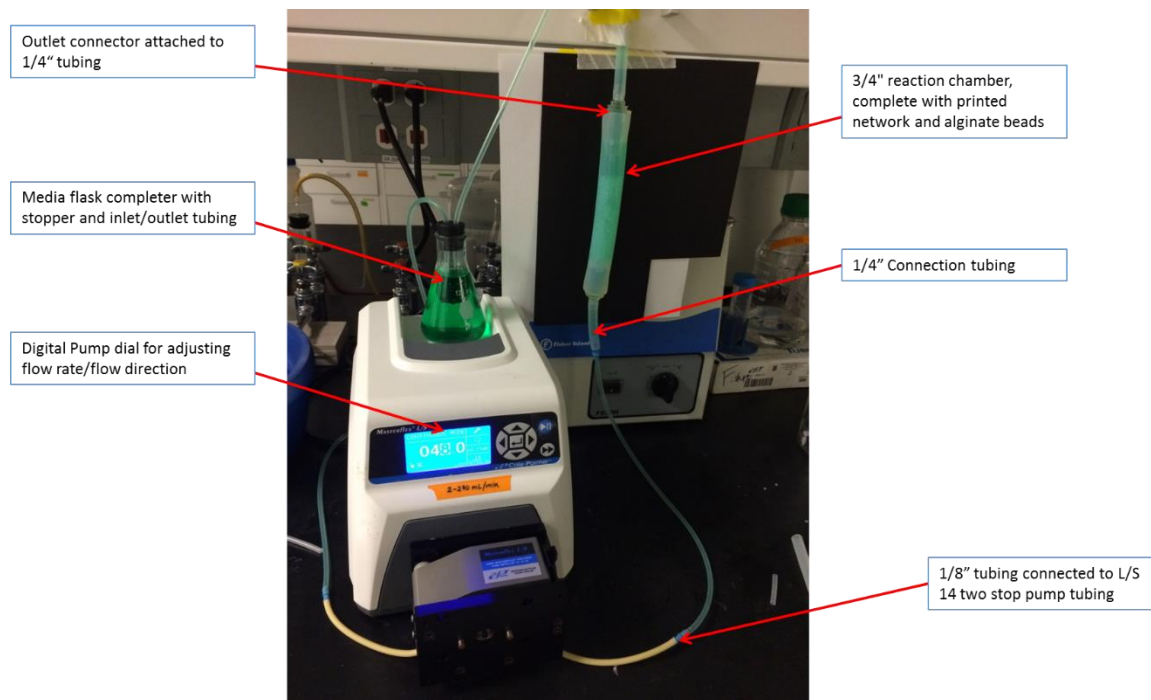


Figure 8: Bioreactor Setup



Figure 9: Bioreactor Setup Featuring 4 Experimental Groups in Parallel

Construct Aggregation

Constructs were aggregated within the reaction chamber using a two-syringe method, similar to double-barrel syringe epoxy techniques. Here, two separate syringes were used due to space constrictions. First, the outlet connector was removed, exposing the alginate beads. Then, using a 10 mL syringe complete with 18 gauge needle, acellular alginate at 37 °C is injected in increments of 10 mL by carefully sliding the needle down the void space between the inner chamber wall and the nearest bead. This liquid alginate is prepared and sterilized in the same manner as above. Following each alginate injection, 10 mL of 0.1M CaCl₂ is carefully injected in a similar manner. Any excess CaCl₂ that rises above the level of alginate beads is carefully aspirated. This technique is performed 3-5 times, allowing a 5 minute period for alginate gel formation in between each injection. After the final injection of alginate and CaCl₂, the system was left to aggregate for 15 minutes. Once satisfied with the aggregation,

the outlet connector was reattached, and the entire system transported back to the incubator where it was perfused again.

The statically cultured beads were aggregated by placing a 3 inch section of platinum-cured silicone rubber tubing on a sterile surface. Statically cultured beads were then placed into this tubing. Once all of the beads had been placed, the construct was aggregated in the same manner as above. Once aggregate, the construct was placed into a 50 mL Falcon tube. The Falcon tube was then filled with media and placed into the incubator at 37 °C.

Viability Analysis

Beads were harvested at each of six harvest sites for each experimental group. The six locations were named bottom inner, bottom outer, middle inner (core) middle outer, top inner, and top outer. Here bottom, middle, and top refer to vertical distance from the inlet, while inner and outer refer to radial distance from the centerline.

Furthermore, in experimental groups featuring a full network, beads from the middle inner group were beads which filled the space in the dead center of the network.

Figure 10 visually displays the location of each harvest site.

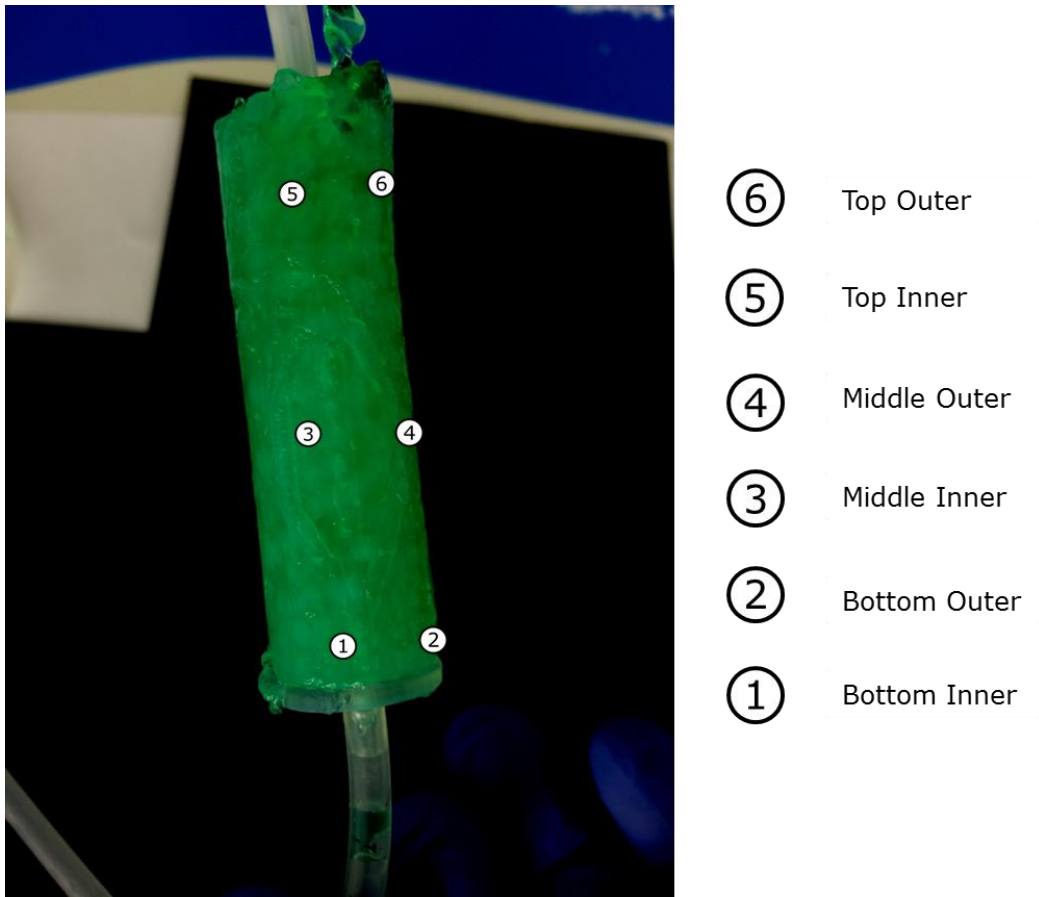


Figure 10: Harvest Sites

In order to harvest beads from the bottom of the TPS groups, the network was physical pulled out of the reaction chamber. To preserve non-harvested bead locations, non-harvested beads were poured into a 50 mL Falcon tube as they were removed from the reaction chamber. Once harvesting was complete, they were reinserted to their proper location by simply inverting the Falcon tube over the reaction chamber.

Each experimental group was assigned its own 6-well plate, and each well was labeled to allow for the proper segregation of beads from each harvest site. Three beads were harvested from each site at 24 hours (n=3). Because statically cultured beads were cultured in 6-well plates at Day 1, harvest sites did not apply. Therefore,

beads were chosen and analyzed at random (n=3). After this initial harvest, the constructs were aggregated. After 24 hours of aggregation (48 hours from experiment start), beads from each harvest site were once again harvested (n=3). At this time point, harvest sites did apply to the static culture, and were therefore taken into account. In addition to the six harvest sites, beads were harvested for dead controls from each group (n=3). Dead control beads were soaked in 70% methanol for 15 minutes before aspirating the methanol.

Beads were then immersed in a solution of 1mM calcein AM (CAM), 2mM ethidium homodimer-1 (EH) (Fisher) in PBS. 1.5 mL was applied per 6-well plate (.25 mL per harvest site). Beads were then left to sit in solution for 30 minutes before imaging with a fluorescent microscope. This entire process was performed in a dark environment due to the photosensitivity of the CAM/EH solution.

Each bead was then imaged at both 2.5 x and 10 x magnifications. Live and dead images were saved to a computer and were then merged and counted using ImageJ software following the protocols in Appendix C. These protocols were written as macros, which not only saved time, but also ensured that each image was analyzed consistently. A few images, selected at random, were then counted by hand to verify the automated counting process.

Results were saved to Excel (Appendix A) and imported to Minitab for analysis. Using an ANOVA (one-way analysis of variance) test, combined with Tukey's test, statistical significance was determined. Results were then plotted, and can be found in Appendix D.

Results

Initial Bioreactor Setup

The bioreactor was first set up using acellular beads in a non-sterile environment. The reaction chamber was loaded with beads, and it was observed that approximately 20-25 mL of alginate, or 600-750 beads, was required to fill each reaction chamber. Once the beads were loaded, the bioreactor was perfused with deionized water. Once fully perfused, a few drops of green food dye were added to the flask of water. It was observed that the green dye diffused throughout the reaction chamber, with the exception of the space between farthest interior edge of the inlet connector and the beginning of the perfusion network, as demonstrated by Figure 11. It was for this reason that the bead stop described above was added into the design. Final network design, complete with bead stop and pores, is shown in Figure 12.



Figure 11: Perfusion of "Free" Beads by Green Food Dye



Figure 12: Final Network Design

Constructs were then aggregated according to the prescribed method. It was observed that approximately 20 mL of alginate was required to completely aggregate each construct. Following aggregation, as shown in Figure 13, constructs were reinserted to the bioreactor, and perfused again. This time, green dye was exchanged for pink, to allow for visual examination of dye diffusion. The construct was then perfused overnight. As illustrated by Figure 14, the dye diffused into the entire construct over a period of 24 hours.



Figure 13: Aggregated Alginate Construct

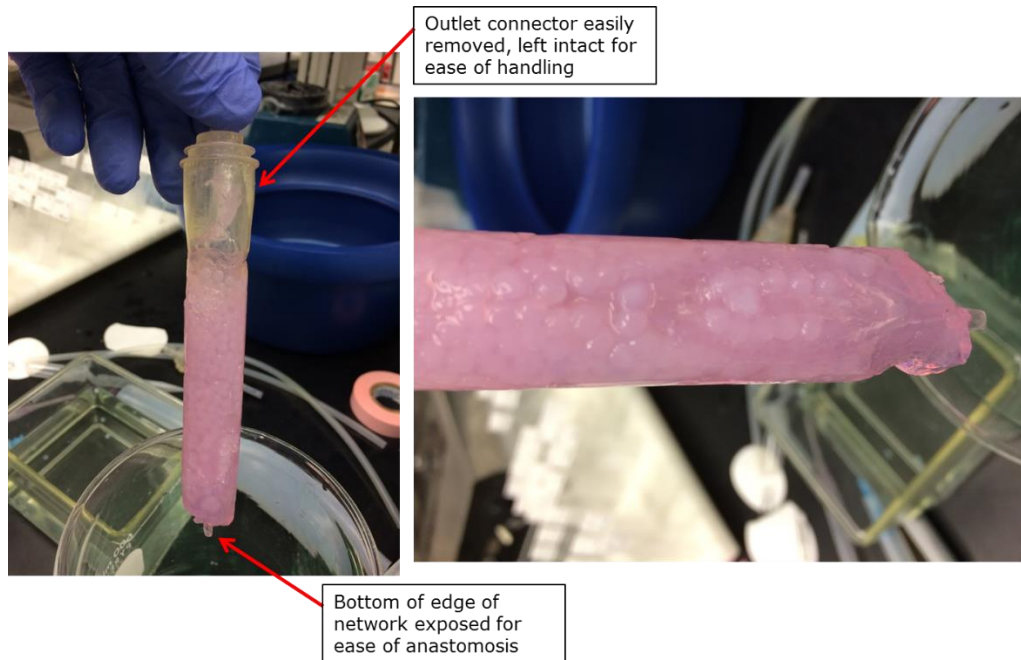


Figure 14: Rehydration of Aggregated Construct

COMSOL Diffusion Studies

COMSOL diffusion studies initially focused on the middle of the three vertical branches. That is, these studies first focused on the two channels that branch directly off of the inlet, and feature a large void space where the middle-most branch was removed. Due to the presence of the largest void space, this cross section has the largest chance to see the presence of dead cells. At the same time, due to the high degree of network symmetry about the longitudinal axis, it was determined to be redundant to model both horizontal and vertical cut planes.

Initially, the maximum porosity network, represented by a center-center pore distance of 1.5 mm was compared to the minimum (within reason) porosity network, represented by a 9 mm center-center pore spacing. These results, displayed in Figure 15 and Figure 16, demonstrate a clear difference in oxygen concentrations between

these two groups. However, it is important to note that, when modeled with platinum-cured silicone tubing as they are here, neither group falls below the 0.04 mM threshold at any point. In fact, the lowest value in the 9 mm spacing group is about 7% oxygen. The nice thing here is that due to the value of the Henry's Law constant at 37 °C (959.3 L-atm/mol), concentration in millimolar is roughly equivalent to percent oxygen values (4% O₂ = .0417 mM). It is also important to note that in all of the COMSOL images to be displayed, the scale on the x and y axes is in millimeters, and the rectangular nodes along the periphery of the channels represent the pores of the networks. In all images, red represents high oxygen concentrations, and blue represents low oxygen concentrations.

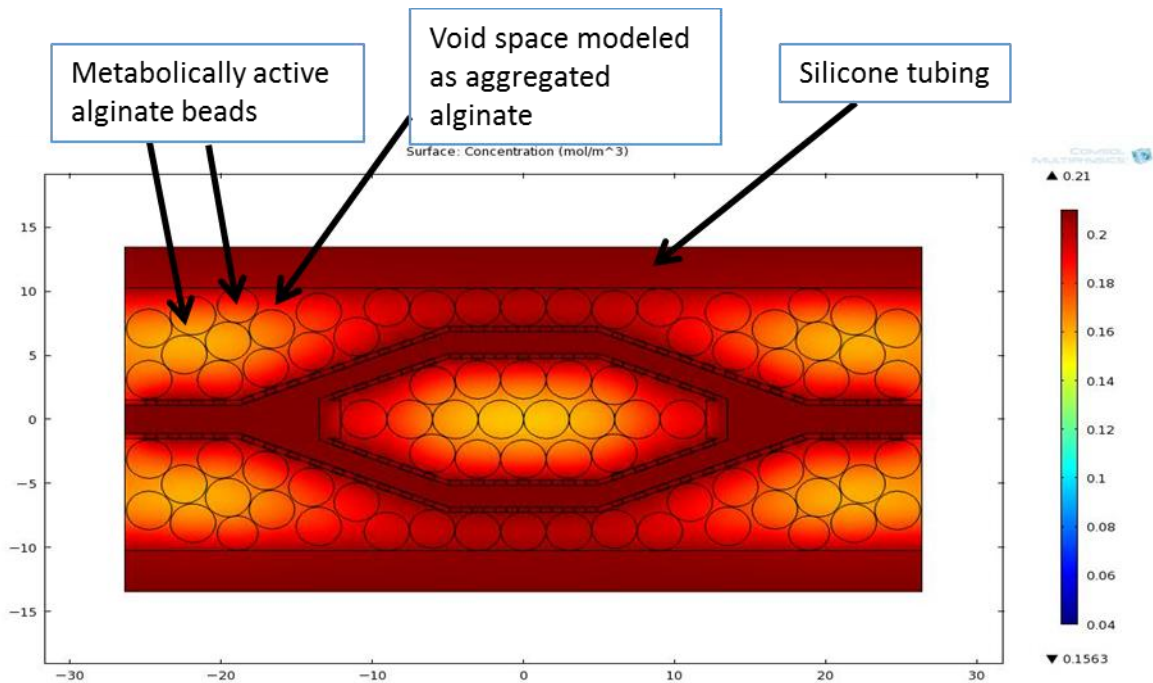


Figure 15: 1.5mm Pore Spacing Oxygen Concentration - Middle Branch, Silicone

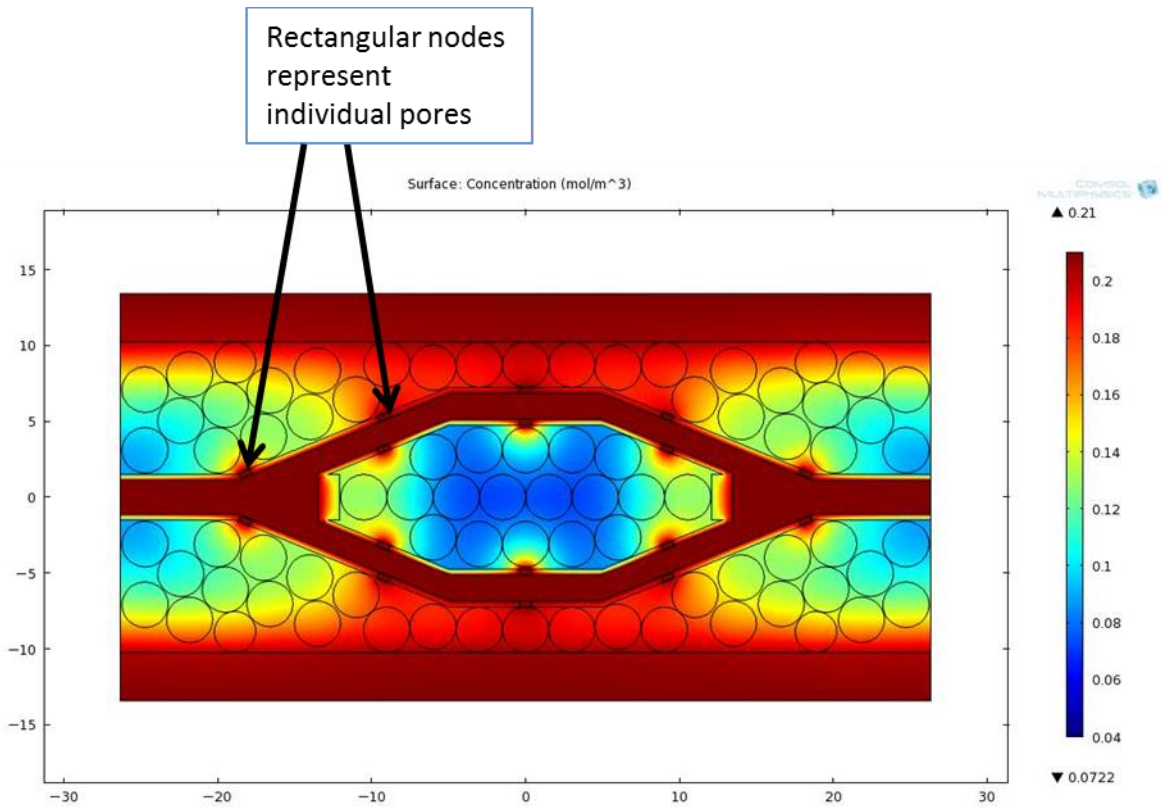


Figure 16: 9mm Pore Spacing Oxygen Concentration - Middle Branch, Silicone

Due to the prevalence of suitable oxygen values throughout, the effect of using a less permeable tubing was examined. These Results are displayed in Figure 17 and Figure 18.

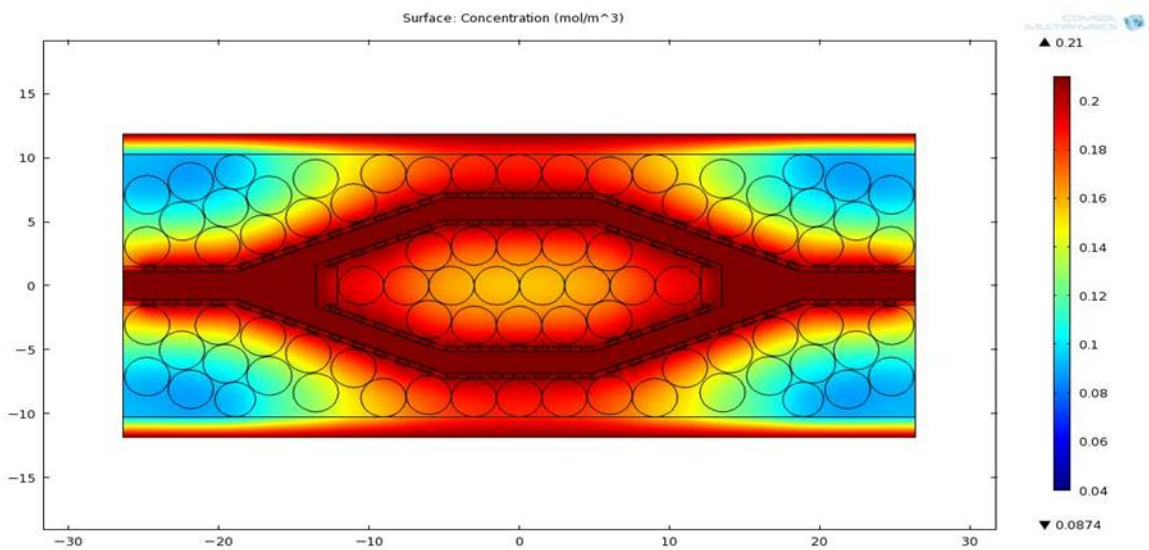


Figure 17: 1.5mm Pore Spacing Oxygen Concentration - Middle Branch, FEP

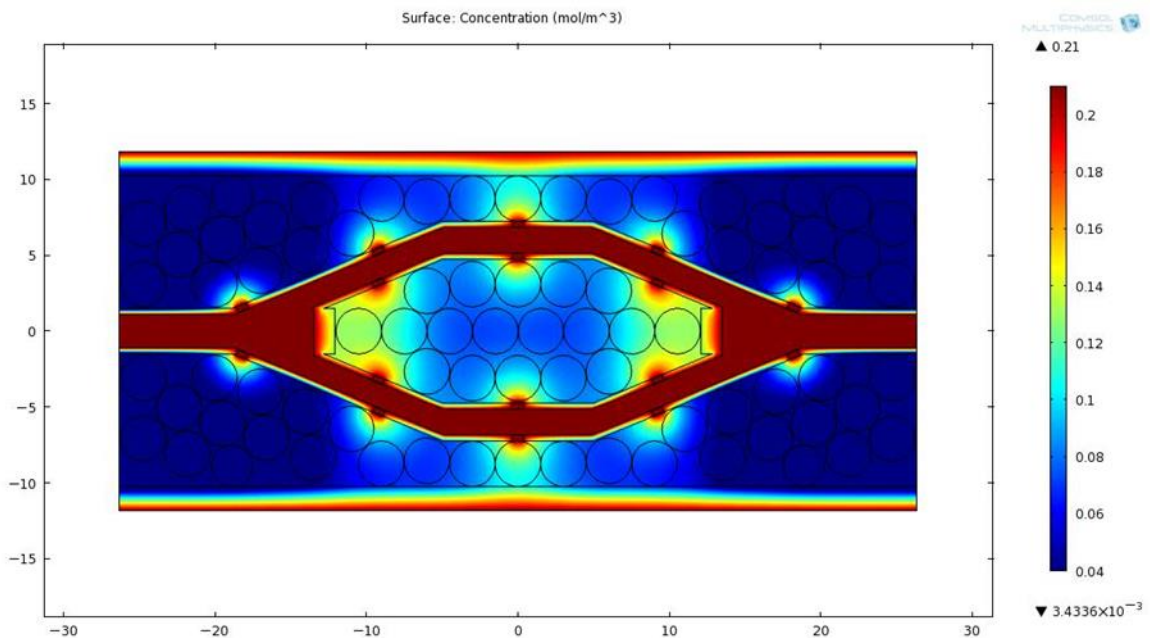


Figure 18: 9mm Pore Spacing Oxygen Concentration - Middle Branch, FEP

As demonstrated here, in a simulated *in vivo* environment, oxygen concentration nears 0% in the 9 mm pore spacing group.

Oxygen concentration was then examined in the upper and lower branches. Because they are identical, one model worked for both branches. These groups were similarly run using both silicone and FEP tubing, but as before, the silicone tubing provided so much oxygen content that the entire system contained healthy levels of oxygen. Therefore, only the FEP results are displayed below. For all graphs, including silicone tubing models, see Appendix E.

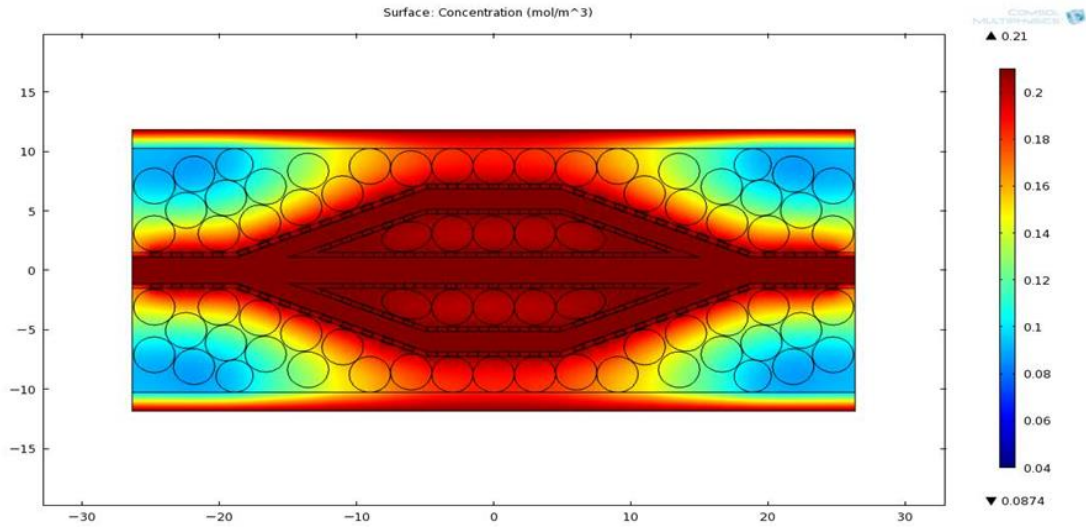


Figure 19: 1.5mm Pore Spacing Oxygen Concentration - Top/Bottom Branch, FEP

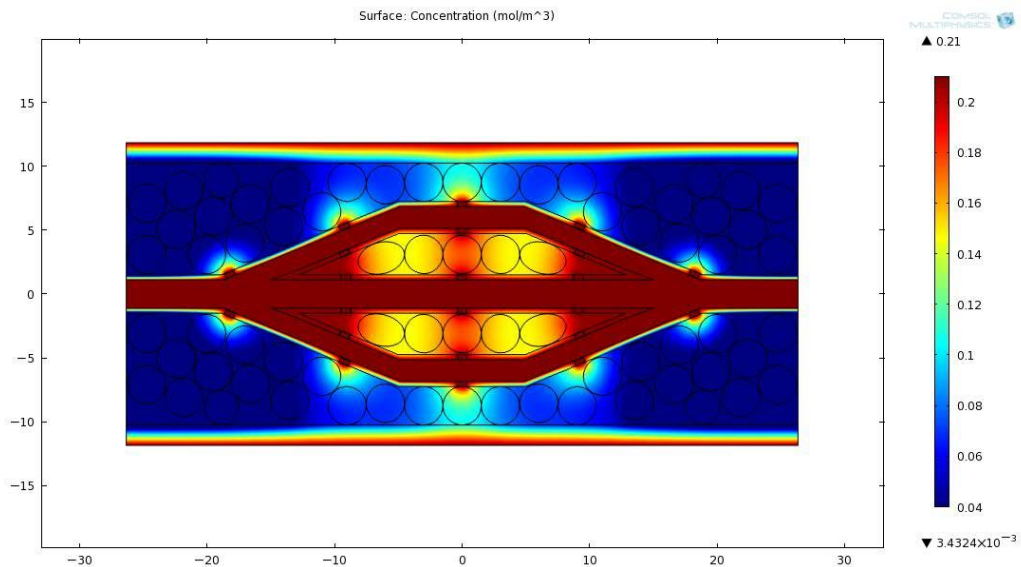


Figure 20: 9mm Pore Spacing Oxygen Concentration - Top/Bottom Branch, FEP

These models validate the assumption that middle branch analyses can serve to model oxygen concentrations in the interior due to their larger interior void space. Here, the exact same minimum oxygen concentrations are observed as in the corresponding middle group models. Once again, the 9 mm pore spacing concentration nears 0%.

With the extremes of network porosity measured, the next series of models was undertaken to determine the minimum pore distance at which oxygen concentration remains above 4%.

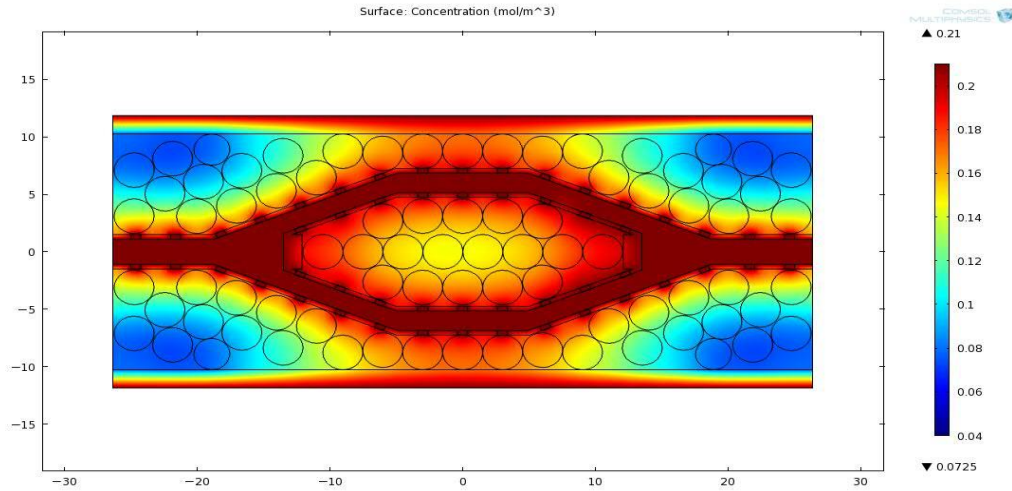


Figure 21: 3mm Pore Spacing Oxygen Concentration - Middle Branch, FEP

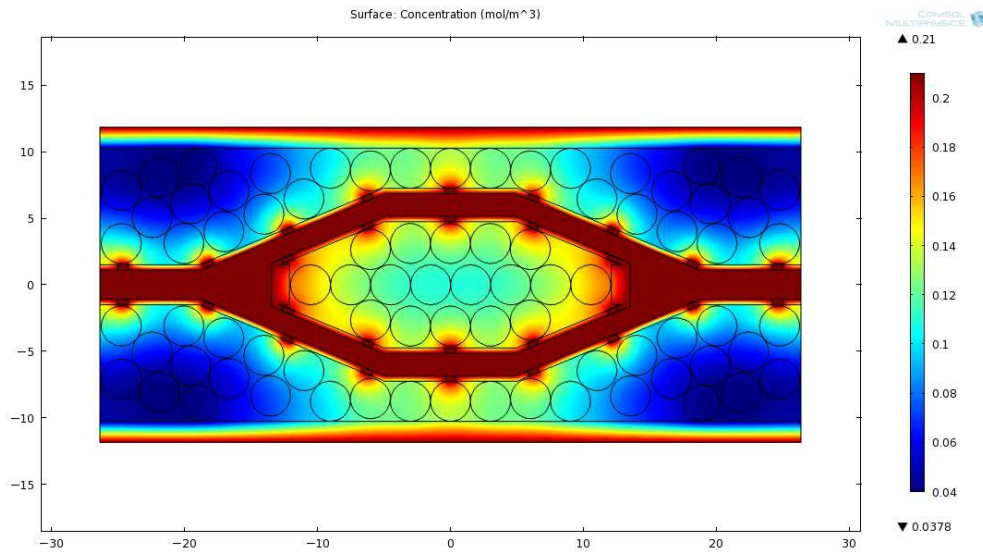


Figure 22: 6mm Pore Spacing Oxygen Concentration - Middle Branch, FEP

Figure 21 represents a 3 mm center-center pore spacing, while Figure 22 represents a 6 mm center-center spacing. Here, oxygen concentration in the 6 mm model falls below 4% in areas where the distance from each bead to the nearest pore is at a

maximum, whereas the 3 mm model maintains oxygen levels above 4% at all locations. Once again, top/bottom branch models can be found in Appendix E.

Finally, the effect of utilizing a single tube, once again representing that worst case TPS scenario, was examined. Here, Figure 23 represents a 1.5 mm pore spacing, and Figure 24 represents a 9 mm pore spacing. Figure 24 clearly demonstrates that a single tube with 9 mm pore spacing will not support cell viability. Interestingly, Figure 23 shows oxygen concentrations above 4% in nearly all regions. However, this can largely be attributed to Michaelis-Menten reaction kinetics, where metabolic activity is actually a function of oxygen concentration. Therefore, cells on the periphery of constructs would display lower metabolic rates, and thus differing differentiation and proliferation characteristics.

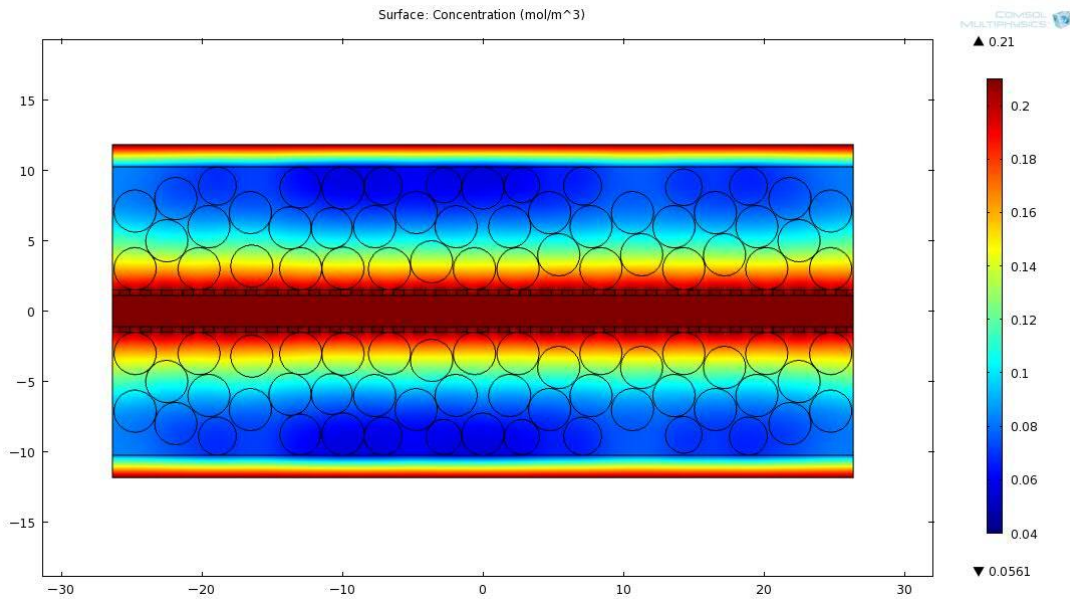


Figure 23: 1.5mm Pore Spacing Oxygen Concentration - Single Tube, FEP

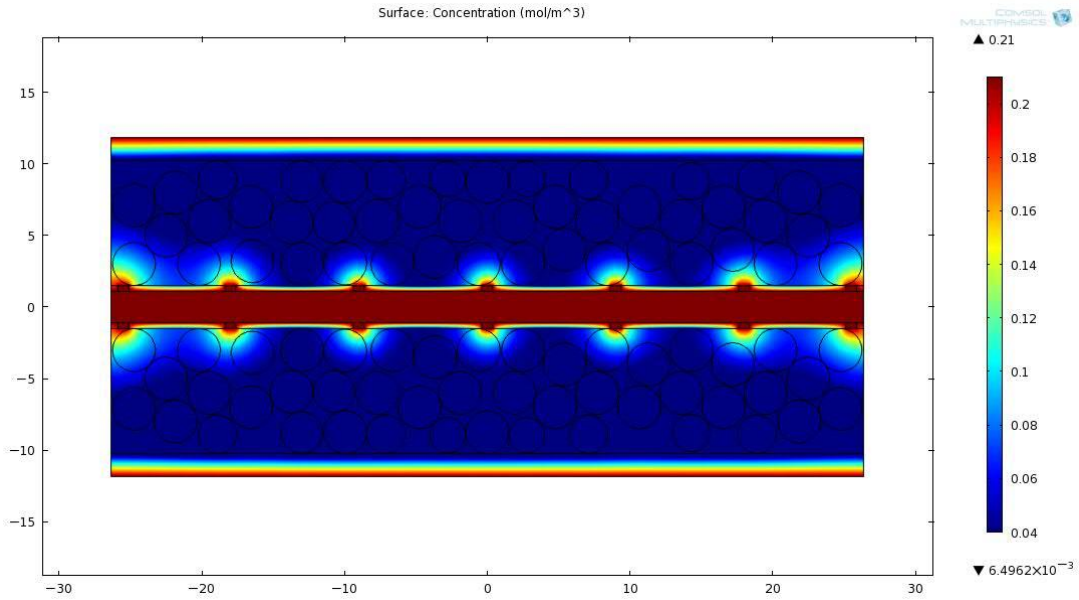


Figure 24: 1.5mm Pore Spacing Oxygen Concentration - Single Tube, FEP

SolidWorks CFD Analysis

CFD results from SolidWorks flow simulations demonstrate flow velocities similar to average velocities in previous TPS bioreactor experiments.²⁵ Furthermore, flow profiles for all three groups examined were relatively consistent, with similar velocities throughout the design, and a uniform distribution of flow throughout all branches.

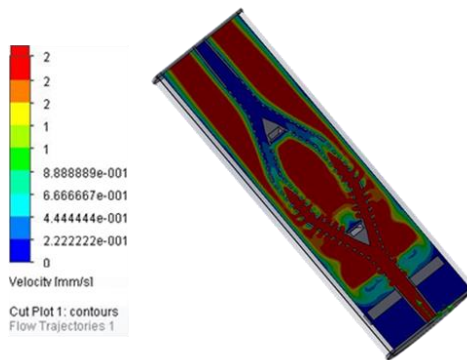


Figure 25: Full Network, 1.5mm Pore Spacing CFD Results

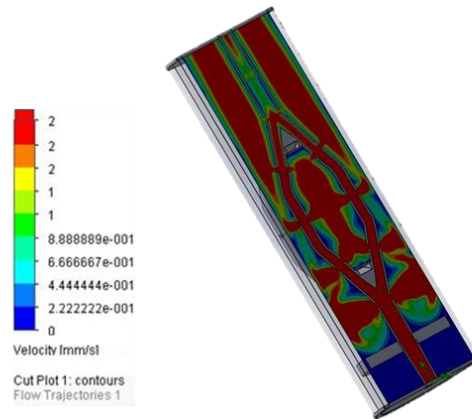


Figure 26: Full Network, 9mm Pore Spacing CFD Results

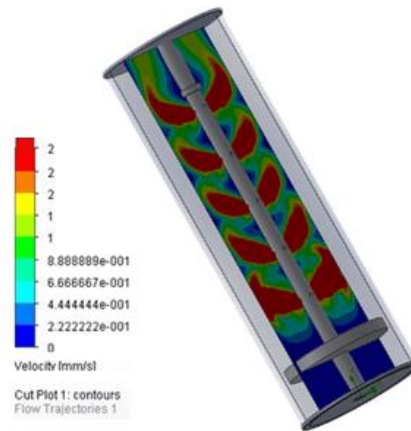


Figure 27: Single Tube, 9mm Pore Spacing CFD Results

More images of these flow simulations can be found in Appendix F.

Finally, CFD results validate the assumption of zero convection within fully aggregated constructs, as demonstrated in Figure 28 and Figure 29, where the entire flow profile is contained within the printed network.

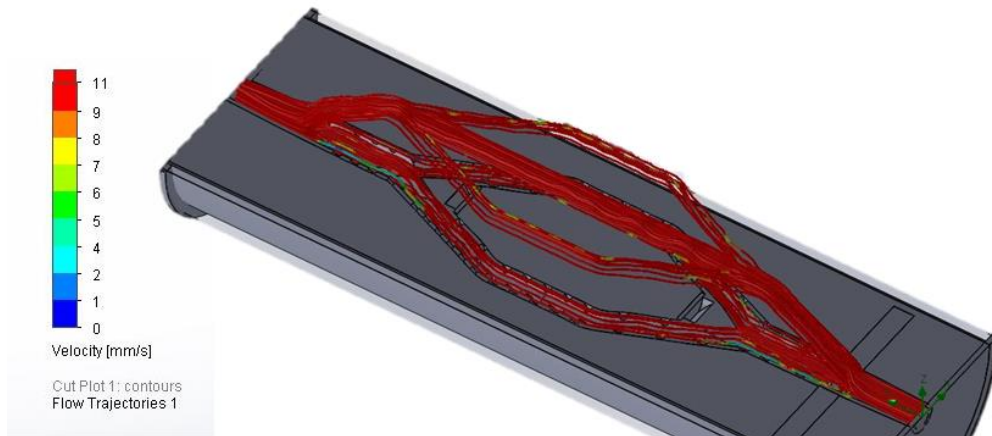


Figure 28: Flow Through an Aggregated Alginate Construct

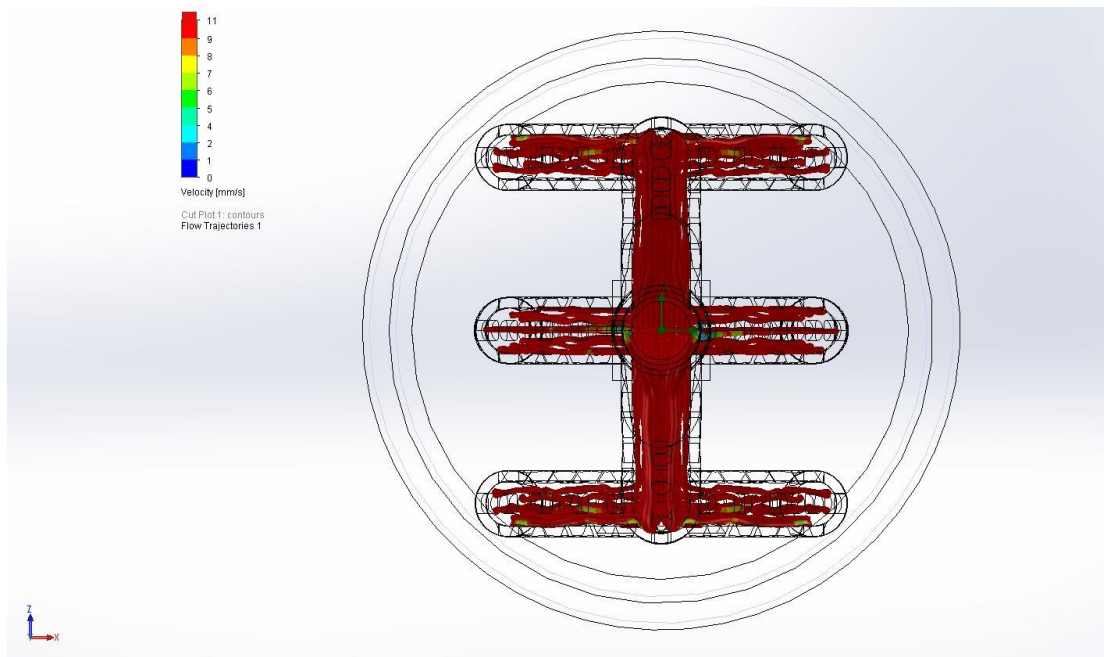


Figure 29: Containment of Flow Through an Aggregated Alginate Construct

***In Vitro* BTE Construct Viability**

BTE construct viability was further examined *in vitro* through the use of viability assays after 24 hours of pre-aggregation flow (Day 1), and after 24 hours of post-aggregation flow (Day 2). Over 1,000 live/dead viability images were taken and processed to obtain

percent live cell counts. The percentage of live cells in each experimental group were not statistically different at the Day 1 time point, as evidenced by Figure 31. Graphs for each individual group can be found in Appendix D.

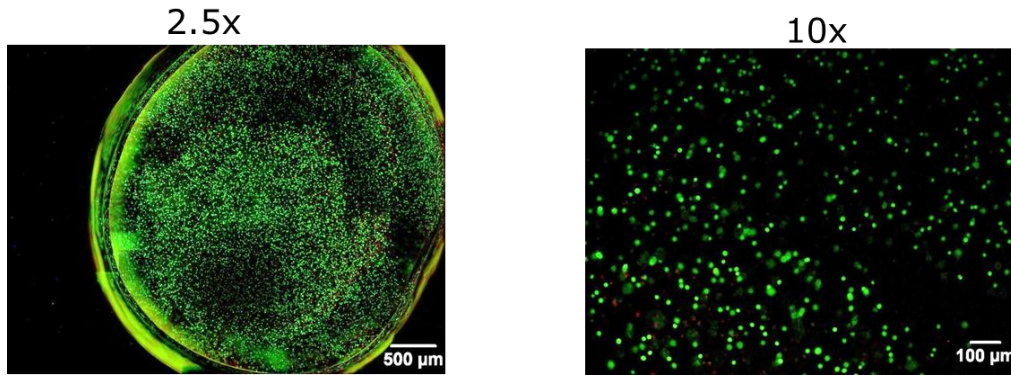


Figure 30: Day 1 Merged Live/Dead Images

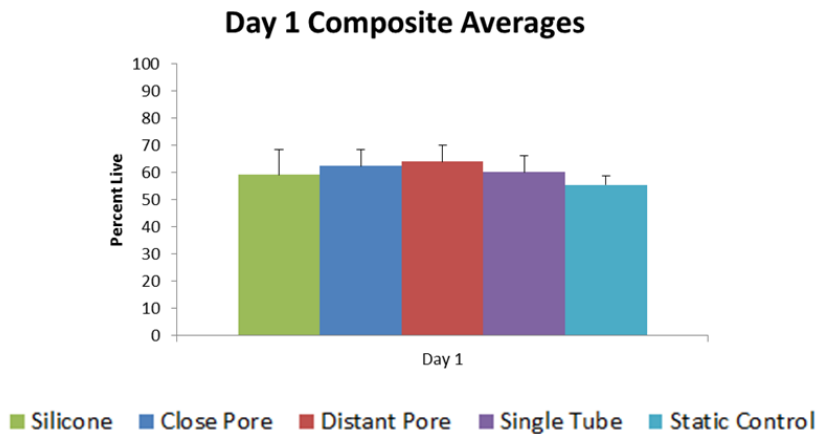


Figure 31: Day 1 Percent Live Composite Averages

Day 2 analyses displayed differing results, as expected. Figure 32 provides representative images of samples taken from the core of Static Control and Silicone experimental groups. These results are graphed in Figure 33, where groups that do not share a letter are statistically different.

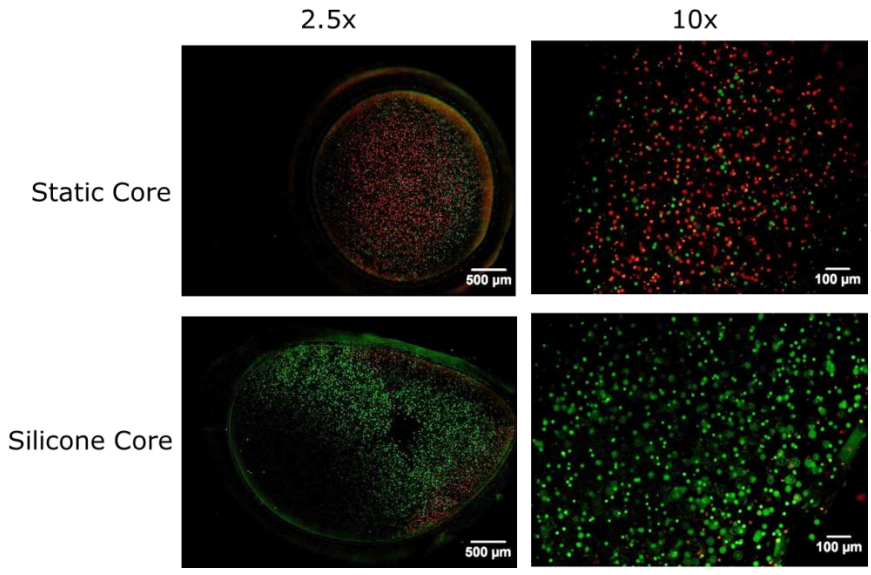


Figure 32: Viability in the Core of Static Control and Silicone Groups

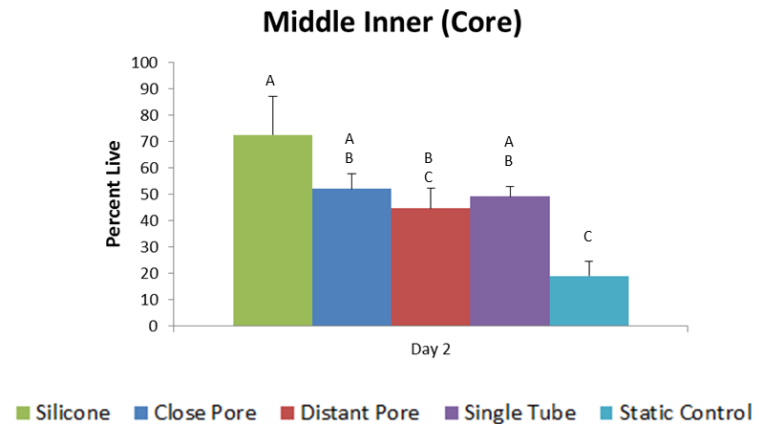


Figure 33: Graphical Representation of Core Viability

It is worth noting that every group, with the exception of the Distant Pore group, is statistically different from the Static Control, with the Silicone group achieving an average of more than three times the percentage of live cells in static groups.

Figure 34 is a graphical representation of the composite averages of each harvest site. Graphs of the percentage of live cells for each harvest site can be found in Appendix D, with raw data shown in Appendix A.

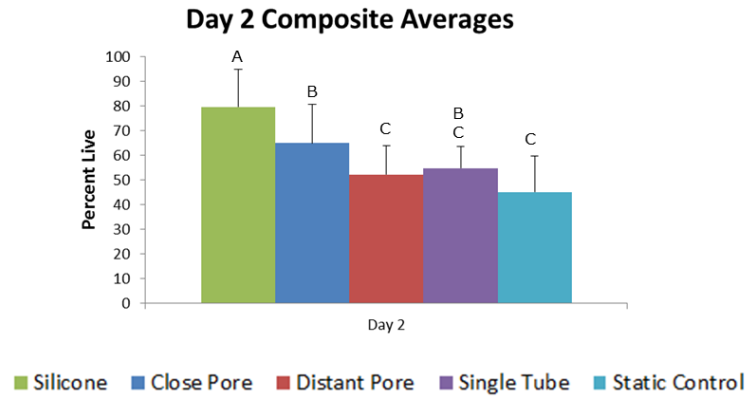


Figure 34: Day 2 Percent Live Composite Averages

Discussion

COMSOL Diffusion Studies

By comparing each COMSOL diffusion model against all others, it was observed that the use of platinum cured silicone tubing for the reaction chamber caused the diffusion of oxygen from the periphery to dominate the diffusion of oxygen from the networks. This resulted in all groups achieving oxygen levels above the chosen floor of 4%. For this reason, FEP tubing was utilized to mimic an *in vivo* environment. Here, was hypothesis was that an increasing porosity, driven by a decreasing center-center pore distance, along with a decreasing distance from each bead to the nearest pore, as driven by the presence of a branching network, will increase oxygen levels throughout the scaffold. This hypothesis was validated through the many COMSOL studies. Further, it was shown that while a 1.5 mm pore spacing will achieve O₂ levels above 4%, a 3 mm pore spacing will also achieve this same result. However, at a spacing of 6 mm O₂ levels begin to fall below 4%, and at a spacing of 9 mm, a significant portion of the construct nears 0%. In single tube networks with pore spacings of 9 mm, the entire construct fell well below 4% O₂.

Finally, it was shown that while a single tube with pores every 1.5 mm results in O₂ levels above 4% throughout the construct, this architecture results in significant gradients, where O₂ levels drop as radial distance from the centerline increases. Due to the dependence of proliferation and differentiation on O₂ concentration, this architecture would result in non-uniform differentiation, and likely non-functionality of the construct. Therefore, the developed construct must make an effort to equalize the distance of each bead to its nearest pore, a challenge which is best met through the use of a symmetric, branched network.

SolidWorks CFD Analysis

CFD analysis of three separate SolidWorks designs (branched network with 1.5 mm pore spacing, branched network with 9 mm pore spacing, and single tube with 9 mm pore spacing) demonstrated similar flow profiles and velocities in all three groups. Furthermore, these velocities were on par with those shown to increase differentiation due to the application of shear stress in previous TPS experiments.²⁵ It was hypothesized that perfusion network design will have little effect on the pre-aggregation viability of cells encapsulated within alginate beads, provided that each bead sees some degree of convection. The CFD simulations demonstrated an expected similarity of pre-aggregation flow, allowing for *in vitro* experiments to test this hypothesis.

At the same time, CFD analysis of flow in an aggregated construct resulted in zero flow perfusing into the alginate, confirming results obtained from Darcy's Law calculations. In *in vitro* experiments, small amounts of convection actually occurred throughout the constructs due to imperfect aggregation. It is hypothesized that this

extra post-aggregation convection attributed to elevated cell viability in Single Tube and Distant Pore groups.

***In Vitro* Viability Analyses**

The *in vitro* analysis of hMSCs in our modified TPS bioreactor allowed for the testing of the overarching, two-part hypothesis. This hypothesis was that perfusion network design will have little effect on the pre-aggregation viability of cells encapsulated within alginate beads, provided that each bead sees some degree of convection, while post-aggregation viability will be a function of oxygen concentration throughout the construct, and therefore porosity and distance of each bead from the nearest pore.

Day 1 viability analyses at each harvest site yielded data that validated the first part of this hypothesis. In fact, Day 1 composite averages across all sites yielded no statistically different results. It should be noted here that Day 1 viability was roughly 60% across all groups. This viability was lower than expected, and can be attributed to the extended time that each harvested bead spent without nutrients before it was imaged. Normally, aggregation of each group would take less than 25 minutes, and with the alginate gels trapping many nutrients, cells would not experience a lack of nutrients during this time. However, due to the requirement to harvest beads from six sites from each of 4 groups, along with the need to aggregate and re-perfuse each construct, harvested beads sat without media for a period of about several hours. It is worth noting that care was preferentially given to beads within the constructs that would be re-perfused and examined at Day 2, as these results form the core of the

novelty of this research. Further, though harvested beads were removed from media for a significant period of time, this time was the same across all groups.

While important, pre-aggregation viability and flow profiles can actually be circumvented by simply running the bioreactor without the printed network, as has been proven to work in the past. Then, once cells within the beads begin to differentiate and calcify, they can be removed from the pre-aggregation chamber, and aggregated around a printed network for re-perfusion as was done here. However, it was necessary to examine the pre-aggregation viability of a network-containing bioreactor in order to accurately determine the causes of viability trends. Additionally, if pre-aggregation differentiation and mineralization in a network-containing bioreactor are comparable to those without, much time and effort can be saved by simply utilizing a network from the beginning stages.

It is also worth noting that while FEP tubing provided a significant barrier to O₂ diffusion, it was very rigid and thus very hard to work with. Because of the stiffness of the tubing, significant force had to be applied to achieve a tight seal around the connectors. In fact, a silicone sealant and sealing tape had to be used to prevent leakage and the formation of air bubbles due to the presence of micro-cracks at the tubing-connector interface. For this reason, FEP tubing is not recommended, unless absolutely necessary, as it was here. These issues were not present in the Silicone group. The application of force necessary to achieve a tight seal caused the Single Tube design to snap in half. On top of its frailty, the Single Tube group failed to adequately bond with the aggregated construct, as shown in Figure 35, demonstrating the need for a box-like structure to maintain construct integrity. This

can be attributed to the hydrophilic nature of the alginate, as opposed to the hydrophobic nature of the EShell. The frailty and lack of construct integrity of the single tube design are just two more reason why a more robust structure is needed.

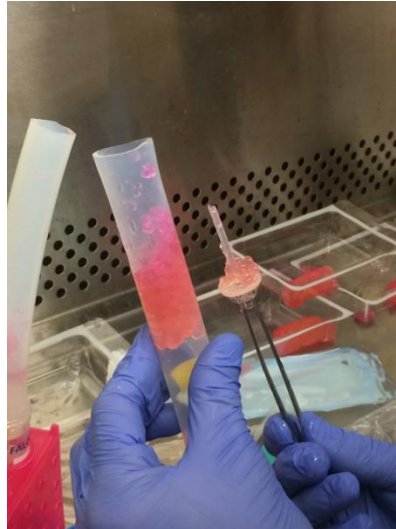


Figure 35: Failure of Single Tube to Adequately Bond with Construct

On the other hand, full, branched network designs allowed for the formation of tight cylindrical constructs, with a single inlet and outlet that would allow for direct anastomosis to existing host vasculature, as shown in Figure 36.



Figure 36: Aggregated Construct Demonstrates Possibility of Direct Anastomosis

Day 2 viability results displayed a clear trend of decreasing viability with decreasing porosity, as evidenced by the Day 2 composite averages represented in Figure 37. In this figure, the COMSOL oxygen concentrations can be found directly above the corresponding *in vitro* results for each group. This trend validates the second part of the hypothesis that oxygen concentrations would decrease with decreasing porosity, and therefore a decrease in porosity would cause a decrease in viability. It is hypothesized that the Single Tube viability was unusually high because the tube snapped in half upon reattachment of the connectors post-aggregation. In order to connect this tubing to the outlet connector, construct height was also cut in half, resulting in a much lower diffusion distance than in other groups, as the top surface was exposed directly to media.

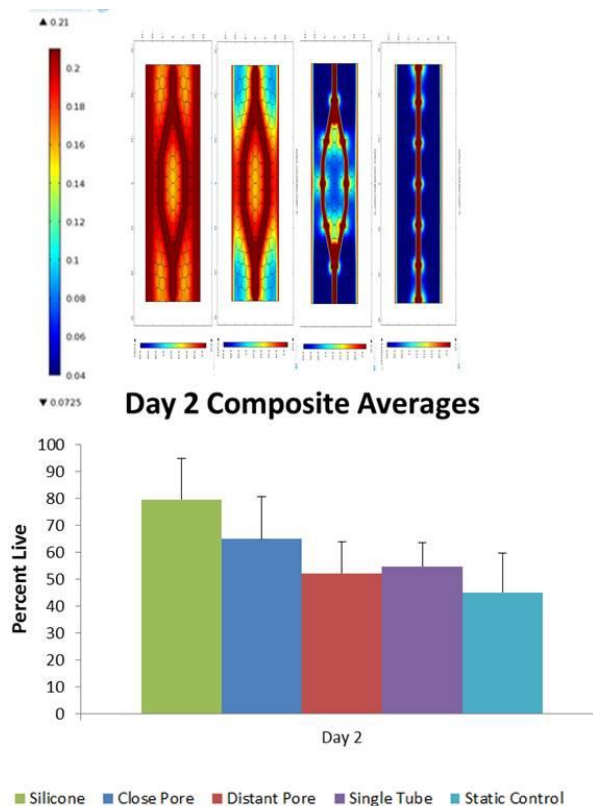


Figure 37: Composite Averages and Corresponding COMSOL Expectations

Perhaps the most important Day 2 results are obtained from the Middle Inner (core) harvest sites (Figure 33, page 59). Here, the need for inherent vasculature is painfully obvious, with only about 20% of Static Control cells still living after just 24 hours. At this harvest site, all groups were statistically different except for the Distant Pore group, but even that group had a mean percent live count of nearly double that in the Static Control.

On the subject of the Static Control group, it is worth noting that it is not surprising that the percentage of live cells was often higher than in the Distant Pore and Single Tube groups at all harvest sites except for the core. This is because in the Static Control group, all harvest sites except for the middle inner site were directly on the periphery of the construct, and thus directly exposed to static media. On the other hand, the outer harvest sites in the bioreactor groups were adjacent to the tubing wall, and thus saw little direct exposure to media. It is for this reason that the Static Core viability is as high as it is in the composite average, and the Middle Inner results are so important. Further, as overall construct size increases, the surface area to volume ratio will decrease. Therefore, a larger percentage of cells will be contained in the core than on the periphery. Similarly, as construct size increases, the time required for complete host-invasion vascularization increases, resulting in long term hypoxic conditions in the core region. Therefore, while the composite average is necessary to demonstrate cell viability at all construct locations, the Middle Inner, or core, harvest site is perhaps the most important, and contains the largest percentage of cells when dealing with large constructs.

As for the viability in the Single Tube and Distant Pore groups, it is hypothesized that imperfect aggregation led to higher viability levels than expected from the COMSOL modeling, as some degree of convective flow was observed throughout these constructs.

Future Directions

The end goal of this work is to develop the capability to both create and replicate large scale bone tissue engineered constructs, complete with inherent vasculature ready for direct anastomosis to host vascular networks. While this work focuses primarily on TPS bioreactors, the application of the network design is not limited to this family of bioreactors. At its most base element, the designed network is simply a CAD file. How this file is utilized is completely determined by the researcher. Here, it was used to create a rigid structure that directly composes the vascular network for us in a TPS bioreactor. Similarly, constructs could be molded around this network to create structures more commonly used in direct perfusion, or even spinner or rotating wall bioreactors. Alternatively, the mold structure used in the CFD modeling could be printed, and used to cast a sacrificial vascular network, or the network could be directly printed with a sacrificial material. The potential for use in both of these methods of creating sacrificial vascular networks greatly increases the number of material types and fabrication techniques available to the researcher. The outer geometries of scaffolds created around this network could be tailored to fit any bioreactor type, and could be combined with other vascularization methods, such as particulate leaching, to achieve a system complete with both a direct vascular axis and a high degree of porosity to encourage vascular ingrowth and cell migration.

The next logical step in the progression of this work is to replace the bioinert, non-degrading EShell material with a non-cytotoxic biomaterial which will degrade over time, to be gradually replaced with host vasculature. Further, a co-culture of hMSCs with endothelial cells could allow for the creation of a confluent monolayer of endothelial cells on the inner surface of the printed network. Ideally, this monolayer of cells would then branch out of the network, via the network pores, allowing for vascularization of the construct not only from the outside-in via spontaneous host-capillary invasion, but also from the inside out. This would dramatically decrease the time necessary for complete construct vascularization.

Conclusion

With over 185,000 limb amputations in the United States alone,² and approximately 15 million bone fractures worldwide every year,¹ there is a large clinical need for bone tissue engineering alternatives. At present, approximately 1 million grafting procedures are performed each year.⁶⁴ Risk factors for bone injury include physical activity, obesity, and aging,¹ meaning that nearly the entire population is at risk. While grafting procedures and surgical techniques help to heal bone defects, they leave many undesirable effects including infection, graft rejection, donor site morbidity, and extended healing times. Current research is limited by the lack of vascularized bone constructs.

This research provides a novel and promising approach to the vascularization of bone tissue engineered constructs. Here, stereolithographic printing is combined with both *in silico* modeling and *in vitro* testing to design and validate a biomimetic vascular architecture for use in TPS bioreactors. Under this system, cells can

experience the advantageous pre-aggregation flow and accompanying shear stress to preferentially differentiate down osteogenic pathways. Post aggregation, any number of these constructs could be combined either in series or in parallel, or both, to allow for the complete vascularization of even the largest of constructs.

The first goal of this study was to examine the relationship between network porosity and oxygen concentration in an aggregated alginate construct within a tubular perfusion system bioreactor. This analysis was completed using COMSOL Multiphysics software, and resulted in a determination of a maximum center to center pore spacing of 3 mm. This spacing allows for the maintenance of at least 4% oxygen throughout a construct that utilizes the designed perfusion network, complete with 750 μm diameter pores and air-saturated perfusion media.

After determining the range of pore spacing which would result in relevant levels of oxygen throughout a construct, CAD network files were examined using computational fluid dynamics, via SolidWorks' Flow Simulation package. It was determined that for the three tested designs, pre-aggregation flow was similar enough to expect the similar percentages of live cells in all constructs. Similarly, a uniform flow distribution was observed in all branches of the branched network designs. Further, the assumption that convection could be neglected in COMSOL simulations was validated.

Finally, *in silico* modeling results from COMSOL and SolidWorks were examined *in vitro* by running a 48 hour bioreactor experiment complete with 400,000,000 human bone-marrow derived mesenchymal stem cells and 5 experimental groups. By performing viability assays after 24 hours of pre-aggregation

perfusion and again after 24 hours of post-aggregation perfusion, results were obtained that validated the *in silico* modeling. In short, Day 1 viability was not statistically different across all groups, while Day 2 viability displayed a trend of decreasing viability with decreasing network porosity. Furthermore, the potential efficacy of TPS bioreactor bone tissue engineered constructs as implants that can be utilized for direct anastomosis was demonstrated by perfusing fully aggregated constructs for the first time.

The vascular network designed and printed here shows promise not only for use in TPS bioreactors, but also many other dynamic culture strategies. By combining this architecture with a biodegradable network material and a lining of endothelial cells, it may be possible to create a vascular network that provides for the extended growth and viability of hMSCs throughout an entire large scale construct. Further, the incorporation of large-diameter inlet and outlet channels allows for the potential direct anastomosis of these constructs to existing host vasculature. In conjunction with this, the major vascular axis featured in these constructs will allow for immediate perfusion upon implantation, while the network of pores will sustain cell life until the network can be fully integrated with the body via spontaneous host vascular ingrowth.

In summary, a thorough combination of computer-aided design, *in silico* modeling, and *in vitro* experiments resulted in the development of a 3D printed network which provided adequate levels of oxygen throughout a BTE construct of more than 20 cm³, or twice the size of any current BTE constructs,¹⁴ to support the viability of human mesenchymal stem cells. Analysis of these results determined that

the overall hypothesis was validated by demonstrating that perfusion network design had no significant effect on the pre-aggregation viability of cells encapsulated within alginate beads, while post-aggregation viability was a function of oxygen concentration throughout the construct, and therefore porosity and distance of each bead from the nearest pore.

Appendix A: Raw Data

Table 1: 2% Alginate Bead Diameters in 0.1M CaCl₂

Bead Diameter (μm)	3666.9	3313.8	3777.7	3847.7	3897.3	3675.2	3266.5	3042	3653.4	3335.6
Average (μm)	3547.61									
Standard Deviation (μm)	286.9879999									

Table 2: Percent Live Values for Each Bead

	Day 1 Percent Live					Day 2 Percent Live				
	1.5	9	Silicone	Single Tube	Static	1.5	9	Silicone	Single Tube	Static
BI	72.52475	77.57009	62.1832	68.8109162	59.40054	95.18519	49.2569	92.4324	48.8372093	59.681
BI	57.44681	62.62425	53.7676	68.3333333	55.53236	38.07615	48.44961	73.3333	37.6237624	61.159
BI	61.25828	54.46009	49.483	70.4787234	51.60698	81.6092	24.24242	89.8039	50.9090909	60.44
BO	60.16129	63.37209	51.6505	54.6263345	59.40054	75.07692	29.03226	95.5947	55.8441558	59.681
BO	56.05634	62.88462	60.7011	52.5490196	55.53236	51.8797	63.3452	81.8182	49.3023256	61.159
BO	61.82432	54.58824	63.048	63.8461538	51.60698	77.63713	45.77465	87.4564	58.7044534	60.44
MI	53.15712	63.97059	56.7134	53.1190926	59.40054	58.90411	55.52239	63.3094	54.6031746	26.253
MI	74.34343	68.38906	51.6068	49.1452991	55.53236	44.44444	38.19876	61.2821	45.8715596	13.147
MI	67.85714	74.28571	53.1183	66.4359862	51.60698	52.68595	40.37736	93.0233	47.113164	17.722
MO	56.82327	65.98361	60.5735	63.5775862	59.40054	59.8916	40.79755	78.0992	69.3617021	47.667
MO	63.46749	67.41855	53.4527	60.6648199	55.53236	63.61111	37.96791	53.2847	61.8473896	47.2
MO	55.00795	62.00528	61.7834	61.8042226	51.60698	54.57875	48.03738	73.741	60.4	48.477
TI	60.16129	58.62069	62.5995	60.4712042	59.40054	61.43791	81.14754	83.913	65.3333333	45.32
TI	64.77495	64.48598	57.8415	55.5555556	55.53236	68.04979	75.15152	79.5082	42.9577465	44.717
TI	57.41127	59.49367	60	61.4583333	51.60698	55.25	72.43243	80.9756	58.685446	35.101
TO	70.62937	58.85167	64.139	60.6924644	59.40054	85.12397	64.72603	93.8462	71.1409396	45.32
TO	69.1974	71.18644	92.7481	56.5701559	55.53236	58.867	61.58192	76.9968	50.6711409	44.717
TO	61.82171	62.87215	50.9677	55.2425665	51.60698	88.75969	64.59627	74.6212	58.2089552	35.101
Average	62.44023	64.05904	59.2432	60.187876	55.51329	65.05937	52.25767	79.6133	54.8564194	45.183
Std Dev	6.093915	5.966433	9.3718	5.94184454	3.181739	15.30675	15.59194	11.5368	8.77532198	14.453

Table 3: Bottom Inner Day 1 Raw Data

Bottom Inner Day 1									
1.5									
Slice	Count	Total Area	Average Size	%Area	Mean	Total Cells	% Live	AVG % Live	STD DEV
10x2 Dead1.jpg	111	16021	144.333	0.834	255	404	72.524752	63.74327971	6.401433336
10x2 Live1.jpg	293	47106	160.771	2.453	255				
10x3 Dead1.jpg	420	72694	173.081	3.786	255	987	57.446809		
10x3 Live1.jpg	567	98533	173.78	5.132	255				
10x4 Dead1.jpg	234	31796	135.88	1.656	255	604	61.258278		
10x4 Live1.jpg	370	64213	173.549	3.344	255				

9									
Slice	Count	Total Area	Average Size	%Area	Mean	Total Cells	% Live	AVG % Live	STD DEV
10x1 Dead1.jpg	96	15636	162.875	0.814	255	428	77.570093	64.88481394	9.569068808
10x1 Live1.jpg	332	58160	175.181	3.029	255				
10x2 Dead1.jpg	188	31415	167.101	1.636	255	503	62.624254		
10x2 Live1.jpg	315	52132	165.498	2.715	255				
10x4 Dead1.jpg	291	40478	139.1	2.108	255	639	54.460094		
10x4 Live1.jpg	348	60088	172.667	3.13	255				

Silicone									
Slice	Count	Total Area	Average Size	%Area	Mean	Total Cells	% Live	AVG % Live	STD DEV
10x1 Dead1.jpg	194	34799	179.376	1.812	255	513	62.183236	55.14460328	5.275484061
10x1 Live1.jpg	319	52741	165.332	2.747	255				
10x2 Dead1.jpg	362	63204	174.597	3.292	255	783	53.767561		
10x2 Live1.jpg	421	79778	189.496	4.155	255				
10x3 Dead1.jpg	342	67969	198.74	3.54	255	677	49.483013		
10x3 Live1.jpg	335	77140	230.269	4.018	255				

Single Tube									
Slice	Count	Total Area	Average Size	%Area	Mean	Total Cells	% Live	AVG % Live	STD DEV
10x1 Dead1.jpg	160	22606	141.288	1.177	255	513	68.810916	69.20765764	0.919683815
10x1 Live1.jpg	353	66461	188.275	3.462	255				
10x3 Dead1.jpg	133	19853	149.271	1.034	255	420	68.333333		
10x3 Live1.jpg	287	59487	207.272	3.098	255				
10x4 Dead1.jpg	111	18448	166.198	0.961	255	376	70.478723		
10x4 Live1.jpg	265	51976	196.136	2.707	255				

Static									
Slice	Count	Total Area	Average Size	%Area	Mean	Total Cells	% Live	AVG % Live	STD DEV
10x2 Dead1.jpg	298	33807	113.446	1.761	255	734	59.400545	55.51329431	3.181738587
10x2 Live1.jpg	436	58852	134.982	3.065	255				
10x3 Dead1.jpg	213	27360	128.451	1.425	255	479	55.532359		
10x3 Live1.jpg	266	39478	148.414	2.056	255				
10x4 Dead1.jpg	527	86344	163.841	4.497	255	1089	51.606979		
10x4 Live1.jpg	562	98644	175.523	5.138	255				

Table 4: Bottom Inner Day 2 Raw Data

Bottom Inner Day 2									
1.5									
Slice	Count	Total Area	Average Size	%Area	Mean	Total Cells	% Live	AVG % Live	STD DEV
10x1 Dead1.jpg	13	1455	111.923	0.076	255	270	95.18519	71.62351096	24.36043006
10x1 Live1.jpg	257	53763	209.195	2.8	255	499	38.07615		
10x2 Dead1.jpg	309	62886	203.515	3.275	255				
10x2 Live1.jpg	190	36233	190.7	1.887	255	261	81.6092		
10x3 Dead1.jpg	48	8213	171.104	0.428	255				
10x3 Live1.jpg	213	46801	219.723	2.438	255				

9									
Slice	Count	Total Area	Average Size	%Area	Mean	Total Cells	% Live	AVG % Live	STD DEV
10x1 Dead1.jpg	239	57393	240.138	2.989	255	471	49.2569	40.64964562	11.60633773
10x1 Live1.jpg	232	45931	197.978	2.392	255	258	48.44961		
10x2 Dead1.jpg	133	17043	200.506	0.888	255			231	24.24242
10x2 Live1.jpg	125	23721	199.336	1.235	255				
10x3 Dead1.jpg	175	27343	156.246	1.424	255				
10x3 Live1.jpg	56	7513	134.161	0.391	255				

Silicone									
Slice	Count	Total Area	Average Size	%Area	Mean	Total Cells	% Live	AVG % Live	STD DEV
10x1 Dead1.jpg	14	2916	208.286	0.152	255	185	92.43243	85.18989578	8.452251065
10x1 Live1.jpg	171	31672	185.216	1.65	255	180	73.33333		
10x3 Dead1.jpg	48	6049	126.021	0.315	255			255	89.80392
10x3 Live1.jpg	132	25565	193.674	1.332	255				
10x4 Dead1.jpg	26	2386	91.769	0.124	255				
10x4 Live1.jpg	229	48098	210.035	2.505	255				

Single Tube									
Slice	Count	Total Area	Average Size	%Area	Mean	Total Cells	% Live	AVG % Live	STD DEV
10x1 Dead1.jpg	220	32950	149.773	1.716	255	430	48.83721	45.79002086	5.836037845
10x1 Live1.jpg	210	47836	227.79	2.491	255	101	37.62376		
10x3 Dead1.jpg	63	7154	113.556	0.373	255			165	50.90909
10x3 Live1.jpg	38	10825	284.868	0.564	255				
10x4 Dead1.jpg	81	17525	216.358	0.913	255				
10x4 Live1.jpg	84	12600	150	0.656	255				

Static									
Slice	Count	Total Area	Average Size	%Area	Mean	Total Cells	% Live	AVG % Live	STD DEV
10x1 Dead1.jpg	202	42074	208.287	2.191	255	501	59.68064	60.42653982	0.603780249
10x1 Live1.jpg	299	58943	197.134	3.07	255	345	61.15942		
10x2 Dead1.jpg	134	27829	207.679	1.449	255			273	60.43956
10x2 Live1.jpg	211	32173	152.479	1.676	255				
10x4 Dead1.jpg	108	19729	182.676	1.028	255				
10x4 Live1.jpg	165	28388	172.048	1.479	255				

Table 5: Bottom Outer Day 1 Raw Data

Bottom Outer Day 1									
1.5									
Slice	Count	Total Area	Average Size	%Area	Mean	Total Cells	% Live	AVG % Live	STD DEV
10x1 Dead1.jpg	247	42336	171.401	2.205	255	620	60.16129032	59.34731756	2.424091613
10x1 Live1.jpg	373	68290	183.083	3.557	255				
10x3 Dead1.jpg	312	63062	202.122	3.284	255	710	56.05633803		
10x3 Live1.jpg	398	73376	184.362	3.822	255				
10x4 Dead1.jpg	226	35807	158.438	1.865	255	592	61.82432432		
10x4 Live1.jpg	366	63255	172.828	3.295	255				

9									
Slice	Count	Total Area	Average Size	%Area	Mean	Total Cells	% Live	AVG % Live	STD DEV
10x2 Dead1.jpg	252	33217	131.813	1.73	255	688	63.37209302	60.2816479	4.030766589
10x2 Live1.jpg	436	74176	170.128	3.863	255				
10x3 Dead1.jpg	193	26654	138.104	1.388	255	520	62.88461538		
10x3 Live1.jpg	327	52260	159.817	2.722	255				
10x4 Dead1.jpg	193	22776	118.01	1.186	255	425	54.58823529		
10x4 Live1.jpg	232	38789	167.194	2.02	255				

Silicone									
Slice	Count	Total Area	Average Size	%Area	Mean	Total Cells	% Live	AVG % Live	STD DEV
10x1 Dead1.jpg	249	53213	213.707	2.772	255	515	51.65048544	58.46653638	4.913987461
10x1 Live1.jpg	266	53277	200.289	2.775	255				
10x3 Dead1.jpg	213	27361	128.455	1.425	255	542	60.70110701		
10x3 Live1.jpg	329	57366	174.365	2.988	255				
10x4 Dead1.jpg	177	23163	130.864	1.206	255	479	63.0480167		
10x4 Live1.jpg	302	52882	175.106	2.754	255				

Single Tube									
Slice	Count	Total Area	Average Size	%Area	Mean	Total Cells	% Live	AVG % Live	STD DEV
10x2 Dead1.jpg	255	47803	187.463	2.49	255	562	54.62633452	57.00716932	4.909690505
10x2 Live1.jpg	307	57713	187.99	3.006	255				
10x3 Dead1.jpg	242	46763	193.236	2.436	255	510	52.54901961		
10x3 Live1.jpg	268	53494	199.604	2.786	255				
10x4 Dead1.jpg	141	24620	174.61	1.282	255	390	63.84615385		
10x4 Live1.jpg	249	44509	178.751	2.318	255				

Static									
Slice	Count	Total Area	Average Size	%Area	Mean	Total Cells	% Live	AVG % Live	STD DEV
10x2 Dead1.jpg	298	33807	113.446	1.761	255	734	59.40054496	55.51329431	3.181738587
10x2 Live1.jpg	436	58852	134.982	3.065	255				
10x3 Dead1.jpg	213	27360	128.451	1.425	255	479	55.53235908		
10x3 Live1.jpg	266	39478	148.414	2.056	255				
10x4 Dead1.jpg	527	86344	163.841	4.497	255	1089	51.60697888		
10x4 Live1.jpg	562	98644	175.523	5.138	255				

Table 6: Bottom Outer Day 2 Raw Data

Bottom Outer Day 2									
1.5									
Slice	Count	Total Area	Average Size	%Area	Mean	Total Cells	% Live	AVG % Live	STD DEV
10x1 Dead1.jpg	81	19223	160.192	1.001	255	325	75.07692308	68.19791771	11.58596439
10x1 Live1.jpg	244	25749	130.045	1.341	255				
10x2 Dead1.jpg	128	23697	185.133	1.234	255	266	51.87969925		
10x2 Live1.jpg	138	27282	197.696	1.421	255				
10x3 Dead1.jpg	53	5646	106.528	0.294	255	237	77.6371308		
10x3 Live1.jpg	184	29411	159.842	1.532	255				
9									
Slice	Count	Total Area	Average Size	%Area	Mean	Total Cells	% Live	AVG % Live	STD DEV
10x1 Dead1.jpg	110	21074	191.582	1.098	255	155	29.03225806	46.05070056	14.00955809
10x1 Live1.jpg	45	5521	122.689	0.288	255				
10x2 Dead1.jpg	103	16713	162.262	0.87	255	281	63.34519573		
10x2 Live1.jpg	178	40921	229.893	2.131	255				
10x4 Dead1.jpg	77	15642	203.143	0.815	255	142	45.77464789		
10x4 Live1.jpg	65	12062	185.569	0.628	255				
Silicone									
Slice	Count	Total Area	Average Size	%Area	Mean	Total Cells	% Live	AVG % Live	STD DEV
10x1 Dead1.jpg	10	1147	114.7	0.06	255	227	95.59471366	88.28978049	5.655029747
10x1 Live1.jpg	217	41690	192.12	2.171	255				
10x2 Dead1.jpg	36	5605	155.694	0.292	255	198	81.81818182		
10x2 Live1.jpg	162	31627	195.228	1.647	255				
10x4 Dead1.jpg	36	3951	109.75	0.206	255	287	87.45644599		
10x4 Live1.jpg	251	62196	247.793	3.239	255				
Single Tube									
Slice	Count	Total Area	Average Size	%Area	Mean	Total Cells	% Live	AVG % Live	STD DEV
10x1 Dead1.jpg	102	21523	211.01	1.121	255	231	55.84415584	54.61697829	3.935265822
10x1 Live1.jpg	129	26061	202.023	1.357	255				
10x3 Dead1.jpg	109	19412	178.092	1.011	255	215	49.30232558		
10x3 Live1.jpg	106	21180	199.811	1.103	255				
10x4 Dead1.jpg	102	15473	151.696	0.806	255	247	58.70445344		
10x4 Live1.jpg	145	31227	215.359	1.626	255				
Static									
Slice	Count	Total Area	Average Size	%Area	Mean	Total Cells	% Live	AVG % Live	STD DEV
10x1 Dead1.jpg	202	42074	208.287	2.191	255	501	59.68063872	60.42653982	0.603780249
10x1 Live1.jpg	299	58943	197.134	3.07	255				
10x2 Dead1.jpg	134	27829	207.679	1.449	255	345	61.15942029		
10x2 Live1.jpg	211	32173	152.479	1.676	255				
10x4 Dead1.jpg	108	19729	182.676	1.028	255	273	60.43956044		
10x4 Live1.jpg	165	28388	172.048	1.479	255				

Table 7: Middle Inner Day 1 Raw Data

Middle Inner Day 1									
1.5									
Slice	Count	Total Area	Average Size	%Area	Mean	Total Cells	% Live	AVG % Live	STD DEV
10x1 Dead1.jpg	319	50909	159.589	2.652	255	681	53.15712188	65.11923303	8.863297792
10x1 Live1.jpg	362	53111	146.715	2.766	255				
10x3 Dead1.jpg	127	13423	105.693	0.699	255	495	74.34343434		
10x3 Live1.jpg	368	59762	162.397	3.113	255				
10x4 Dead1.jpg	81	11109	137.148	0.579	255	252	67.85714286		
10x4 Live1.jpg	171	31024	181.427	1.616	255				

9									
Slice	Count	Total Area	Average Size	%Area	Mean	Total Cells	% Live	AVG % Live	STD DEV
10x1 Dead1.jpg	196	27580	140.714	1.436	255	544	63.97058824	68.88178676	4.225521093
10x1 Live1.jpg	348	64574	185.557	3.363	255				
10x2 Dead1.jpg	208	25824	124.154	1.345	255	658	68.38905775		
10x2 Live1.jpg	450	85776	190.613	4.468	255				
10x3 Dead1.jpg	108	13443	124.472	0.7	255	420	74.28571429		
10x3 Live1.jpg	312	58551	187.663	3.05	255				

Silicone									
Slice	Count	Total Area	Average Size	%Area	Mean	Total Cells	% Live	AVG % Live	STD DEV
10x1 Dead1.jpg	216	38881	180.005	2.025	255	499	56.71342685	53.81283724	2.141837795
10x1 Live1.jpg	283	58798	207.767	3.062	255				
10x3 Dead1.jpg	256	48530	189.57	2.528	255	529	51.60680529		
10x3 Live1.jpg	273	57956	212.293	3.019	255				
10x4 Dead1.jpg	218	45860	210.367	2.389	255	465	53.11827957		
10x4 Live1.jpg	247	49572	200.696	2.582	255				

Single Tube									
Slice	Count	Total Area	Average Size	%Area	Mean	Total Cells	% Live	AVG % Live	STD DEV
10x2 Dead1.jpg	248	40930	165.04	2.132	255	529	53.11909263	56.23345931	7.394431429
10x2 Live1.jpg	281	54621	194.381	2.845	255				
10x3 Dead1.jpg	238	35898	150.832	1.87	255	468	49.14529915		
10x3 Live1.jpg	230	45510	197.87	2.37	255				
10x4 Dead1.jpg	194	28408	146.433	1.48	255	578	66.43598616		
10x4 Live1.jpg	384	77219	201.091	4.022	255				

Static									
Slice	Count	Total Area	Average Size	%Area	Mean	Total Cells	% Live	AVG % Live	STD DEV
10x2 Dead1.jpg	298	33807	113.446	1.761	255	734	59.40054496	55.51329431	3.181738587
10x2 Live1.jpg	436	58852	134.982	3.065	255				
10x3 Dead1.jpg	213	27360	128.451	1.425	255	479	55.53235908		
10x3 Live1.jpg	266	39478	148.414	2.056	255				
10x4 Dead1.jpg	527	86344	163.841	4.497	255	1089	51.60697888		
10x4 Live1.jpg	562	98644	175.523	5.138	255				

Table 8: Middle Inner Day 2 Raw Data

Middle Inner Day 2									
1.5									
Slice	Count	Total Area	Average Size	%Area	Mean	Total Cells	% Live	AVG % Live	STD DEV
10x1 Dead1.jpg	90	15534	172.6	0.809	255	219	58.90410959	52.01150148	5.922366647
10x1 Live1.jpg	129	22734	176.233	1.184	255				
10x2 Dead1.jpg	245	61063	249.237	3.18	255	441	44.44444444		
10x2 Live1.jpg	196	50261	256.434	2.618	255				
10x3 Dead1.jpg	229	38135	166.528	1.986	255	484	52.68595041		
10x3 Live1.jpg	255	48907	191.792	2.547	255				

9									
Slice	Count	Total Area	Average Size	%Area	Mean	Total Cells	% Live	AVG % Live	STD DEV
10x1 Dead1.jpg	149	17837	119.711	0.929	255	335	55.52238806	44.69950144	7.704445963
10x1 Live1.jpg	186	25013	134.478	1.303	255				
10x2 Dead1.jpg	398	88439	222.209	4.606	255	644	38.19875776		
10x2 Live1.jpg	246	45391	184.516	2.364	255				
10x4 Dead1.jpg	316	48703	154.123	2.537	255	530	40.37735849		
10x4 Live1.jpg	214	38940	181.963	2.028	255				

Silicone									
Slice	Count	Total Area	Average Size	%Area	Mean	Total Cells	% Live	AVG % Live	STD DEV
10x1 Dead1.jpg	102	20005	196.127	1.042	255	278	63.30935252	72.53821987	14.50873325
10x1 Live1.jpg	176	38998	221.58	2.031	255				
10x2 Dead1.jpg	151	26572	175.974	1.384	255	390	61.28205128		
10x2 Live1.jpg	239	44569	186.481	2.321	255				
10x5 Dead1.jpg	21	3498	166.571	0.182	255	301	93.02325581		
10x5 Live1.jpg	280	64725	231.161	3.371	255				

Single Tube									
Slice	Count	Total Area	Average Size	%Area	Mean	Total Cells	% Live	AVG % Live	STD DEV
10x1 Dead1.jpg	143	17600	195.556	0.917	255	315	54.6031746	49.19596607	3.856926534
10x1 Live1.jpg	172	32531	219.804	1.694	255				
10x2 Dead1.jpg	59	11535	195.508	0.601	255	109	45.87155963		
10x2 Live1.jpg	50	14711	294.22	0.766	255				
10x3 Dead1.jpg	229	24480	255	1.275	255	433	47.11316397		
10x3 Live1.jpg	204	44845	262.251	2.336	255				

Static									
Slice	Count	Total Area	Average Size	%Area	Mean	Total Cells	% Live	AVG % Live	STD DEV
10x2 Dead1.jpg	368	73436	199.554	3.825	255	499	26.25250501	19.04019191	5.431124904
10x2 Live1.jpg	131	25186	192.26	1.312	255				
10x3 Dead1.jpg	403	66281	164.469	3.452	255	464	13.14655172		
10x3 Live1.jpg	61	9373	153.656	0.488	255				
10x4 Dead1.jpg	195	30211	154.928	1.573	255	237	17.72151899		
10x4 Live1.jpg	42	8897	211.833	0.463	255				

Table 9: Middle Outer Day 1 Raw Data

Middle Outer Day 1									
1.5									
Slice	Count	Total Area	Average Size	%Area	Mean	Total Cells	% Live	AVG % Live	STD DEV
10x3 Dead1.jpg	193	33948	175.896	1.768	255	447	56.82326622	58.43290253	3.636313546
10x3 Live1.jpg	254	40206	158.291	2.094	255				
10x4 Dead1.jpg	236	33676	142.695	1.754	255	646	63.46749226		
10x4 Live1.jpg	410	71400	174.146	3.719	255				
10x5 Dead1.jpg	283	39343	139.021	2.049	255	629	55.00794913		
10x5 Live1.jpg	346	57636	166.578	3.002	255				

9									
Slice	Count	Total Area	Average Size	%Area	Mean	Total Cells	% Live	AVG % Live	STD DEV
10x2 Dead1.jpg	83	10966	132.12	0.571	255	244	65.98360656	65.13580999	2.289823931
10x2 Live1.jpg	161	24081	149.571	1.254	255				
10x3 Dead1.jpg	130	19537	150.285	1.018	255	399	67.41854637		
10x3 Live1.jpg	269	46266	171.993	2.41	255				
10x4 Dead1.jpg	144	21687	150.604	1.13	255	379	62.00527704		
10x4 Live1.jpg	235	38019	161.783	1.98	255				

Silicone									
Slice	Count	Total Area	Average Size	%Area	Mean	Total Cells	% Live	AVG % Live	STD DEV
10x2 Dead1.jpg	220	32661	148.459	1.701	255	558	60.5734767	58.60320054	3.675310142
10x2 Live1.jpg	338	66241	195.979	3.45	255				
10x3 Dead1.jpg	364	43684	120.011	2.275	255	782	53.45268542		
10x3 Live1.jpg	418	71648	171.407	3.732	255				
10x4 Dead1.jpg	120	19031	158.592	0.991	255	314	61.78343949		
10x4 Live1.jpg	194	32595	168.015	1.698	255				

Single Tube									
Slice	Count	Total Area	Average Size	%Area	Mean	Total Cells	% Live	AVG % Live	STD DEV
10x1 Dead1.jpg	169	27114	160.438	1.412	255	464	63.57758621	62.01554293	1.198483492
10x1 Live1.jpg	295	55156	186.969	2.873	255				
10x2 Dead1.jpg	142	21026	148.07	1.095	255	361	60.66481994		
10x2 Live1.jpg	219	42612	194.575	2.219	255				
10x3 Dead1.jpg	199	29671	149.101	1.545	255	521	61.80422265		
10x3 Live1.jpg	322	57450	178.416	2.992	255				

Static									
Slice	Count	Total Area	Average Size	%Area	Mean	Total Cells	% Live	AVG % Live	STD DEV
10x2 Dead1.jpg	298	33807	113.446	1.761	255	734	59.40054496	55.51329431	3.181738587
10x2 Live1.jpg	436	58852	134.982	3.065	255				
10x3 Dead1.jpg	213	27360	128.451	1.425	255	479	55.53235908		
10x3 Live1.jpg	266	39478	148.414	2.056	255				
10x4 Dead1.jpg	527	86344	163.841	4.497	255	1089	51.60697888		
10x4 Live1.jpg	562	98644	175.523	5.138	255				

Table 10: Middle Outer Day 2 Raw Data

Middle Outer Day 2									
1.5									
Slice	Count	Total Area	Average Size	%Area	Mean	Total Cells	% Live	AVG % Live	STD DEV
10x1 Dead1.jpg	148	26929	181.953	1.403	255	369	59.89159892	59.3604882	3.706519039
10x1 Live1.jpg	221	36750	166.29	1.914	255				
10x3 Dead1.jpg	131	23776	181.496	1.238	255	360	63.61111111		
10x3 Live1.jpg	229	47639	208.031	2.481	255				
10x4 Dead1.jpg	124	16999	137.089	0.885	255	273	54.57875458		
10x4 Live1.jpg	149	25602	171.826	1.333	255				

9									
Slice	Count	Total Area	Average Size	%Area	Mean	Total Cells	% Live	AVG % Live	STD DEV
10x1 Dead1.jpg	193	40785	211.321	2.124	255	326	40.79754601	42.26761454	4.240233978
10x1 Live1.jpg	133	19669	147.887	1.024	255				
10x2 Dead1.jpg	232	39328	169.517	2.048	255	374	37.96791444		
10x2 Live1.jpg	142	24560	172.958	1.279	255				
10x3 Dead1.jpg	278	47874	172.209	2.493	255	535	48.03738318		
10x3 Live1.jpg	257	49713	193.436	2.589	255				

Silicone									
Slice	Count	Total Area	Average Size	%Area	Mean	Total Cells	% Live	AVG % Live	STD DEV
10x1 Dead1.jpg	53	9452	178.34	0.492	255	242	78.09917355	68.37495076	10.81775697
10x1 Live1.jpg	189	42640	225.608	2.221	255				
10x2 Dead1.jpg	256	59983	234.309	3.124	255	548	53.28467153		
10x2 Live1.jpg	292	51897	177.729	2.703	255				
10x3 Dead1.jpg	73	15315	209.795	0.798	255	278	73.74100719		
10x3 Live1.jpg	205	38187	186.278	1.989	255				

Single Tube									
Slice	Count	Total Area	Average Size	%Area	Mean	Total Cells	% Live	AVG % Live	STD DEV
10x1 Dead1.jpg	72	10740	149.167	0.559	255	235	69.36170213	63.86969723	3.928131234
10x1 Live1.jpg	163	46738	286.736	2.434	255				
10x2 Dead1.jpg	95	21340	224.632	1.111	255	249	61.84738956		
10x2 Live1.jpg	154	27338	177.519	1.424	255				
10x3 Dead1.jpg	99	16941	171.121	0.882	255	250	60.4		
10x3 Live1.jpg	151	29060	192.45	1.514	255				

Static									
Slice	Count	Total Area	Average Size	%Area	Mean	Total Cells	% Live	AVG % Live	STD DEV
10x1 Dead1.jpg	157	31393	199.955	1.635	255	300	47.66666667	47.78127468	0.527657703
10x1 Live1.jpg	143	25022	174.979	1.303	255				
10x3 Dead1.jpg	132	24179	183.174	1.259	255	250	47.2		
10x3 Live1.jpg	118	15034	127.407	0.783	255				
10x4 Dead1.jpg	203	35054	172.68	1.826	255	394	48.47715736		
10x4 Live1.jpg	191	31325	164.005	1.632	255				

Table 11: Top Inner Day 1 Raw Data

Top Inner Day 1									
1.5									
Slice	Count	Total Area	Average Size	%Area	Mean	Total Cells	% Live	AVG % Live	STD DEV
10x1 Dead1.jpg	247	44405	179.777	2.313	255	620	60.16129032	60.78250496	3.038131842
10x1 Live1.jpg	373	69476	186.263	3.619	255				
10x2 Dead1.jpg	180	22935	127.417	1.195	255	511	64.77495108		
10x2 Live1.jpg	331	66308	200.326	3.454	255				
10x3 Dead1.jpg	204	41153	201.73	2.143	255	479	57.41127349		
10x3 Live1.jpg	275	59717	217.153	3.11	255				

9									
Slice	Count	Total Area	Average Size	%Area	Mean	Total Cells	% Live	AVG % Live	STD DEV
10x2 Dead1.jpg	132	16833	127.523	0.877	255	319	58.62068966	60.86678062	2.583858135
10x2 Live1.jpg	187	42307	226.241	2.203	255				
10x3 Dead1.jpg	114	16549	145.167	0.862	255	321	64.48598131		
10x3 Live1.jpg	207	44922	217.014	2.34	255				
10x4 Dead1.jpg	160	29152	182.2	1.518	255	395	59.49367089		
10x4 Live1.jpg	235	49339	209.953	2.57	255				

Silicone									
Slice	Count	Total Area	Average Size	%Area	Mean	Total Cells	% Live	AVG % Live	STD DEV
10x1 Dead1.jpg	141	19901	141.142	1.037	255	377	62.5994695	60.14698449	1.945218047
10x1 Live1.jpg	236	46288	196.136	2.411	255				
10x2 Dead1.jpg	250	61758	247.032	3.217	255	593	57.84148398		
10x2 Live1.jpg	343	59351	173.035	3.091	255				
10x3 Dead1.jpg	170	30164	177.435	1.571	255	425	60		
10x3 Live1.jpg	255	48246	189.2	2.513	255				

Single Tube									
Slice	Count	Total Area	Average Size	%Area	Mean	Total Cells	% Live	AVG % Live	STD DEV
10x2 Dead1.jpg	151	28788	190.649	1.499	255	382	60.47120419	59.16169769	2.581575981
10x2 Live1.jpg	231	43785	189.545	2.28	255				
10x3 Dead1.jpg	156	30752	197.128	1.602	255	351	55.55555556		
10x3 Live1.jpg	195	35240	180.718	1.835	255				
10x4 Dead1.jpg	185	30322	163.903	1.579	255	480	61.45833333		
10x4 Live1.jpg	295	57027	193.312	2.97	255				

Static									
Slice	Count	Total Area	Average Size	%Area	Mean	Total Cells	% Live	AVG % Live	STD DEV
10x2 Dead1.jpg	298	33807	113.446	1.761	255	734	59.40054496	55.51329431	3.181738587
10x2 Live1.jpg	436	58852	134.982	3.065	255				
10x3 Dead1.jpg	213	27360	128.451	1.425	255	479	55.53235908		
10x3 Live1.jpg	266	39478	148.414	2.056	255				
10x4 Dead1.jpg	527	86344	163.841	4.497	255	1089	51.60697888		
10x4 Live1.jpg	562	98644	175.523	5.138	255				

Table 12: Top Inner Day 2 Raw Data

Top Inner Day 2									
1.5									
Slice	Count	Total Area	Average Size	%Area	Mean	Total Cells	% Live	AVG % Live	STD DEV
10x1 Dead1.jpg	118	25208	213.627	1.313	255	306	61.4379085	61.57923368	5.226448878
10x1 Live1.jpg	188	38869	206.75	2.024	255				
10x2 Dead1.jpg	77	13380	173.766	0.697	255	241	68.04979253		
10x2 Live1.jpg	164	25866	157.72	1.347	255				
10x3 Dead1.jpg	179	35428	197.922	1.845	255	400	55.25		
10x3 Live1.jpg	221	50807	229.896	2.646	255				

9									
Slice	Count	Total Area	Average Size	%Area	Mean	Total Cells	% Live	AVG % Live	STD DEV
10x1 Dead1.jpg	46	5409	117.587	0.282	255	244	81.14754098	76.24382952	3.640800487
10x1 Live1.jpg	198	47491	239.854	2.473	255				
10x3 Dead1.jpg	41	5098	124.341	0.266	255	165	75.15151515		
10x3 Live1.jpg	124	21825	176.008	1.137	255				
10x4 Dead1.jpg	102	12750	125	0.664	255	370	72.43243243		
10x4 Live1.jpg	268	55591	207.429	2.895	255				

Silicone									
Slice	Count	Total Area	Average Size	%Area	Mean	Total Cells	% Live	AVG % Live	STD DEV
10x1 Dead1.jpg	37	5250	141.892	0.273	255	230	83.91304348	81.46561665	1.831347192
10x1 Live1.jpg	193	38669	200.358	2.014	255				
10x3 Dead1.jpg	50	7116	142.32	0.371	255	244	79.50819672		
10x3 Live1.jpg	194	49026	252.711	2.553	255				
10x4 Dead1.jpg	39	6220	159.487	0.324	255	205	80.97560976		
10x4 Live1.jpg	166	34410	207.289	1.792	255				

Single Tube									
Slice	Count	Total Area	Average Size	%Area	Mean	Total Cells	% Live	AVG % Live	STD DEV
10x1 Dead1.jpg	78	16150	207.051	0.841	255	225	65.33333333	55.65884194	9.382145132
10x1 Live1.jpg	147	32981	224.361	1.718	255				
10x2 Dead1.jpg	81	13255	163.642	0.69	255	142	42.95774648		
10x2 Live1.jpg	61	9333	153	0.486	255				
10x3 Dead1.jpg	88	17884	203.227	0.931	255	213	58.68544601		
10x3 Live1.jpg	125	34054	272.432	1.774	255				

Static									
Slice	Count	Total Area	Average Size	%Area	Mean	Total Cells	% Live	AVG % Live	STD DEV
10x1 Dead1.jpg	222	42040	189.369	2.19	255	406	45.32019704	41.71272943	4.681672898
10x1 Live1.jpg	184	29453	160.071	1.534	255				
10x2 Dead1.jpg	293	56085	191.416	2.921	255	530	44.71698113		
10x2 Live1.jpg	237	34907	147.287	1.818	255				
10x4 Dead1.jpg	257	45520	177.121	2.371	255	396	35.1010101		
10x4 Live1.jpg	139	25176	181.122	1.311	255				

Table 13: Top Outer Day 1 Raw Data

Top Outer Day 1									
1.5									
Slice	Count	Total Area	Average Size	%Area	Mean	Total Cells	% Live	AVG % Live	STD DEV
10x2 Dead1.jpg	126	23489	186.421	1.223	255	429	70.62937063	67.21615767	3.858991529
10x2 Live1.jpg	303	64478	212.799	3.358	255				
10x3 Dead1.jpg	142	25949	182.739	1.352	255	461	69.19739696		
10x3 Live1.jpg	319	67961	213.044	3.54	255				
10x5 Dead1.jpg	197	38358	194.711	1.998	255	516	61.82170543		
10x5 Live1.jpg	319	61840	193.856	3.221	255				

9									
Slice	Count	Total Area	Average Size	%Area	Mean	Total Cells	% Live	AVG % Live	STD DEV
10x2 Dead1.jpg	258	41762	161.868	2.175	255	627	58.85167464	64.30342314	5.136341861
10x2 Live1.jpg	369	76570	207.507	3.988	255				
10x3 Dead1.jpg	85	13211	155.424	0.688	255	295	71.18644068		
10x3 Live1.jpg	210	41490	197.571	2.161	255				
10x4 Dead1.jpg	212	30722	144.915	1.6	255	571	62.87215412		
10x4 Live1.jpg	359	76281	212.482	3.973	255				

Silicone									
Slice	Count	Total Area	Average Size	%Area	Mean	Total Cells	% Live	AVG % Live	STD DEV
10x1 Dead1.jpg	227	29815	131.344	1.553	255	633	64.13902054	69.28495136	17.44056302
10x1 Live1.jpg	406	67842	167.099	3.533	255				
10x2 Dead1.jpg	19	2410	126.842	0.126	255	262	92.7480916		
10x2 Live1.jpg	243	40661	167.329	2.118	255				
10x3 Dead1.jpg	304	52789	173.648	2.749	255	620	50.96774194		
10x3 Live1.jpg	316	73190	231.614	3.812	255				

Single Tube									
Slice	Count	Total Area	Average Size	%Area	Mean	Total Cells	% Live	AVG % Live	STD DEV
10x2 Dead1.jpg	193	36940	191.399	1.924	255	491	60.69246436	57.50172892	2.320376099
10x2 Live1.jpg	298	56541	189.735	2.945	255				
10x3 Dead1.jpg	195	37806	193.877	1.969	255	449	56.5701559		
10x3 Live1.jpg	254	55839	219.839	2.908	255				
10x4 Dead1.jpg	286	40486	141.559	2.109	255	639	55.24256651		
10x4 Live1.jpg	353	78323	221.878	4.079	255				

Static									
Slice	Count	Total Area	Average Size	%Area	Mean	Total Cells	% Live	AVG % Live	STD DEV
10x2 Dead1.jpg	298	33807	113.446	1.761	255	734	59.40054496	55.51329431	3.181738587
10x2 Live1.jpg	436	58852	134.982	3.065	255				
10x3 Dead1.jpg	213	27360	128.451	1.425	255	479	55.53235908		
10x3 Live1.jpg	266	39478	148.414	2.056	255				
10x4 Dead1.jpg	527	86344	163.841	4.497	255	1089	51.60697888		
10x4 Live1.jpg	562	98644	175.523	5.138	255				

Table 14: Top Outer Day 2 Raw Data

Top Outer Day 2									
1.5									
Slice	Count	Total Area	Average Size	%Area	Mean	Total Cells	% Live	AVG % Live	STD DEV
10x2 Dead1.jpg	36	6359	176.639	0.331	255	242	85.12396694	77.58355065	13.3175751
10x2 Live1.jpg	206	38889	188.782	2.025	255				
10x3 Dead1.jpg	167	24024	143.856	1.251	255	406	58.86699507		
10x3 Live1.jpg	239	52811	220.967	2.751	255				
10x4 Dead1.jpg	29	3359	115.828	0.175	255	258	88.75968992		
10x4 Live1.jpg	229	55778	243.572	2.905	255				

9									
Slice	Count	Total Area	Average Size	%Area	Mean	Total Cells	% Live	AVG % Live	STD DEV
10x1 Dead1.jpg	103	20629	200.282	1.074	255	292	64.7260274	63.63474053	1.452528909
10x1 Live1.jpg	189	46726	247.228	2.434	255				
10x3 Dead1.jpg	68	10961	161.191	0.571	255	177	61.5819209		
10x3 Live1.jpg	109	14344	131.596	0.747	255				
10x4 Dead1.jpg	114	21155	185.57	1.102	255	322	64.59627329		
10x4 Live1.jpg	208	45257	217.582	2.357	255				

Silicone									
Slice	Count	Total Area	Average Size	%Area	Mean	Total Cells	% Live	AVG % Live	STD DEV
10x1 Dead1.jpg	12	1306	108.833	0.068	255	195	93.84615385	81.82139036	8.557922769
10x1 Live1.jpg	183	36199	197.809	1.885	255				
10x2 Dead1.jpg	72	10402	144.472	0.542	255	313	76.99680511		
10x2 Live1.jpg	241	39518	163.975	2.058	255				
10x4 Dead1.jpg	67	9223	137.657	0.48	255	264	74.62121212		
10x4 Live1.jpg	197	42765	217.081	2.227	255				

Single Tube									
Slice	Count	Total Area	Average Size	%Area	Mean	Total Cells	% Live	AVG % Live	STD DEV
10x1 Dead1.jpg	86	8318	96.721	0.433	255	298	71.1409396	60.00701192	8.452925339
10x1 Live1.jpg	212	54194	255.632	2.823	255				
10x2 Dead1.jpg	147	24387	165.898	1.27	255	298	50.67114094		
10x2 Live1.jpg	151	34278	227.007	1.785	255				
10x3 Dead1.jpg	140	28539	203.85	1.486	255	335	58.20895522		
10x3 Live1.jpg	195	46416	238.031	2.418	255				

Static									
Slice	Count	Total Area	Average Size	%Area	Mean	Total Cells	% Live	AVG % Live	STD DEV
10x1 Dead1.jpg	222	42040	189.369	2.19	255	406	45.32019704	41.71272943	4.681672898
10x1 Live1.jpg	184	29453	160.071	1.534	255				
10x2 Dead1.jpg	293	56085	191.416	2.921	255	530	44.71698113		
10x2 Live1.jpg	237	34907	147.287	1.818	255				
10x4 Dead1.jpg	257	45520	177.121	2.371	255	396	35.1010101		
10x4 Live1.jpg	139	25176	181.122	1.311	255				

Appendix B: Calculations

All equations were first solved by hand, and then transferred to the Engineering Equation Solver software, where they were verified, and units were checked.

File:1:\EES\Bioreactor Flow Rate.EES

10/26/2015 10:36:30 AM Page 1

EES Ver. 9.911: #3856: For use only by students and faculty, A. James Clark School of Engineering, University of Maryland

```
r1=(.25/2)*convert(in,mm)
r2=(.75/2)*convert(in,mm)
a1=pi*r1^2
a2=pi*r2^2
Q1=3*convert(ml/min,mm^3/s)
v1=Q1/a1
v2=v1
Q2=v2*a2
Q2_mL=Q2*convert(mm^3/s,mL/min)
```

SOLUTION

Unit Settings: SI C kPa J mass deg

a1 = 31.67 [mm²]

Q1 = 50 [mm³/s]

Q2_mL = 27 [mL/min]

r2 = 9.525 [mm]

v2 = 1.579 [mm/s]

a2 = 285 [mm²]

Q2 = 450 [mm³/s]

r1 = 3.175 [mm]

v1 = 1.579 [mm/s]

No unit problems were detected.

"Henry's Law to Calculate Molar Concentration of O2"

T_star=298[k] "Henry's Law coefficients are given at 25C"
 T_room=37+273 "Incubator Temp"
 k_H_star=769.23 [L-atm/mol] "Henry Coefficient for Water at 25C"
 H=1700[k] "Enthalpy of Dissolution constant"
 K_H_room=k_H_star*exp(-H*(1/T_room-1/T_star)) "Calculate Henry's Law Coefficient at 37C"
 O_air=.2095*.95 "Percent oxygen =20.95% in air, but 5% CO2 pumped in as well"
 O_death=.04 "4 percent oxygen set as floor"
 P_o2_20=O_air*1[atm] "Partial Pressure of oxygen in air"
 P_o2_death=O_death*1[atm] "Partial Pressure of oxygen in hypoxic environment"
 C_20=(P_o2_20/k_H_room)*convert(mol/L, mol/m^3) "Concentration of oxygen in air-saturated media"
 C_4=(P_o2_death/k_H_room)*convert(mol/L, mol/m^3) "Concentration of oxygen in air-saturated media"

"Diffusivity of Platinum-Cured Silicone"

P_silicone=(796.1*10^(-10))*convert(cm^3-mm/(sec-cm^2-mmHg),m^3-m/(sec-m^2-mmHg)) "Permeation rate from Cole-Parmer Catalog"
 delta_silicone=.125*convert(in, m) "Wall thickness of silicone tubing = 1/8 inch"
 p_1=152[mmHg] "Partial Pressure of Oxygen in air"
 p_2=0[mmHg] "Initial partial pressure on inside wall of tubing"
 J_p_silicone=-P_silicone*(p_2-p_1)/delta_silicone "Calculate Fick's Law Flux"
 J_L_silicone=J_p_silicone*1000[L]/1[m^3] "Get J in terms of liters"
 {T_room=37+273 "37 degrees C"}
 T_STP=0+273 "STP"
 V_STP=22.4[L/mol] "Ideal Gas Law"
 T_25=25+273
 V_25=V_STP*T_25/T_STP "Calculate volume of each mole of gas to correct for temperature increase to 25C"
 J_m_silicone=J_L_silicone/V_25 "Get J in terms of moles"
 C_1=.21 [mol/m^3] "Henry's Law concentration of oxygen"
 C_2=0 [mol/m^3] "Initial concentration of oxygen on inside wall"
 J_m_silicone=-D_silicone*(C_2-C_1)/delta_silicone "Calculate Diffusivity using Fick's Law"
 S_silicone_0=P_silicone/D_silicone "Solubility of O2 in Tubing"
 S_silicone_room=S_silicone_0*exp(H/T_room)
 {c=S_silicone_0*p
 p=152}

"Diffusivity of FEP Tubing"

Delta_p_FEP=-1724*convert(kPa,mmHg)
 Delta_p_room=-152[mmHg]
 C_FEP_paper=((Delta_p_FEP*convert(mmHg,atm))/k_H_room)*convert(mol/L, mol/m^3) "Molar concentration of oxygen potential from paper"
 P_FEP_0=(1.4*10^(-10))*convert(cm^3-mm/(sec-cm^2-mmHg),m^3-m/(sec-m^2-mmHg)) "Permeation rate from Cole-Parmer Catalog"
 delta_FEP_paper=.05*convert(mm, m) "Film thickness=0.05mm"
 delta_FEP_room=1/16*convert(in, m) "Wall thcknes of FEP= 1/16 inch"
 J_p_FEP=-P_FEP_0*(Delta_p_FEP)/delta_FEP_paper "Calculate Fick's Law Flux"
 J_L_FEP=J_p_FEP*1000[L]/1[m^3] "Get J in terms of liters"
 J_m_FEP=J_L_FEP/V_25 "Get J in terms of moles"
 J_m_FEP=-D_FEP*(C_FEP_paper)/delta_FEP_paper "Calculate Diffusivity using Fick's Law"
 S_FEP=P_FEP_0/D_FEP "Solubility of O2 in Tubing"
 S_FEP_m=S_FEP*convert(m^3/(m^3-mmHg),L/(m^3-mmHg))/V_25 "get solubility in terms of moles"
 "Convert all values to correct for our thickness and pressure differential"
 J_p_FEP_room=-D_FEP*(C_2-C_1)/delta_FEP_room*V_25/(1000[L]/1[m^3]) "Assume constant diffusivity, calculate J at our thickness"
 J_p_FEP_room=-P_FEP_room*(Delta_p_room)/delta_FEP_room "Use Flux to back out Permeability at our thickness"
 S_FEP_room=P_FEP_room/D_FEP "Solubility of O2 in Tubing"
 S_FEP_room_m=S_FEP_room*convert(m^3/(m^3-mmHg),L/(m^3-mmHg))/V_25 "get solubility in terms of moles"
 C_o2_FEP_room=-delta_p_room*S_FEP_room_m

"Rate of Oxygen Consumption"

```
R_consumption=(.012*10^(-6)/10^6)*convert(mol/m^3-hr, mol/m^3-s) "Rate of O2 consumption by MSCs, divide by 10^6 to  
convert from rate per million to rate per cell"  
rho_s=100000 "Seeding density - cells/bead"  
r_bead=(3.54/2)*convert(mm,m) "radius of a bead"  
V_bead=4/3*pi*r_bead^3 "volume of a bead"  
R_consumption_bead=R_consumption*rho_s "consumption per bead"  
R_consumption_m=R_consumption_bead/V_bead "consumption per m^3"
```

"Alginate Permeability"

```
k=(1.2*10^(-12))*convert(cm^2, m^2) "Permeability of Alginate taken from literature values"  
P_room=101.325 [kPa] "Atmospheric Pressure"  
mu=viscosity(water, T=T_room, P=P_room)*convert(Pa-s, kPa-s) "viscosity of water at 37C"  
delta_p=101.325 [kPa] "pressure drop"  
L=70*convert(mm,m) "length of scaffold"  
A=pi*D^2/4 "cross-sectional area of construct"  
D=19.05*convert(mm,m) "Diameter of construct"  
Q=(k*A*delta_p/(mu*L))*convert(m^3/s, mL/min) "Calculated flow rate through alginate construct - Darcy's Law"
```

SOLUTION

Unit Settings: SI K kPa J mass deg

A = 0.000285 [m²]
C1 = 0.21 [mol/m³]
C2 = 0 [mol/m³]
C20 = 0.2075 [mol/m³]
C4 = 0.0417 [mol/m³]
CFEP,paper = -17.74 [mol/m³]
Co2,FEP,room = 0.21 [mol/m³]
D = 0.01905 [m]
δFEP,paper = 0.00005 [m]
δFEP,room = 0.001588 [m]
δp = 101.3 [kPa]
δp,FEP = -12931 [mmHg]
δp,room = -152 [mmHg]
δsilicone = 0.003175 [m]
DFEP = 4.174E-11 [m²/s]
Dsilicone = 2.357E-08 [m²/s]
H = 1700 [K]
JL,FEP = 0.0003621 [L/m²-s]
JL,silicone = 0.00003811 [L/m²-s]
Jm,FEP = 0.00001481 [mol/(m²-s)]
Jm,silicone = 0.000001559 [mol/(m²-s)]
Jp,FEP = 3.621E-07 [m³/(m²-s)]
Jp,FEP,room = 1.350E-10 [m³/(m²-s)]
Jp,silicone = 3.811E-08 [m³/(m²-s)]
k = 1.200E-16 [m²]
KH,room = 959.3 [L-atm/mol]
KH,star = 769.2 [L-atm/mol]
L = 0.07 [m]
μ = 6.939E-07 [kPa-s]
Oair = 0.199
Odeath = 0.04
p1 = 152 [mmHg]
p2 = 0 [mmHg]
PFEP,0 = 1.400E-15 [m³-m/(s-m²-mmHg)]
PFEP,room = 1.410E-15 [m³-m/(s-m²-mmHg)]
Po2,20 = 0.199 [atm]

Po2,death = 0.04 [atm]
Proom = 101.3 [kPa]
Psilicone = 7.961E-13 [m³-m/(s-m²-mmHg)]
Q = 0.004281 [mL/min]
ρs = 100000
Γbead = 0.00177 [m]
Rconsumption = 3.333E-18 [mol/s]
Rconsumption,bead = 3.333E-13 [mol/s]
Rconsumption,m = 1.435E-05 [mol/m³-s]
SFEP = 0.00003354 [m³/(m³-mmHg)]
SFEP,m = 0.001372 [mol/m³-mmHg]
SFEP,room = 0.00003378 [m³/(m³-mmHg)]
SFEP,room,m = 0.001382 [mol/m³-mmHg]
Ssilicone,0 = 0.00003378 [m³/(m³-mmHg)]
Ssilicone,room = 0.008134 [m³/(m³-mmHg)]
T25 = 298 [K]
Troom = 310 [K]
Tstar = 298 [K]
TSTP = 273 [K]
V25 = 24.45 [L/mol]
Vbead = 2.323E-08 [m³]
VSTP = 22.4 [L/mol]

No unit problems were detected.

Appendix C: ImageJ Macro Procedures

ImageJ macros were written to allow for automated cell counting and image processing. This also ensured that all images were processed uniformly to prevent misrepresentation of data. These macros were then confirmed by hand-counting a few images to ensure that counts were accurate. Macros were created for each file by simply changing the file names to access corresponding images. Images were first processed, and then merged. Cell counts were obtained from individual live or dead images at 10x magnification.

```
open("C:\\Users\\Owen\\Desktop\\Box Sync\\Bioreactor Pics\\hMSC1 ImageJ Edits\\1.5\\BI\\2x1 Live.bmp");
run("Sharpen");
run("Sharpen");
run("Subtract Background...", "rolling=50");
run("Brightness/Contrast...");
setMinAndMax(15, 124);
saveAs("Jpeg", "C:\\Users\\Owen\\Desktop\\Box Sync\\Bioreactor Pics\\hMSC1 ImageJ Edits\\1.5\\BI\\2x1 Live1.jpg");
run("Close All");
```

Figure 38: ImageJ Image Processing Macro

```
open("C:\\Users\\Owen\\Desktop\\Box Sync\\Bioreactor Pics\\hMSC1 ImageJ Edits\\1.5\\BI\\2x1 Dead1.jpg");
open("C:\\Users\\Owen\\Desktop\\Box Sync\\Bioreactor Pics\\hMSC1 ImageJ Edits\\1.5\\BI\\2x1 Live1.jpg");
run("Add Image...", "image=[2x1 Dead1.jpg] x=0 y=0 opacity=50");
saveAs("Jpeg", "C:\\Users\\Owen\\Desktop\\Box Sync\\Bioreactor Pics\\hMSC1 ImageJ Edits\\1.5\\BI\\2x1 Merged.jpg");
run("Close");
run("Close");
```

Figure 39: ImageJ Image Overlay Macro

```
open("C:\\Users\\Owen\\Desktop\\Box Sync\\Bioreactor Pics\\hMSC1 ImageJ Edits\\1.5\\BI\\10x1 Dead1.jpg");
setOption("BlackBackground", false);
run("Convert to Mask");
run("Watershed");
run("Analyze Particles...", "size=50-400 show=Outlines display exclude clear summarize");
run("Close All");
open("C:\\Users\\Owen\\Desktop\\Box Sync\\Bioreactor Pics\\hMSC1 ImageJ Edits\\1.5\\BI\\10x1 Live1.jpg");
run("Convert to Mask");
run("Watershed");
run("Analyze Particles...", "size=50-400 show=Outlines display exclude clear summarize");
run("Close All");
```

Figure 40: ImageJ Counting Macro

Appendix D: Viability Analysis Graphical Results

All results depicted here follow the legend as outlined in Figure 41.

■ Silicone ■ Close Pore ■ Distant Pore ■ Single Tube ■ Static Control

Figure 41: Legend for All Viability Graphs

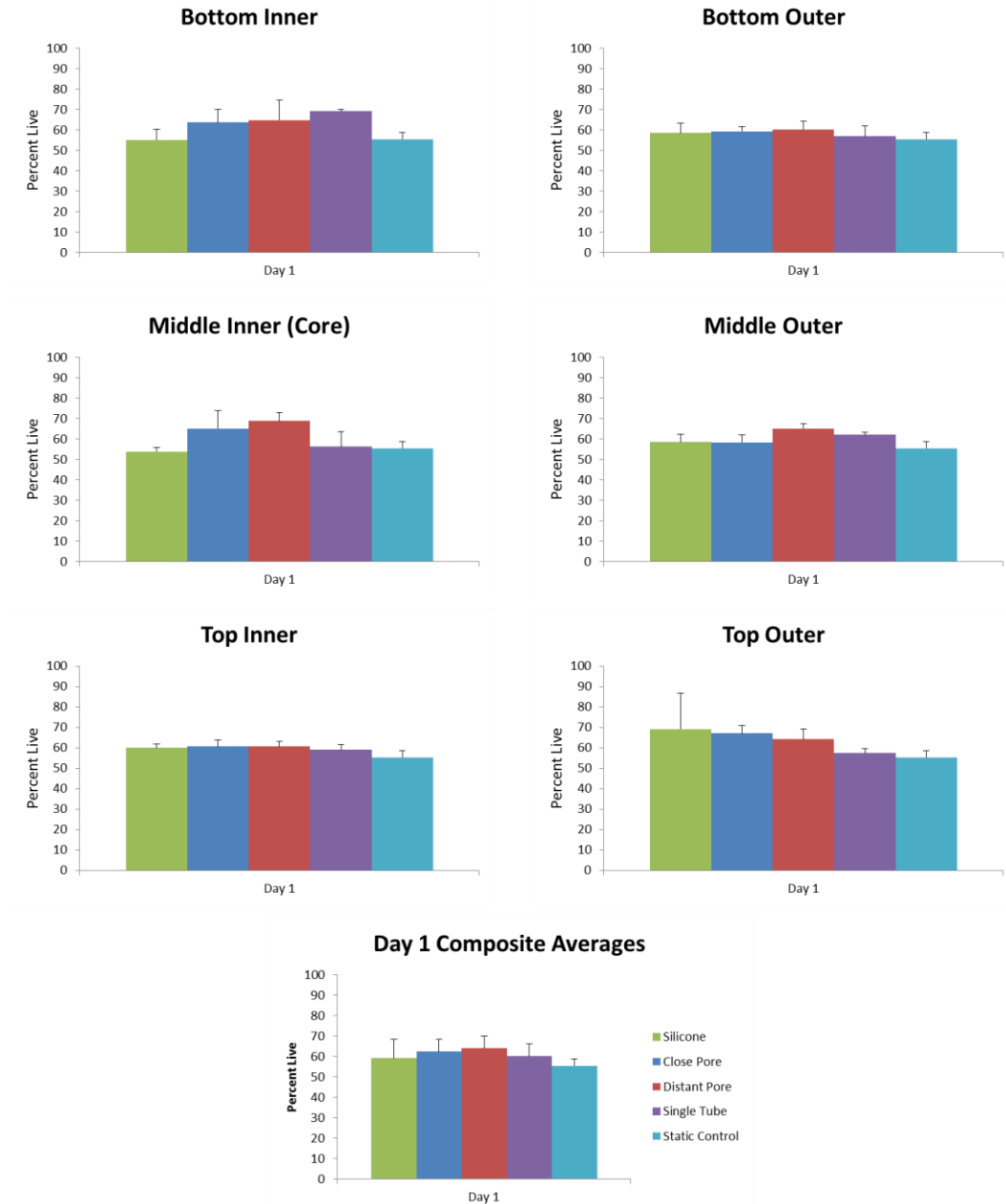


Figure 42: Day 1 Viability Results

Note that there is no statistical difference among any of the groups at any given harvest site.

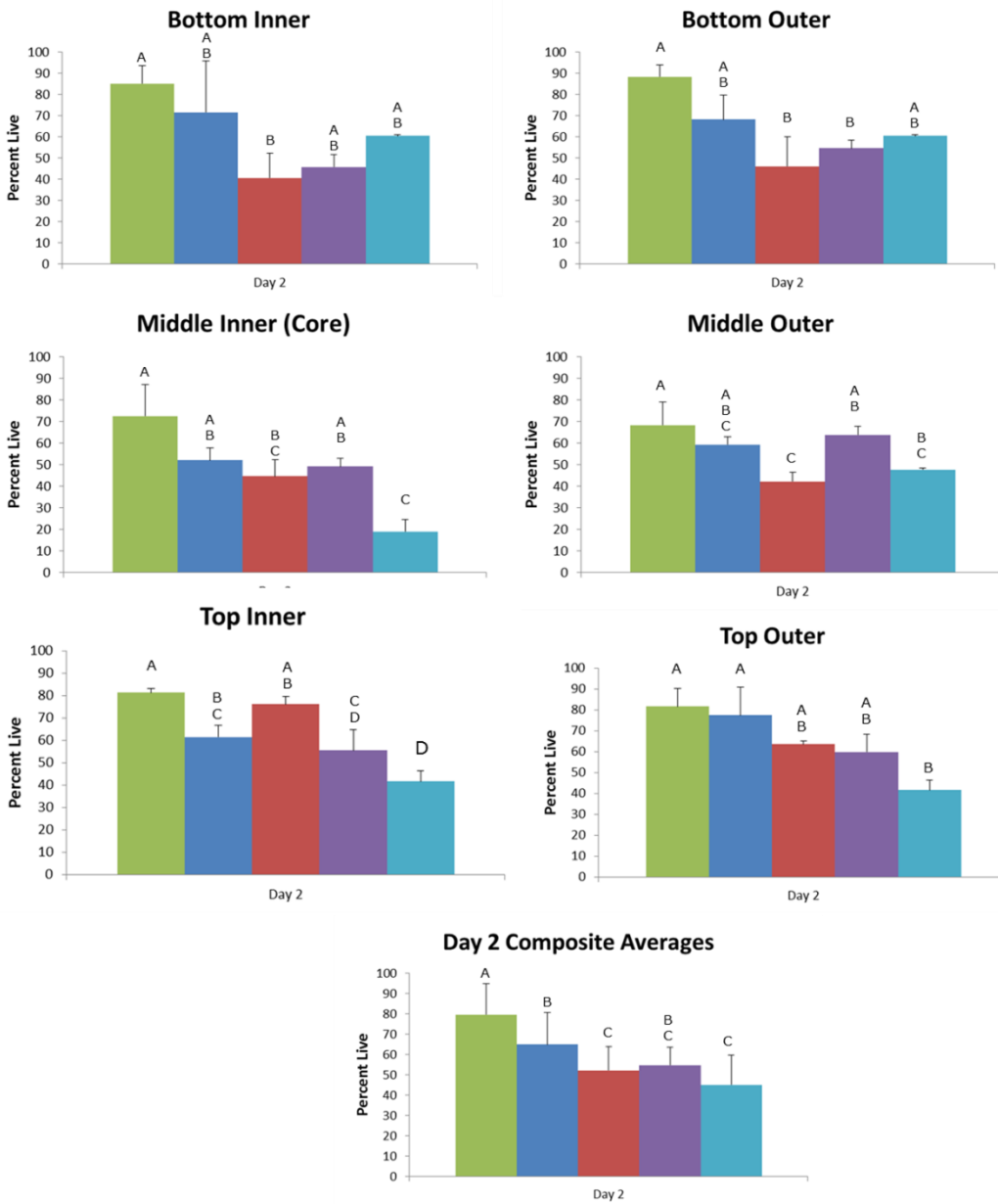
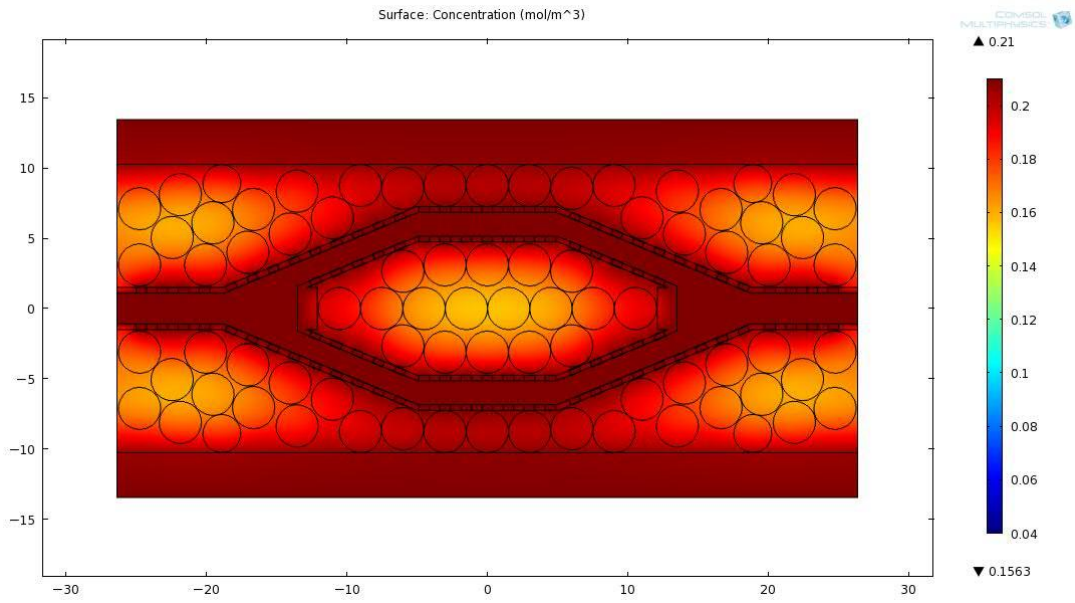
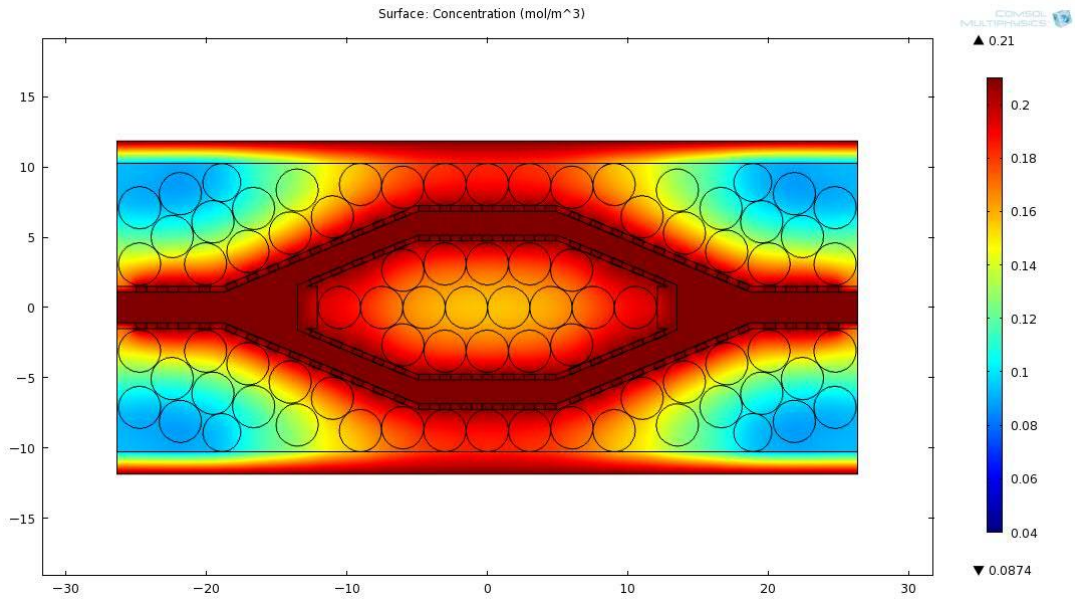


Figure 43: Day 2 Viability Results

In Figure 43, groups that do not share a letter are statistically different.

Appendix E: COMSOL Simulation Results



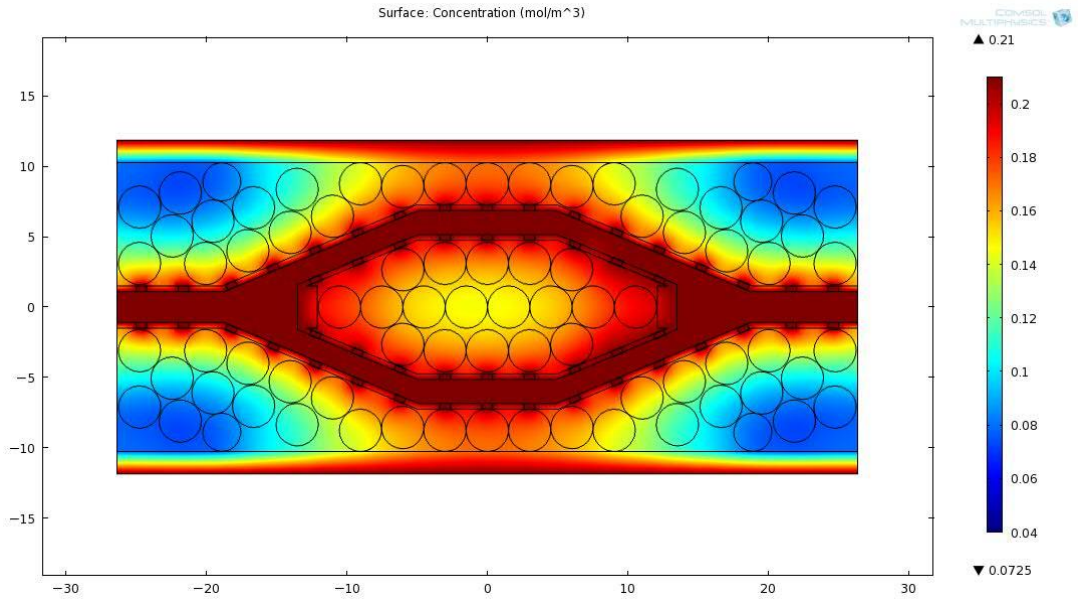


Figure 46: 3 mm Pore Spacing - Middle Branch, FEP

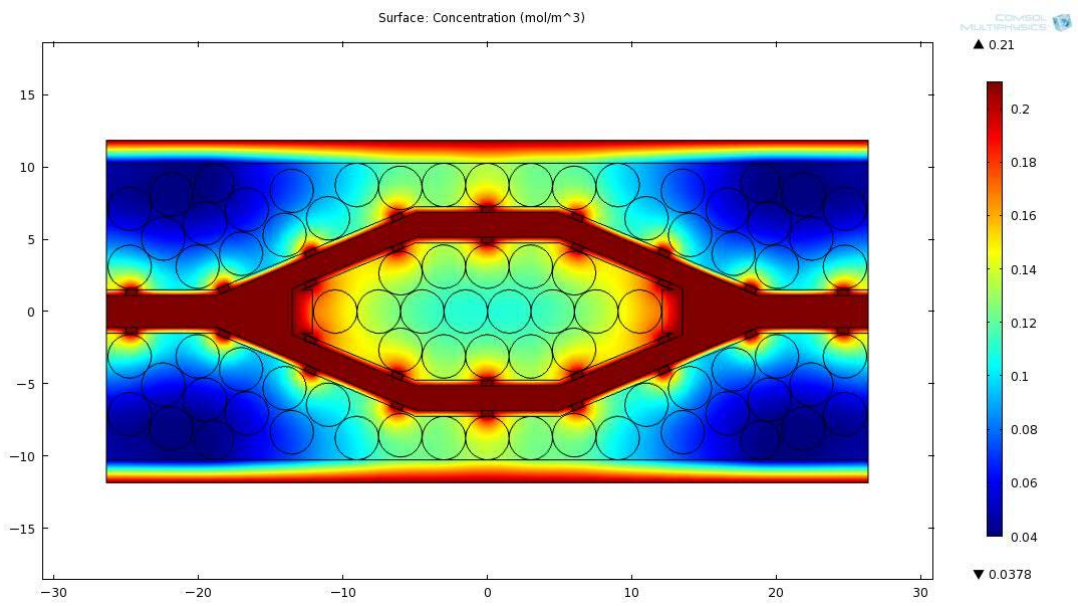


Figure 47: 6 mm Pore Spacing - Middle Branch, FEP

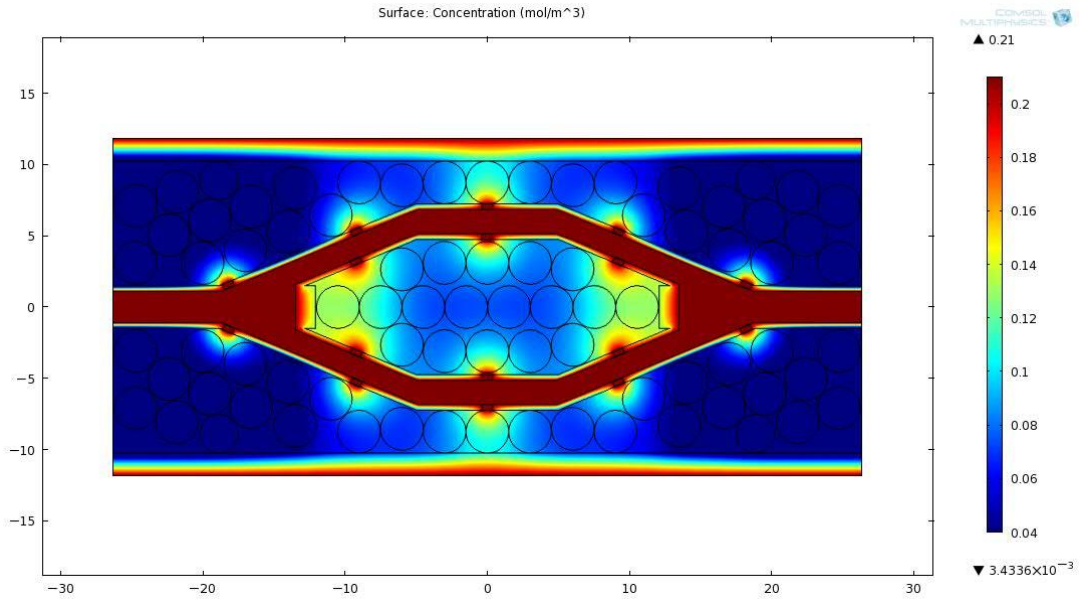


Figure 48: 9 mm Pore Spacing - Middle Branch, FEP

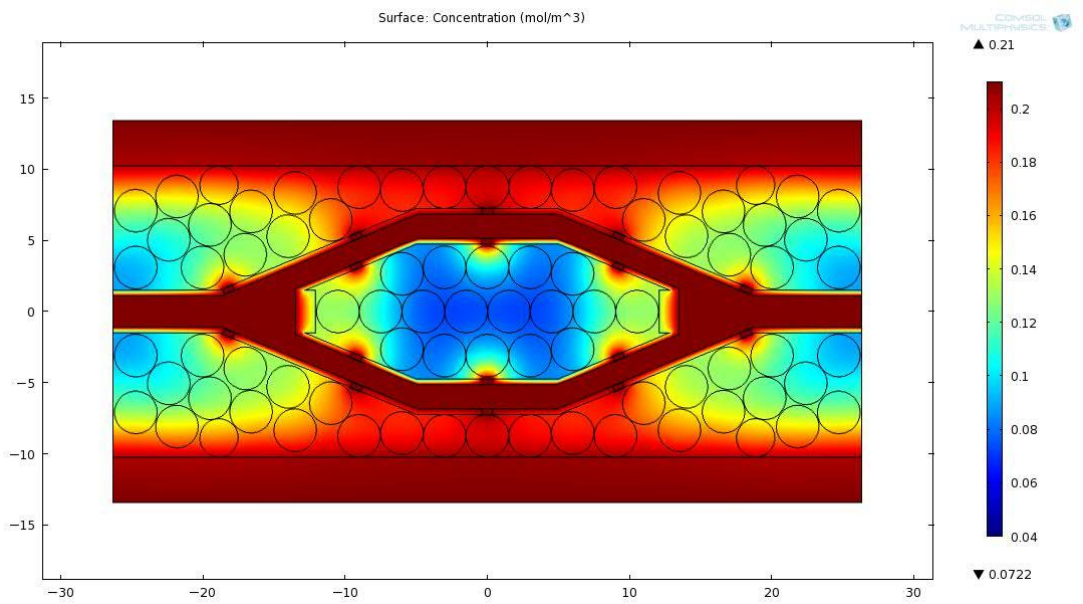
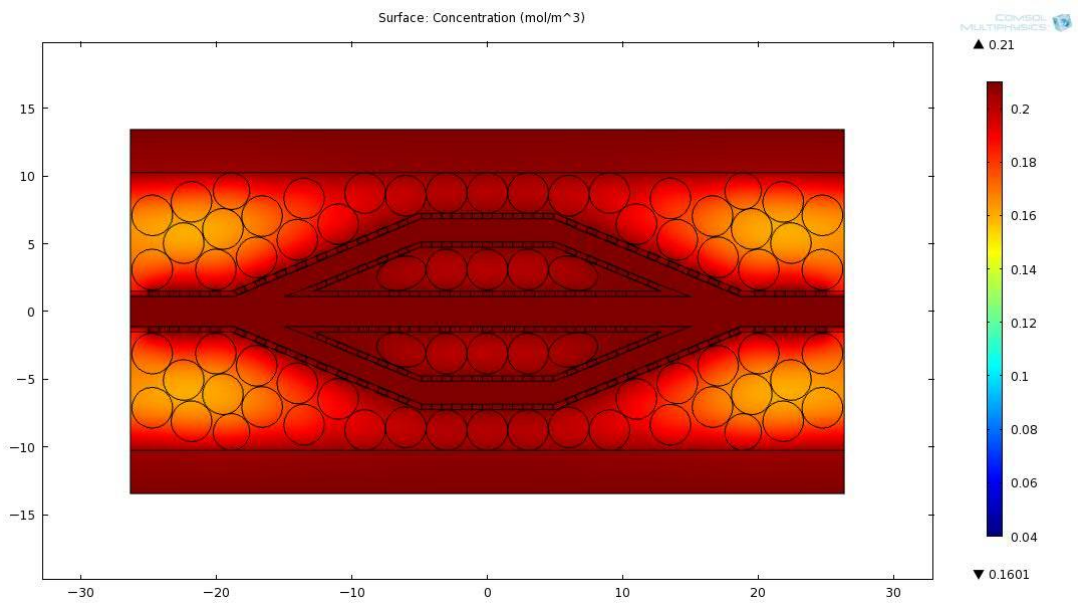
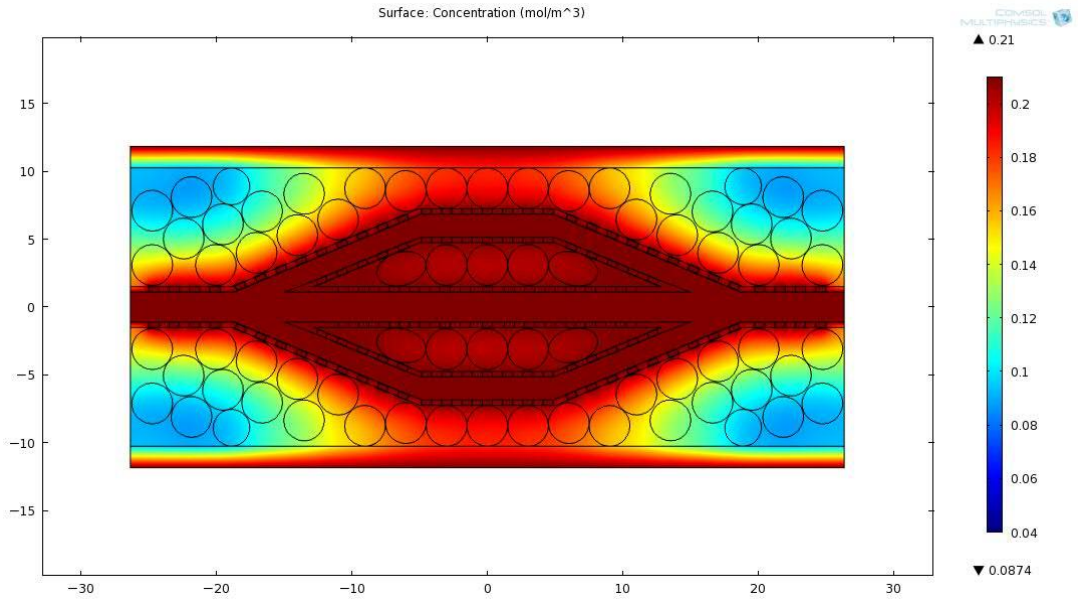


Figure 49: 9 mm Pore Spacing - Middle Branch, Silicone



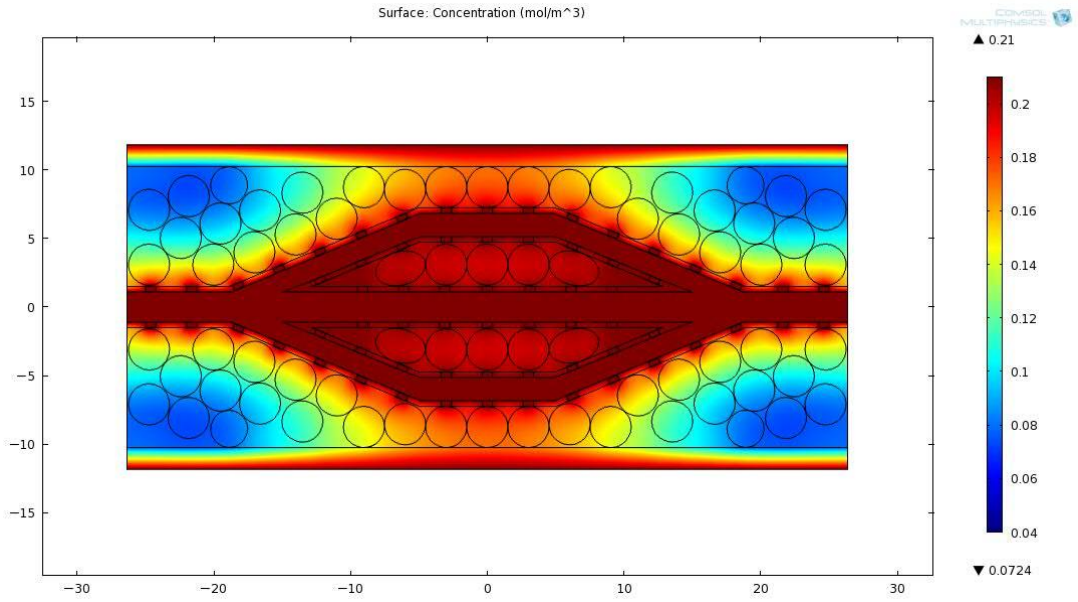


Figure 52: 3 mm Pore Spacing – Top/Bottom Branch, FEP

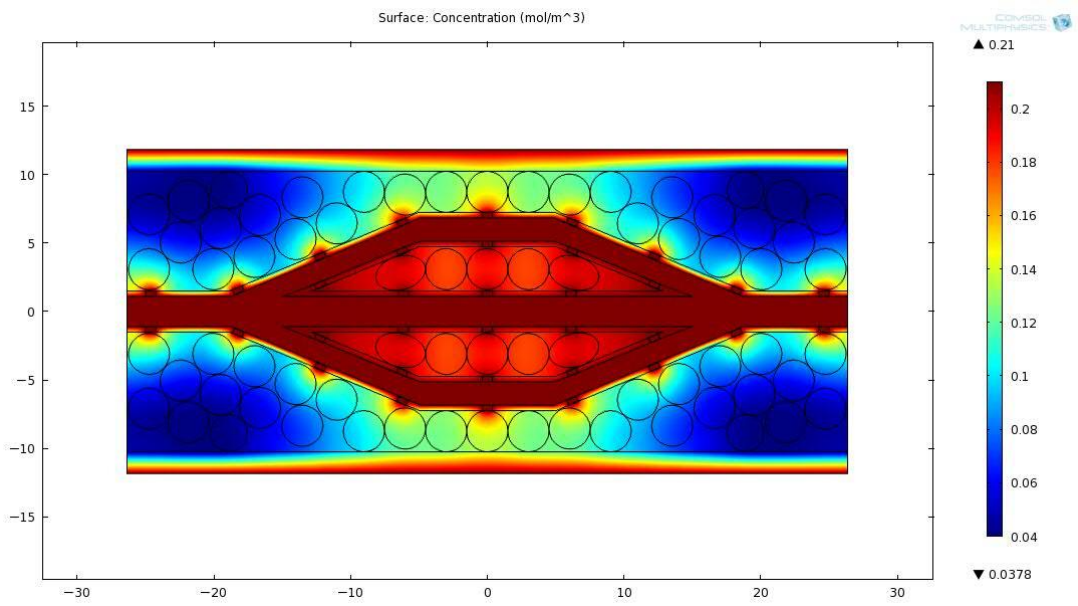


Figure 53: 6 mm Pore Spacing – Top/Bottom Branch, FEP

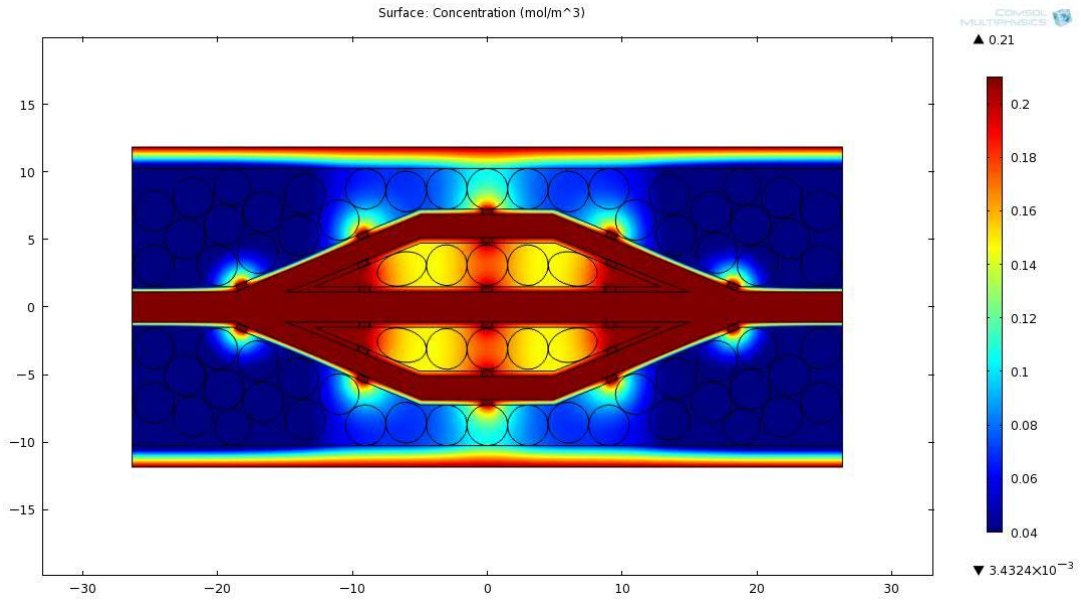


Figure 54: 9 mm Pore Spacing – Top/Bottom Branch, FEP

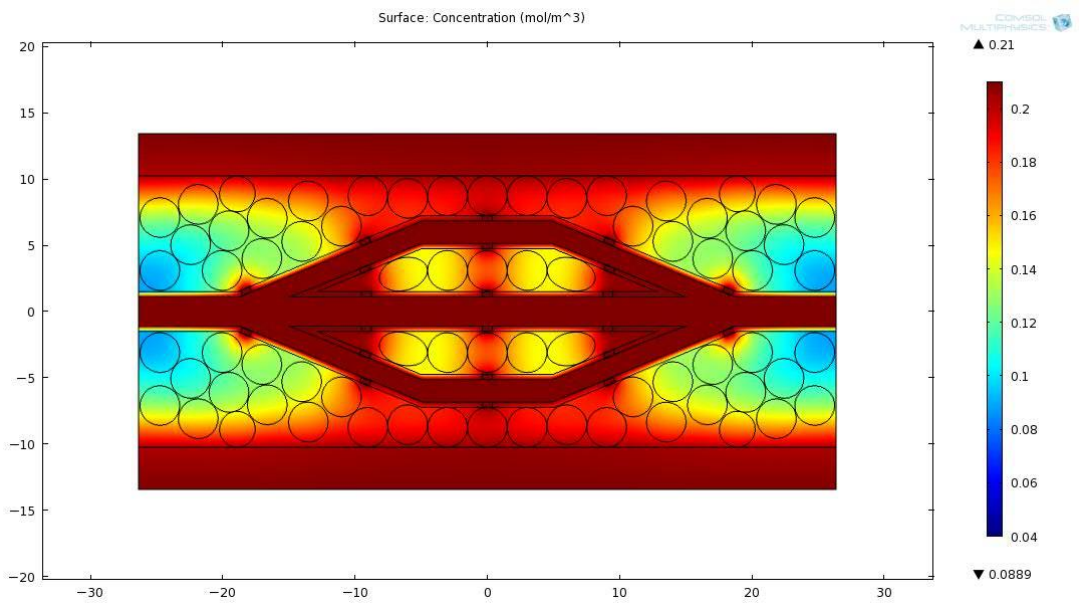
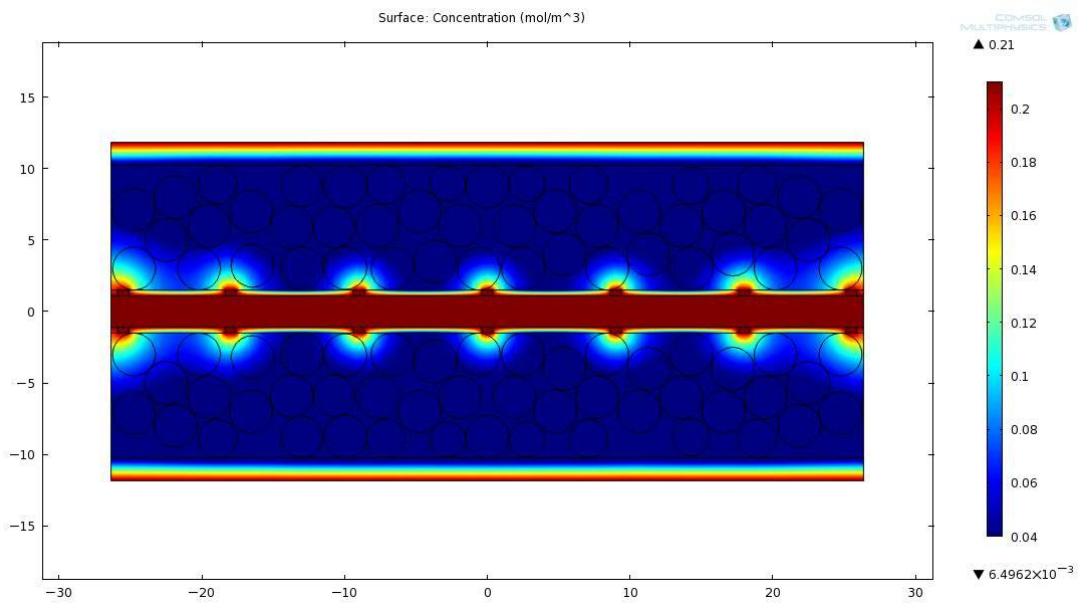
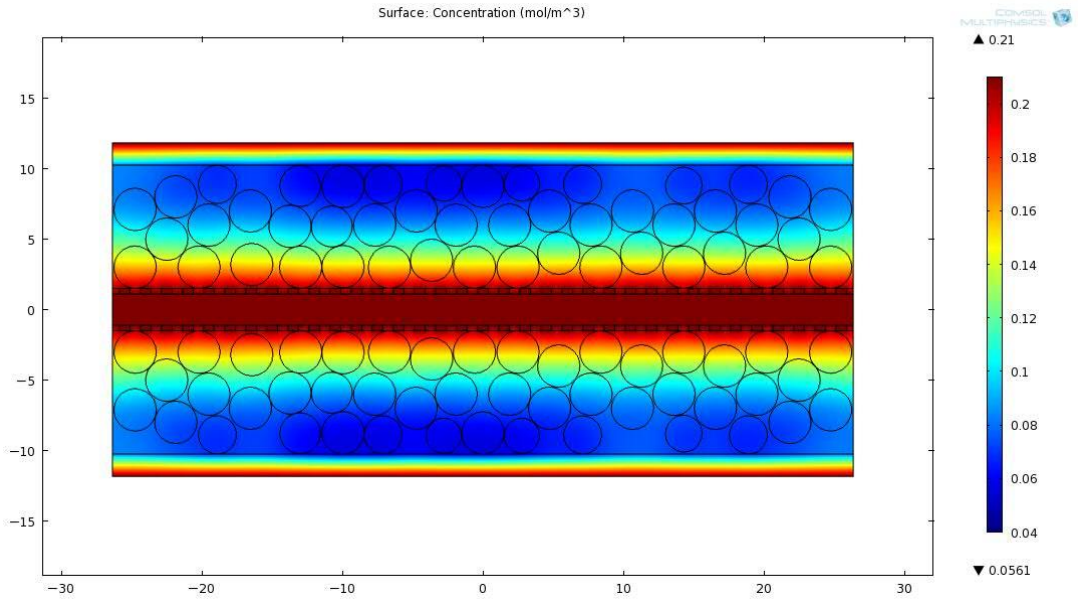


Figure 55: 9 mm Pore Spacing – Top/Bottom Branch, Silicone



Appendix F: SolidWorks CFD Results

All CFD results adhere to the legend set forth in Figure 58, unless otherwise stated.

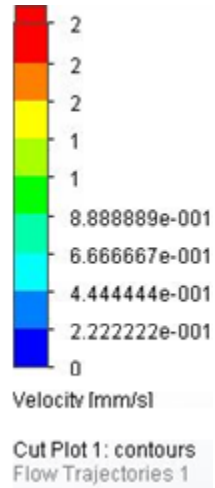


Figure 58: CFD Results Legend

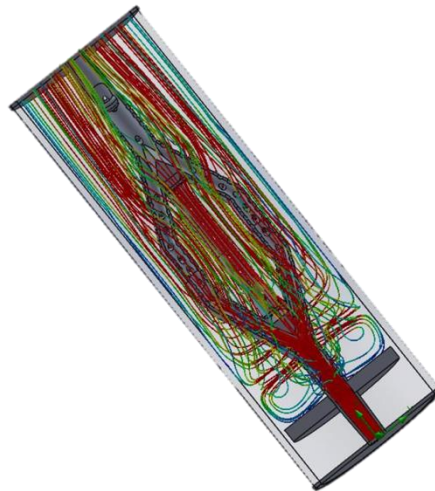


Figure 59: Close Pore Trajectory Profile

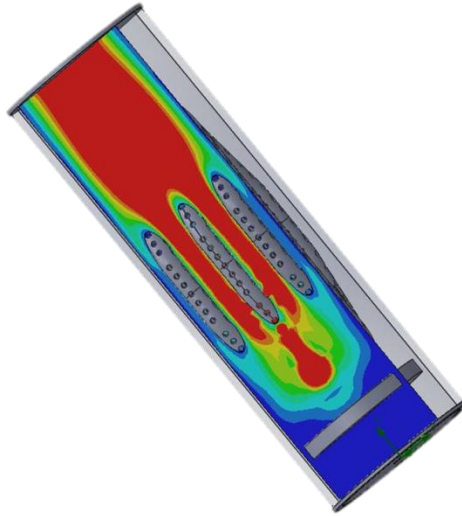


Figure 60: Close Pore Vertical Cut Plot, 5 mm Offset

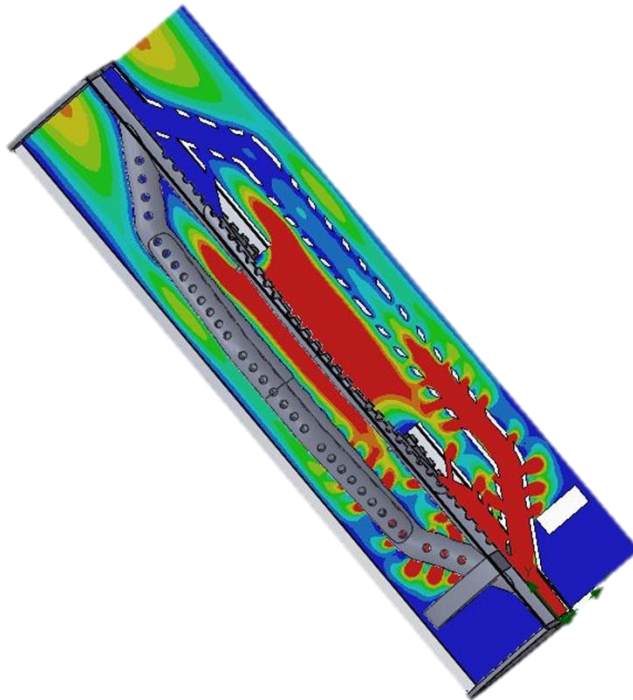


Figure 61: Close Pore Vertical Cut Plot

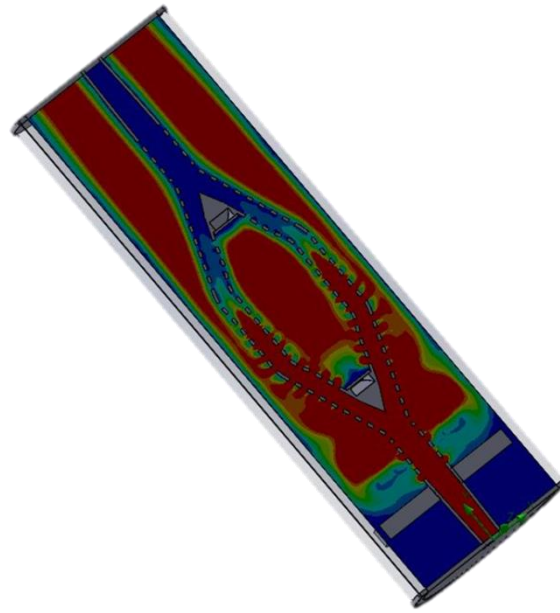


Figure 62: Close Pore Horizontal Cut Plot

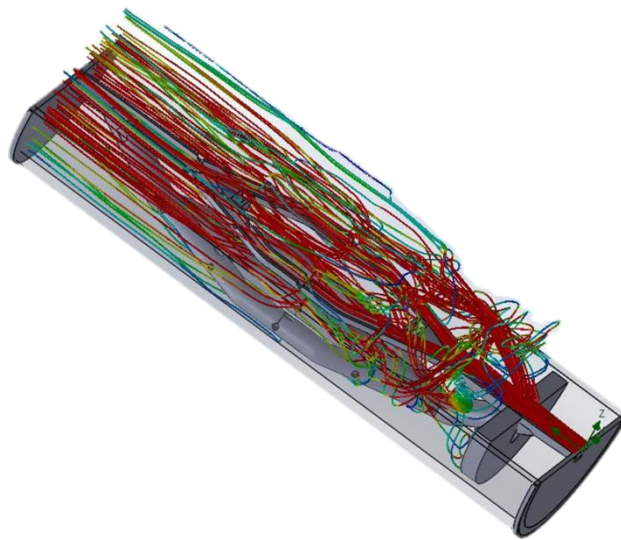


Figure 63: Distant Pore Trajectory Profile

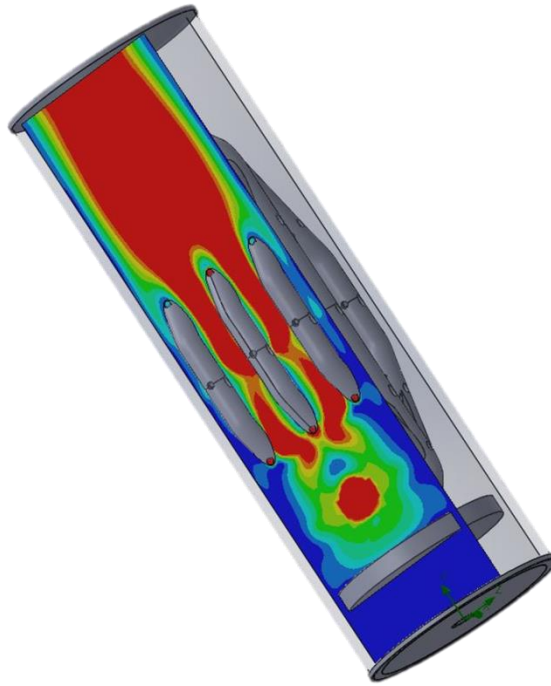


Figure 64: Distant Pore Vertical Cut Plot, 5 mm Offset

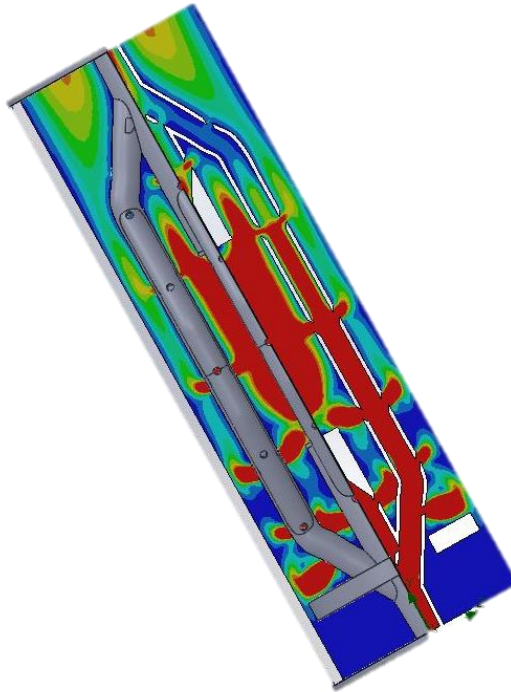


Figure 65: Distant Pore Vertical Cut Plot

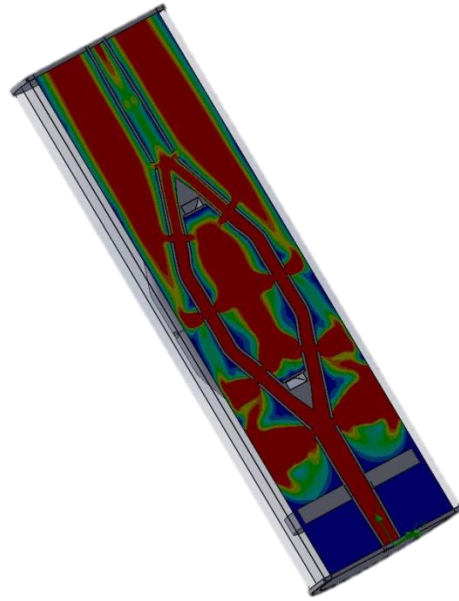


Figure 66: Distant Pore Horizontal Cut Plot

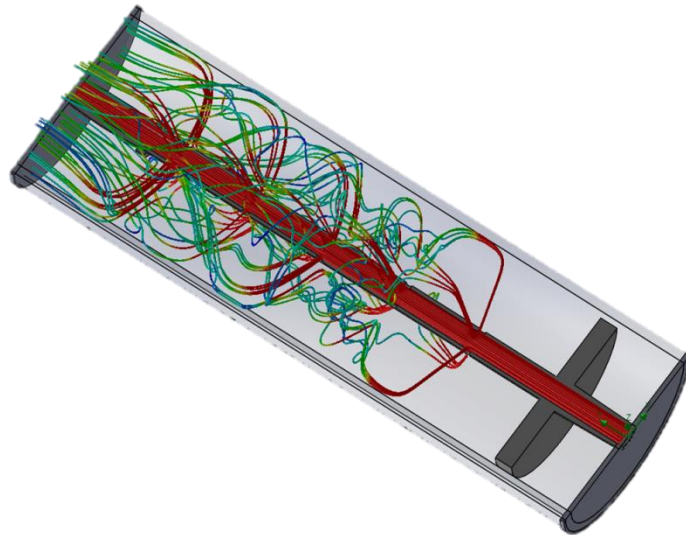


Figure 67: Single Tube Trajectory Profile

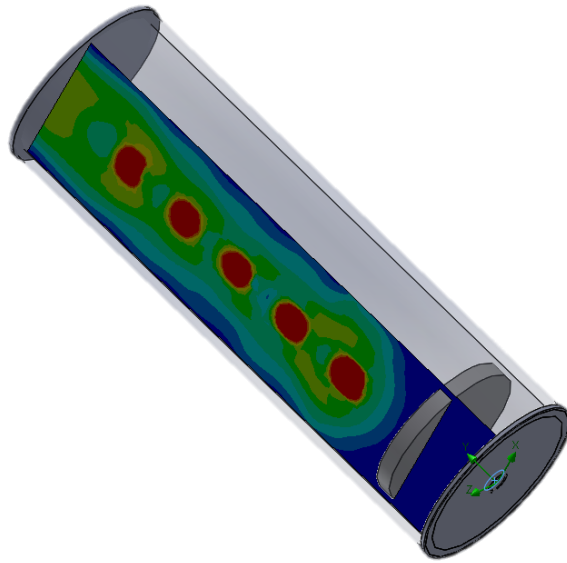


Figure 68: Single Tube Vertical Cut Plot, 5 mm Offset

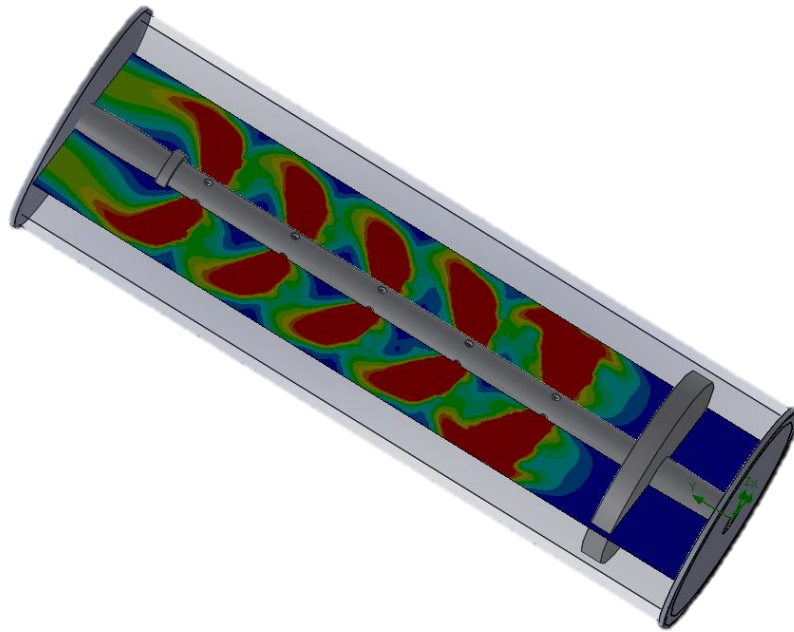


Figure 69: Single Tube Horizontal Cut Plot

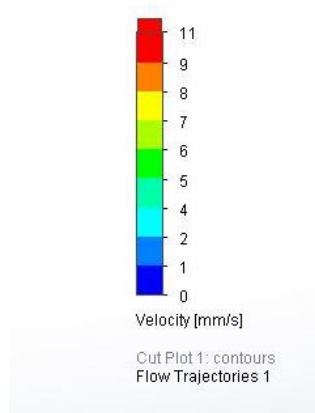


Figure 70: CFD Legend for Darcy Flow Simulations

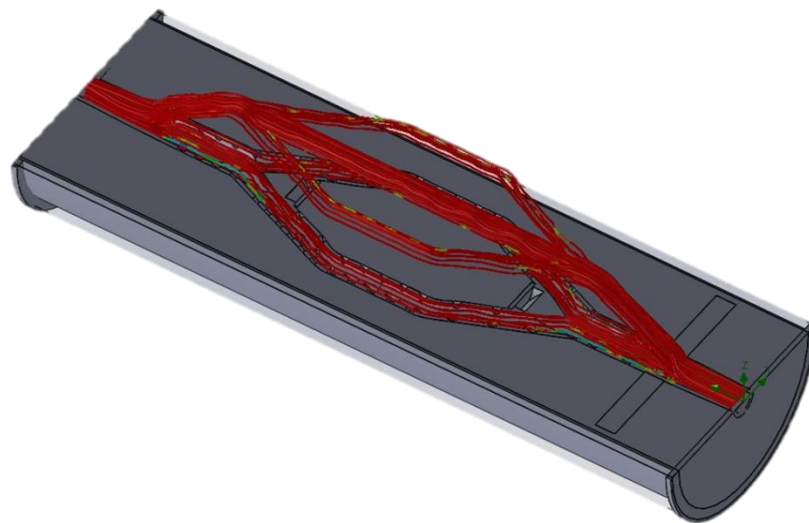


Figure 71: Darcy Trajectory Profile, Close Pore Group

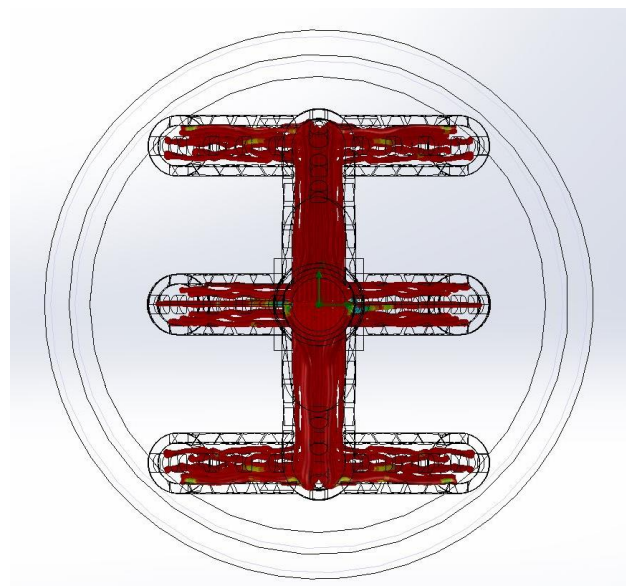


Figure 72: Darcy Trajectory Profile Rear View

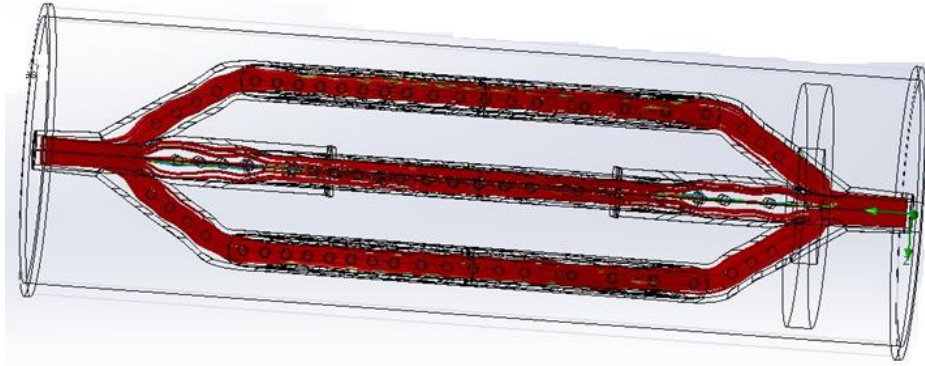


Figure 73: Darcy Trajectory Profile Side View

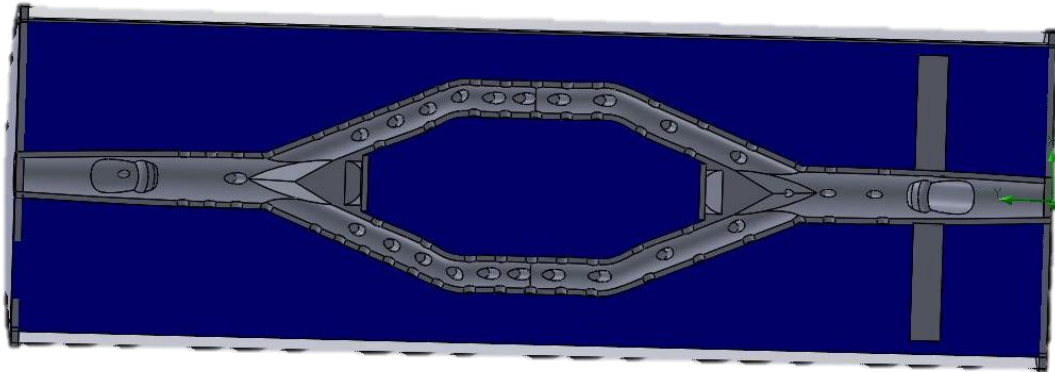


Figure 74: Darcy Horizontal Cut Plot, Pore Gradient Profile

Appendix F: Additional Bioreactor Pictures

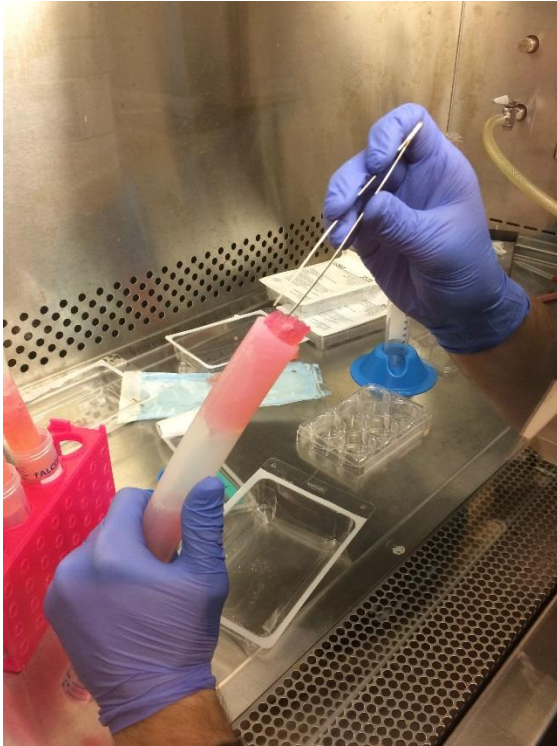


Figure 75: Day 2 Construct Extraction from Silicone Group

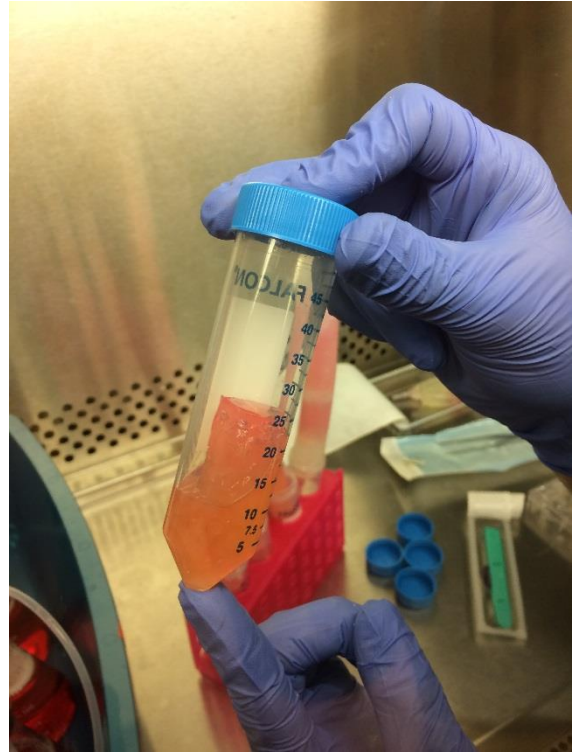


Figure 76: Static Control Aggregated Construct

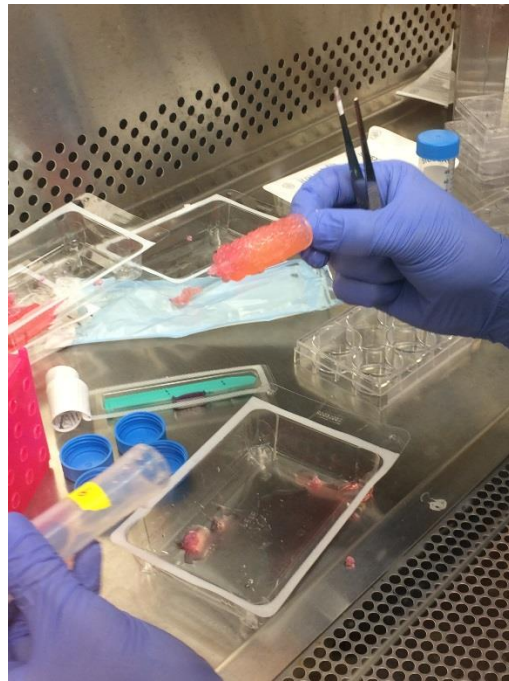


Figure 77: Day 2 Construct, Distant Pore Group



Figure 78: Trimmed Construct Demonstrates Complete Bead Infiltration

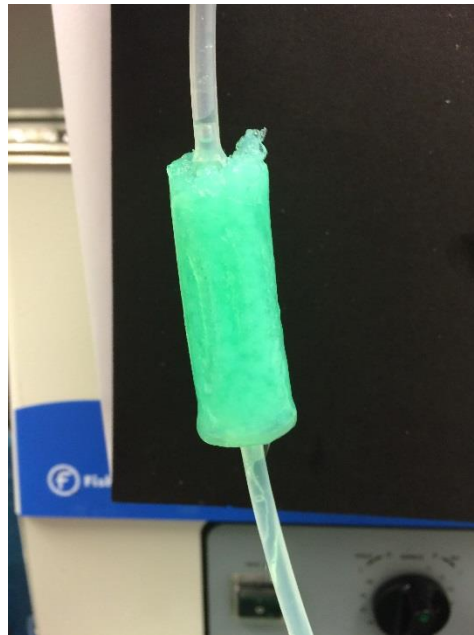


Figure 79: Re-perfusion of Constructs Demonstrates Potential for Anastomosis

Bibliography

1. Liu, Y., Lim, J. & Teoh, S. H. Review: Development of clinically relevant scaffolds for vascularised bone tissue engineering. *Biotechnol. Adv.* **31**, 688–705 (2013).
2. Ziegler-Graham, K., MacKenzie, E. J., Ephraim, P. L., Travison, T. G. & Brookmeyer, R. Estimating the Prevalence of Limb Loss in the United States: 2005 to 2050. *Arch. Phys. Med. Rehabil.* **89**, 422–429 (2008).
3. Sen, M. K. & Miclau, T. Autologous iliac crest bone graft: should it still be the gold standard for treating nonunions? . *Injury* **38 Suppl 1**, S75–80 (2007).
4. Matthews, D., Samdany, A. & Ahmed, S. U. An alternative management option for infected non-union of long bone fractures. *J. Clin. Orthop. Trauma* **4**, 43–45 (2013).
5. Calori, G. M. *et al.* Incidence of donor site morbidity following harvesting from iliac crest or RIA graft. *Injury* **45**, S116–S120 (2014).
6. Nonfatal Hospitalized Injuries, Both Sexes, All Ages , United States, 2010. *CDC WISQARS 2014*, (2014).
7. Laurencin, C. T., Ambrosio, A. M. A., Borden, M. D. & Cooper, J. A. Tissue Engineering: Orthopedic Applications. *Annu. Rev. Biomed. Eng.* **1**, 19–46 (1999).
8. Giannoudis, P. V, Dinopoulos, H. & Tsiridis, E. Bone substitutes: an update. *Injury* **36 Suppl 3**, S20–S27 (2005).
9. Giannoudis, P. V, Faour, O., Goff, T., Kanakaris, N. & Dimitriou, R. Masquelet technique for the treatment of bone defects: tips-tricks and future directions. *Injury* **42**, 591–8 (2011).
10. Klaue, K. *et al.* Bone regeneration in long-bone defects: tissue compartmentalisation? In vivo study on bone defects in sheep. *Injury* **40**, 95–102 (2009).
11. Wong, T. M. *et al.* Masquelet technique for treatment of posttraumatic bone defects. *ScientificWorldJournal.* **2014**, 710302 (2014).
12. Iacobellis, C., Berizzi, A. & Aldegheri, R. Bone transport using the Ilizarov method: A review of complications in 100 consecutive cases. *Strateg. Trauma Limb Reconstr.* **5**, 17–22 (2010).

13. Ilizarov, G. A. Clinical Application of the Tension-Stress Effect for Limb Lengthening. *Clinical Orthop. Relat. Res.* **250**, (1990).
14. Sladkova, M. & de Peppo, G. Bioreactor Systems for Human Bone Tissue Engineering. *Processes* **2**, 494–525 (2014).
15. Bertassoni, L. E. *et al.* Hydrogel bioprinted microchannel networks for vascularization of tissue engineering constructs. *Lab Chip* **14**, 2202–2211 (2014).
16. Bettahalli, N. M. S., Steg, H., Wessling, M. & Stamatialis, D. Development of poly(l-lactic acid) hollow fiber membranes for artificial vasculature in tissue engineering scaffolds. *J. Memb. Sci.* **371**, 117–126 (2011).
17. Kolesky, D. B. *et al.* 3D bioprinting of vascularized, heterogeneous cell-laden tissue constructs. *Adv. Mater.* **26**, 3124–30 (2014).
18. Tocchio, A. *et al.* Versatile fabrication of vascularizable scaffolds for large tissue engineering in bioreactor. *Biomaterials* **45**, 124–31 (2015).
19. Rouwkema, J., Rivron, N. C. & van Blitterswijk, C. a. Vascularization in tissue engineering. *Trends Biotechnol.* **26**, 434–441 (2008).
20. Liu, J., Zheng, H., Poh, P., Machens, H.-G. & Schilling, A. Hydrogels for Engineering of Perfusable Vascular Networks. *Int. J. Mol. Sci.* **16**, 15997–16016 (2015).
21. Yeatts, A. B., Choquette, D. T. & Fisher, J. P. Bioreactors to influence stem cell fate: Augmentation of mesenchymal stem cell signaling pathways via dynamic culture systems. *Biochim. Biophys. Acta - Gen. Subj.* **1830**, 2470–2480 (2013).
22. Duarte, L. R. The stimulation of bone growth by ultrasound. *Arch. Orthop. Trauma. Surg.* **101**, 153–9 (1983).
23. Yeatts, A. B. & Fisher, J. P. Bone tissue engineering bioreactors: Dynamic culture and the influence of shear stress. *Bone* **48**, 171–181 (2011).
24. Yeatts, A. B., Geibel, E. M., Fears, F. F. & Fisher, J. P. Human mesenchymal stem cell position within scaffolds influences cell fate during dynamic culture. *Biotechnol. Bioeng.* **109**, 2381–2391 (2012).
25. Yeatts, A. B. & Fisher, J. P. Tubular Perfusion System for the Long-Term Dynamic Culture of Human Mesenchymal Stem Cells. *Tissue Eng. Part C Methods* **17**, 337–348 (2011).

26. Yeatts, A. B., Gordon, C. N. & Fisher, J. P. Formation of an aggregated alginate construct in a tubular perfusion system. *Tissue Eng. Part C. Methods* **17**, 1171–8 (2011).
27. Braccini, I. & Pérez, S. Molecular basis of Ca²⁺-induced gelation in alginates and pectins: The egg-box model revisited. *Biomacromolecules* **2**, 1089–1096 (2001).
28. Robeson, M. J. Model of a tubular perfusion bioreactor using computational fluid dynamics. *Electron. Theses Diss.* (2015).
29. Wang, X.-M. & Waite, T. D. Gel layer formation and hollow fiber membrane filterability of polysaccharide dispersions. *J. Memb. Sci.* **322**, 204–213 (2008).
30. Hwang, C. M. *et al.* Fabrication of three-dimensional porous cell-laden hydrogel for tissue engineering. *Biofabrication* **2**, 035003 (2010).
31. Wang, X.-M. & Waite, T. D. Impact of gel layer formation on colloid retention in membrane filtration processes. *J. Memb. Sci.* **325**, 486–494 (2008).
32. Yeatts, A. B. *et al.* In Vivo Bone Regeneration Using Tubular Perfusion System Bioreactor Cultured Nanofibrous Scaffolds. *Tissue Eng. Part A* **20**, 139–146 (2014).
33. Gui, L. & Niklason, L. E. Vascular tissue engineering: Building perfusable vasculature for implantation. *Curr. Opin. Chem. Eng.* **3**, 68–74 (2014).
34. Zhao, L., Lee, V. K., Yoo, S.-S., Dai, G. & Intes, X. The integration of 3-D cell printing and mesoscopic fluorescence molecular tomography of vascular constructs within thick hydrogel scaffolds. *Biomaterials* **33**, 5325–5332 (2012).
35. Mironov, V., Boland, T., Trusk, T., Forgacs, G. & Markwald, R. R. Organ printing: computer-aided jet-based 3D tissue engineering. *Trends Biotechnol.* **21**, 157–161 (2003).
36. Skardal, A., Zhang, J. & Prestwich, G. D. Bioprinting vessel-like constructs using hyaluronan hydrogels crosslinked with tetrahedral polyethylene glycol tetracrylates. *Biomaterials* **31**, 6173–6181 (2010).
37. Annabi, N. *et al.* Controlling the porosity and microarchitecture of hydrogels for tissue engineering. *Tissue Eng. Part B. Rev.* **16**, 371–383 (2010).
38. Derby, B. Printing and Prototyping of Tissues and Scaffolds. *Science (80-.)*. **338**, 921–927 (2012).

39. Kim, S. S. *et al.* Survival and function of hepatocytes on a novel three-dimensional synthetic biodegradable polymer scaffold with an intrinsic network of channels. *Ann. Surg.* **228**, 8–13 (1998).
40. Yeong, W.-Y. *et al.* Rapid prototyping in tissue engineering: challenges and potential. *Trends Biotechnol.* **22**, 643–652 (2004).
41. Gauvin, R. *et al.* Microfabrication of complex porous tissue engineering scaffolds using 3D projection stereolithography. *Biomaterials* **33**, 3824–3834 (2012).
42. Cooke, M. N., Fisher, J. P., Dean, D., Rimnac, C. & Mikos, A. G. Use of stereolithography to manufacture critical-sized 3D biodegradable scaffolds for bone ingrowth. *J. Biomed. Mater. Res. B. Appl. Biomater.* **64**, 65–69 (2003).
43. Forgacs, G. Tissue engineering: Perfusable vascular networks. *Nat. Mater.* **11**, 746–747 (2012).
44. Miller, J. S. *et al.* Rapid casting of patterned vascular networks for perfusable engineered three-dimensional tissues. *Nat. Mater.* **11**, 768–774 (2012).
45. Bellan, L. M. *et al.* Fabrication of an artificial 3-dimensional vascular network using sacrificial sugar structures. *Soft Matter* **5**, 1354 (2009).
46. Wang, X.-Y. *et al.* Engineering interconnected 3D vascular networks in hydrogels using molded sodium alginate lattice as the sacrificial template. *Lab Chip* **14**, 2709 (2014).
47. Baker, B. M., Trappmann, B., Stapleton, S. C., Toro, E. & Chen, C. S. Microfluidics embedded within extracellular matrix to define vascular architectures and pattern diffusive gradients. *Lab Chip* **13**, 3246 (2013).
48. Matthew K. Gelber and Rohit Bhargava. Monolithic multilayer microfluidics via sacrificial molding of 3D-printed isomalt†. *R. Soc. Chem.* **15**, 1736–1741 (2015).
49. Bellan, L. M., Strychalski, E. A. & Craighead, H. G. Nanochannels fabricated in polydimethylsiloxane using sacrificial electrospun polyethylene oxide nanofibers. *J. Vac. Sci. Technol. B Microelectron. Nanom. Struct.* **26**, 1728 (2008).
50. Gualandi, C., Zucchelli, A., Fernández Osorio, M., Belcari, J. & Focarete, M. L. Nanovascularization of polymer matrix: generation of nanochannels and nanotubes by sacrificial electrospun fibers. *Nano Lett.* **13**, 5385–90 (2013).

51. Sandgren, T., Sonesson, B., Ahlgren, Å. R. & Länne, T. The diameter of the common femoral artery in healthy human: Influence of sex, age, and body size. *J. Vasc. Surg.* **29**, 503–510 (1999).
52. Zhao, F. *et al.* Effects of oxygen transport on 3-D human mesenchymal stem cell metabolic activity in perfusion and static cultures: Experiments and mathematical model. *Biotechnol. Prog.* **21**, 1269–1280 (2005).
53. Radisic, M. *et al.* Oxygen gradients correlate with cell density and cell viability in engineered cardiac tissue. *Biotechnol. Bioeng.* **93**, 332–343 (2006).
54. Volkmer, E. *et al.* Hypoxia in static and dynamic 3D culture systems for tissue engineering of bone. *Tissue Eng. Part A* **14**, 1331–1340 (2008).
55. Mohyeldin, A., Garzón-Muvdi, T. & Quiñones-Hinojosa, A. Oxygen in Stem Cell Biology: A Critical Component of the Stem Cell Niche. *Cell Stem Cell* **7**, 150–161 (2010).
56. Utting, J. C. *et al.* Hypoxia inhibits the growth, differentiation and bone-forming capacity of rat osteoblasts. *Exp. Cell Res.* **312**, 1693–1702 (2006).
57. Lennon, D. P., Edmison, J. M. & Caplan, a I. Cultivation of rat marrow-derived mesenchymal stem cells in reduced oxygen tension: effects on in vitro and in vivo osteochondrogenesis. *J. Cell. Physiol.* **187**, 345–355 (2001).
58. Harrison, J. S., Rameshwar, P., Chang, V. & Bandari, P. Oxygen Saturation in the Bone Marrow of Healthy Volunteers. *Blood* **99**, 394 (2002).
59. Krinner, a., Zscharnack, M., Bader, a., Drasdo, D. & Galle, J. Impact of oxygen environment on mesenchymal stem cell expansion and chondrogenic differentiation. *Cell Prolif.* **42**, 471–484 (2009).
60. Potier, E. *et al.* Hypoxia affects mesenchymal stromal cell osteogenic differentiation and angiogenic factor expression. *Bone* **40**, 1078–1087 (2007).
61. Malladi, P. *et al.* Effect of reduced oxygen tension on chondrogenesis and osteogenesis in adipose-derived mesenchymal cells Effect of reduced oxygen tension on chondrogenesis and osteogenesis in adipose-derived mesenchymal cells. *Am J Physiol Cell Physiol* **290**, 1139–1146 (2006).
62. Wang, Y. *et al.* The hypoxia-inducible factor alpha pathway couples angiogenesis to osteogenesis during skeletal development. *J. Clin. Invest.* **117**, 1616–26 (2007).

63. Salim, A., Nacamuli, R. P., Morgan, E. F., Giaccia, A. J. & Longaker, M. T. Transient changes in oxygen tension inhibit osteogenic differentiation and Runx2 expression in osteoblasts. *J. Biol. Chem.* **279**, 40007–40016 (2004).
64. Laurencin, C. T., Ambrosio, A. M. A., Borden, M. D. & Cooper, J. A. Tissue Engineering: Orthopedic Applications. *Annu. Rev. Biomed. Eng.* **1**, 19–46 (1999).
65. Whang, C. J., Mozingo, J. R. & Rhoton Jr., A. L. Comparison of flow in arterial and vein grafts to basilar artery. *Surg Forum* **25**, 449–451 (1974).